



High Temperature Water Gas Shift Catalysts: A Computer Modelling Study

Sreelekha Benny

Department of Chemistry
University College London

Johnson Matthey Technology Centre

Thesis submitted for the degree of Doctor in Engineering

March 2010

“It's our attitude at the beginning of a difficult undertaking which more than anything else will determine its successful outcome.”

William James (Father of American psychology)

Declaration

I, Sreelekha Benny confirm that the work presented in this thesis is the result of my own investigations and where information has been derived from other sources, this has been fully acknowledged.

Abstract

The high-temperature (HT) Water Gas Shift (WGS) reaction has considerable technological relevance for lowering CO content during the conversion of natural gas or liquid hydrocarbons to hydrogen. Conventional HT-WGS catalysts based on oxides of iron and chromium are well established industrially. However, it is crucial to remove any impurities present such as Cr⁶⁺, S or N during the catalytic process. In particular, Cr⁶⁺ is regarded as a Class I carcinogen and its presence is restricted by EU legislation. Even though Cr⁶⁺ is reduced during the catalytic process, caution must still be taken to eliminate any further impurities. Hence, it is desirable to identify alternative promoters and develop a Cr-free HT-WGS catalyst.

This thesis presents results obtained using atomistic simulation techniques to investigate the effect of Cr³⁺ and possible alternative dopants in three important iron oxide materials, Hematite (α -Fe₂O₃), Maghemite (γ -Fe₂O₃) and Magnetite (Fe₃O₄). The starting point is to develop an understanding of the structural properties and distribution of Cr³⁺ on the bulk and surface material of hematite. The critical stage of understanding the role of Cr³⁺ provides the basis from which criteria for novel dopants can be assessed. Al³⁺ and Mn³⁺ are proposed as the promising candidates on the basis of this study. The research has been extended to other complex iron oxides, such as maghemite and magnetite.

In summary, the role of chromium in the HT-WGS reaction has been investigated to establish criteria for effective, alternative promoter dopants. This investigation has provided a detailed insight into the atomic level behaviour of Cr³⁺, Mn³⁺, Al³⁺ impurities in three major iron oxide phases. The alternative dopants predicted in this study have been the subject of parallel experimental studies conducted by Johnson Matthey. The results of this study are already benefiting the design of more efficient iron-oxide catalysts for the HT-WGS reaction.

Acknowledgements

I would like to express my gratitude towards the following people who have provided me with invaluable help, support and advice throughout this work.

First and foremost, I wish to express my sincere gratitude to my supervisor Prof. Nora de Leeuw for introducing me to the world of computer modelling. Without her support, encouragement, guidance and good humour I would not be able to achieve this.

I would like to thank my industrial supervisor Dr. Sam French for the guidance offered to me at Johnson Matthey. I would like to specially acknowledge Prof. Richard Oldman for the immense support and valuable advice for the completion of this thesis. I would also like to thank Dr. Ricardo Grau-Crespo for the excellent advice and ideas along the way.

Many thanks go to a number of people from Johnson Matthey; Dr. Dave Thompsett, Dr. Ross Anderson, Dr. Martin Fowles, Prof. Sankar, Dr. Glenn Jones and Dr. Misbah Sarwar for the useful discussions, advice and support.

I would like to thank Dr. Zhimei Du and Dr. Iman Saadoune from UCL for their advice at the beginning of my research project. I would also like to mention my friends from UCL and Johnson Matthey who have made these years enjoyable.

I am grateful to EPSRC and Johnson Matthey for the financial support.

Finally I would like to thank my family, in particular my husband Benny Devadasan for all the support and encouragement he has given me throughout my EngD. I must mention my children and my mother for their understanding. I must also mention my grandmother, sister and family in India for their encouragement.

Thanks Everyone!

List of Publications

S. Benny, R. Grau-Crespo, N.H. de Leeuw (2008) “A theoretical investigation of α -Fe₂O₃ – Cr₂O₃ solid solutions.” *Physical Chemistry Chemical Physics*, 11, 808-815.

S. Benny, R. Grau-Crespo, S. French, N.H. de Leeuw (2010) “Comparison of (Fe_{1-x}Cr_x)₂O₃ and (Fe_{1-x}Al_x)₂O₃ solid solutions: A Computer simulation study.” (Submitted)

S. Benny, R. Grau-Crespo, A.Y.I Al-Baitai, R. Oldman, N.H. de Leeuw (2010) “Incorporation of isovalent impurities (Al³⁺, Cr³⁺, Mn³⁺) in Maghemite – A Computational study. ” (In preparation)

Contents

Declaration	3
Abstract	4
Acknowledgements	5
List of Publications	6
Contents	7
Chapter 1: Introduction	11
1.1 Introduction	11
1.2 The Water Gas Shift Reaction	14
1.2.1 Background	14
1.2.2 The WGS Process	14
1.2.3 The High Temperature Water Gas Shift Catalyst	15
1.2.4 Preparation of the Catalyst	17
1.2.5 Reaction Mechanisms: Regenerative and Associative	19
1.3 Structure and Properties of Iron Oxides	21
1.3.1 Hematite (α -Fe ₂ O ₃)	22
1.3.2 Maghemite (γ -Fe ₂ O ₃)	23
1.3.3 Magnetite (Fe ₃ O ₄)	25
1.3.4 Phase Transitions	29
1.4 Developments in HTS Catalysts	29
1.4.1 Promotion of Fe/Cr Catalysts	29
1.4.2 Chromium Free Catalysts	31
1.4.3 Summary of the Development of HT-WGS Catalysts	35
1.5 References	36

Chapter 2: Methodology	45
2.1 The Potential Model	46
2.1.1 The Coulombic Potential	46
2.1.2 Ewald Summation	46
2.1.3 Parry Method	47
2.1.4 The Short Range Potentials	48
2.1.5 The Electronic Polarisability	50
2.2 Energy Minimization	52
2.2.1 Optimisation Methods	52
2.2.2 Simulation Codes	54
2.3 Defect Energy Calculations	55
2.3.1 Point Defects	55
2.3.2 Simulating Site Occupancy Disorder in Ionic Solids	61
2.3.3 Vibrational Free energies : Monkhorst-Pack scheme	66
2.3.4 Spin Models of Cation Ordering	66
2.4 Surface	67
2.4.1 Types of surfaces	67
2.4.2 Modelling the Surfaces	69
2.4.3 Surface Defects	71
2.4.4 Hydroxylated Surfaces	72
2.4.5 Crystal Morphology	73
2.5 Summary	75
2.6 Reference	76
Chapter 3 : Hematite: Bulk, Surfaces and Defects	79
3.1 Introduction	79
3.2 Pure Hematite: Bulk and Surfaces	80
3.2.1 Bulk Calculations	80
3.2.2 Surface Calculations	82
3.3 Defects	94
3.3.1 Dissociated Water	94

3.3.2	The Role of Cation Dopants in Hematite: Al^{3+} , Sc^{3+} , Ti^{3+} , V^{3+} , Cr^{3+} , Mn^{3+} , Y^{3+} and La^{3+} .	100
3.3.3	The Effect of Cr^{3+} and Dissociated Water on the Surface Morphology of Hematite	121
3.4.	Conclusions	122
3.5.	References	124
Chapter4: The properties of the mixed solid solutions, $\text{Fe}_2\text{O}_3\text{-Cr}_2\text{O}_3$ and $\text{Fe}_2\text{O}_3\text{-Al}_2\text{O}_3$		128
4.1	Introduction	128
4.2	$\text{Fe}_2\text{O}_3\text{-Cr}_2\text{O}_3$ solutions	130
4.2.1	Magnetic Effects	136
4.2.2	Configurational Entropy	137
4.2.3	Vegards Law: Relation between the Cell Parameter and the Composition of the Defect	141
4.3	Comparison of $\text{Fe}_2\text{O}_3 - \text{Cr}_2\text{O}_3$ and $\text{Fe}_2\text{O}_3\text{-Al}_2\text{O}_3$ Solutions	143
4.3.1	Mixing Energies and Cation Ordering	144
4.3.2.	Deviation from Vegards Law	149
4.4	Summary	151
4.5	References	152
Chapter 5: More Complex Iron Oxides: Maghemite and Isovalent Impurities		154
5.1	General	154
5.2	Maghemite Model and Bond Distribution	155
5.2.1	Bonding in Maghemite	155
5.2.2	Defect Formation energy	157
5.3	Incorporation of Isovalent Ions in Maghemite	161
5.3.1	Solution Energy Calculations	161
5.3.2	Bond Distribution of the Dopants in Maghemite	165
5.4	Cation Ordering and Stability of the Dopant Systems	168
5.4.1	Configurational Effects	168

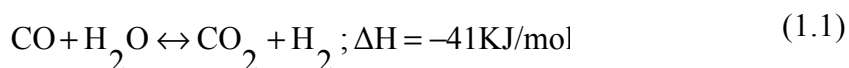
5.4.2	Effect of Dopants on the γ - to α - Phase Transition	171
5.5	Conclusions	174
5.6	References	175
Chapter 6:		
Magnetite: Defect Calculations in the Bulk and at the Surface		177
6.1	Introduction	177
6.2	Cation Charge Distribution	178
6.3	Calculations for Pure Magnetite	179
6.3.1	Bulk Calculations	179
6.3.2	(110) Surface of Magnetite	180
6.4	Doped Magnetite : Bulk Calculations	182
6.4.1	Lattice Energy Calculations	182
6.4.2	Effect of Dopants on Bulk Structures	184
6.4.3	Solution Energy of the Mixed Spinel Oxides	189
6.5	Dopants at the Surface	192
6.5.1	Cr^{3+}	192
6.5.2	Al^{3+}	194
6.5.3	Mn^{3+} and Mn^{2+}	195
6.6	Oxygen Vacancy Formation in Magnetite	197
6.6.1	Oxygen Vacancies in the Bulk	197
6.6.2	Oxygen Vacancies at the Surface	199
6.6.3	Effect of Dopants in the Oxygen Vacancy Formation Energy	201
6.7	Conclusions	203
6.8	References	204
Chapter 7: Implications for Catalysis and Conclusions		206
7.1	References	210
Appendix I		211

Chapter 1

INTRODUCTION

1.1 Introduction

The high temperature water gas shift (HT-WGS) reaction:



is a reversible exothermic chemical reaction¹, which has considerable technological relevance for lowering carbon monoxide content during the conversion of natural gas or liquid hydrocarbons to hydrogen. This reaction plays an important role in the production of hydrogen, which has various key applications in the field of catalytic synthesis for example, hydrogenation, methanol synthesis, and Fischer Tropsch Synthesis. According to published data, 10% of yearly energy consumption will originate from the WGS reaction by the year 2030^{2,3}.

Chromium-doped iron oxide catalysts are well established for commercial use in the high temperature stage of the WGS reaction. However, due to the carcinogenic nature of chromium,^{4, 5} they are the subject of increasingly restrictive EU legislation (IPPC Directive 96/61/EC and 200/76/EC)⁶ and alternative dopants need to be identified. Furthermore, improved catalysts are required to meet the needs for reduction in reactor size, tighter cost targets, higher performance and to overcome the operational drawbacks of the current commercial catalysts.

The work reported in this thesis concerns an investigation of the properties of the three technologically important iron oxides, hematite (α -Fe₂O₃), maghemite (γ -Fe₂O₃) and magnetite (Fe₃O₄) used in industrial catalytic applications, such as the Water Gas Shift (WGS)⁷ reaction and Fischer Troph Synthesis (FTS)⁸. The project has focused specifically on the conventional high-temperature-shift catalysts based on oxides of iron and chromium, in particular the role of dopants such as chromium to the catalytic process.

This first chapter begins with the background information on the WGS reaction and a review of the literature on the structure and properties of the iron oxide materials; hematite, maghemite, magnetite and the recent developments in this field. The different computer modelling methods applied in this work are summarized in Chapter 2.

The toxic effects of chromium make it important to seek an efficient and improved catalyst for the high temperature phase of the WGS reaction. The studies reported in Chapter 3 have been carried out to achieve an understanding of the behaviour of Cr³⁺ in the bulk and surface material of the hematite system together with a number of isovalent metal dopant alternatives, for example, Al³⁺ and Mn³⁺.

Chapter 4 demonstrates a more detailed comparative study of the mixed solid solutions of the $\text{Fe}_2\text{O}_3 - \text{Cr}_2\text{O}_3$ and $\text{Fe}_2\text{O}_3\text{-Al}_2\text{O}_3$ systems. The thermodynamic properties of the solution systems are investigated along with the degree of cation ordering and the influence of magnetic and vibrational effects on the stability of these solid solutions are discussed.

The study is continued by considering more complex iron oxide systems. The first material considered was maghemite, which is an intermediate in the reduction process, as a preliminary work to studying magnetite, the active phase of the WGS reaction. Chapter 5 presents a detailed study of the behaviour of the metal dopants in the bulk material of maghemite. The phase stability and the cation ordering of the system are discussed.

In Chapter 6, the influence of the chosen metal dopants in the bulk material of magnetite is investigated. In addition, a non-dipolar (111) surface is constructed and the position of the dopants and stability of the system are explored.

The results of the modelling techniques are compared with literature data and at experiments carried out Johnson Matthey Technology Centre. The main focus will be to understand the role of chromium in the WGS reaction and compare it with the potential behaviour of aluminium and manganese. A number of catalytic parameters are investigated such as, oxygen vacancy formation and the oxidation-reduction energetics. The predictions obtained from the computational modelling tools will be interpreted in the context of experimental results and are summarised in Chapter 7.

1.2 The Water Gas Shift Reaction

1.2.1 Background

In addition to its importance in a variety of catalytic synthesis processes nowadays, industrial hydrogen is considered to be the most important candidate as a clean energy carrier. For example, high-purity hydrogen is required for the operation of low temperature polymer electrolyte membrane fuel cells (PEMFCs)⁹. Therefore the production and purification of hydrogen has a dominant position in industrial technology and is also an essential component of many industrial processes. As it can be produced from renewable energy sources (biodegradable organic waste), it represents one possibility to reduce the negative impact of civilization on the environment such as the greenhouse effect and air pollution¹⁰. Industrially hydrogen is produced in large quantities from hydrocarbon fuels (e.g. methane or alcohols) by reforming processes. The product stream of the reforming process typically contains mixtures of hydrogen, carbon monoxide, carbon dioxide and steam¹¹. The industrial elimination of CO in the reforming product stream, which is essential for several downstream processes, for example, ammonia synthesis, includes several bulky and complex processing units. Effectively then, the WGS reaction also enhances the hydrogen yield since water is reduced to hydrogen in the process of oxidising carbon monoxide to carbon dioxide.

1.2.2 The WGS Process

The WGS process was first reported and patented by Mond and Langer¹² in 1888. The process is usually carried out in two stages due to thermodynamic equilibrium limitations. The first step involves a high temperature step operating at 310–450°C,^{13, 14} which reduces CO content to 2–3%. The iron oxide/chromium catalysts developed by German researchers at BASF¹⁵ in 1911 as part of the ammonia synthesis development programme still forms the basis for the high temperature shift (HTS) catalyst used today, which has hardly changed since its initial development¹⁶. The second stage uses a low temperature water gas shift catalyst based on Cu/ZnO/Al₂O₃ that operates at 210–240°C¹. The equilibrium constant for the reaction decreases with increase in temperature (**Figure 1.1**). With the aid of inter-stage cooling, ca 1% CO exit levels were achieved by using the two separate catalyst beds of iron-chromium oxide catalysts and copper-zinc oxide catalysts^{1, 16}, and is still used commonly. (Note: This thesis specifically focuses on the HTS because of the toxic issues of the conventional catalyst.)

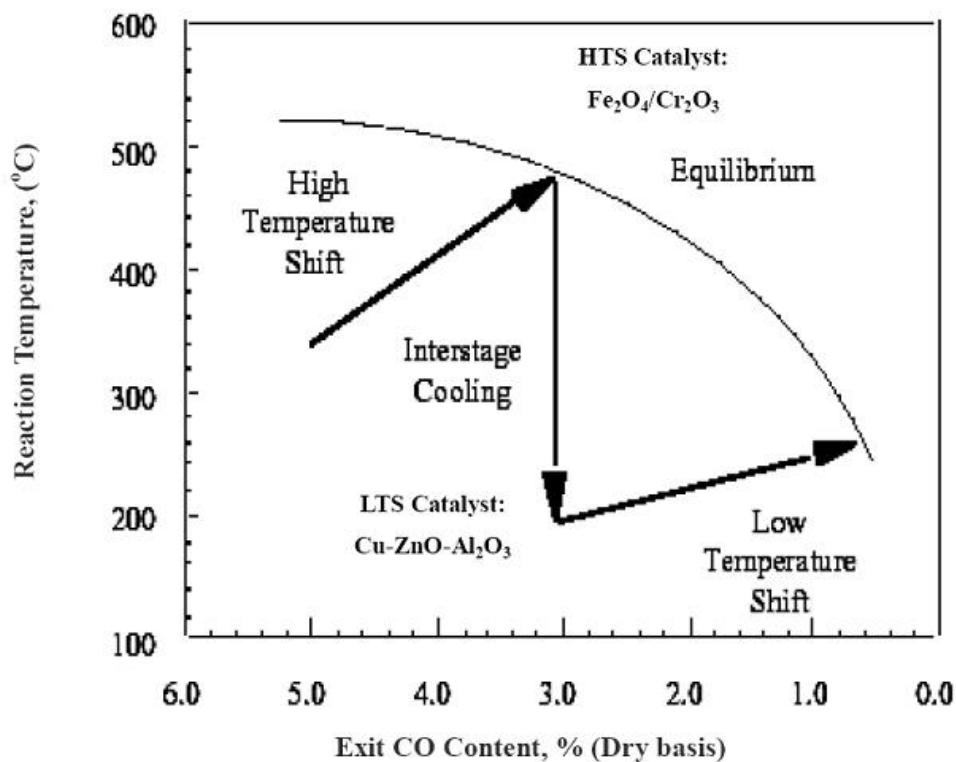


Figure 1.1 : Schematic representation of the water gas shift reaction (Twiggs M.V., et al, 1989¹)

1.2.3 The High Temperature Water Gas Shift Catalyst

The HT-WGS reaction is carried out by using an iron oxide catalyst structurally promoted by chromium oxide^{4, 13}. It is reported that Cr₂O₃ retards the thermal sintering of magnetite. It also prevents the loss of surface area of the catalyst at high temperatures^{16, 17}. The catalyst is activated by a partial reduction pre-treatment where it transforms to a spinel phase. It is generally accepted that the presence of chromium increases the lifetime of the catalyst which prevents the rapid thermal sintering of magnetite crystallites by acting as a stabilizer and the consequent loss of surface area that occurs in pure iron catalysts.¹⁶

The composition of iron oxide and chromium oxide varies according to manufacturers. Markina *et al*¹⁸ and others argued that 14 wt% Cr₂O₃ produces greatest resistance to sintering. However, a commercial catalyst is usually composed of 92 wt% iron oxide and 8 wt% chromium oxide¹⁹. These stabilised catalysts can be operated in plants for 2-10 years and are not particularly sensitive to sulphur poisoning¹⁶. However, relatively slow sintering still causes a decrease in activity of the catalyst, which requires catalyst replacement.^{14, 20, 21}

Domka and co-workers¹⁹ found that the surface area (40m²g⁻¹) of chromium containing catalysts remained higher than non chromium containing catalyst. Catalyst activity has been studied in detail by a number of researchers²²⁻²⁵ and found to decrease with age. Chandra *et al*²³ argued that this decrease in activity is rapid during the initial period (up to 400h), slows down between 400-700h and after 1000h the activity became constant. This argument is in agreement with Hoogschagen *et al*²⁴ and Mars²⁵.

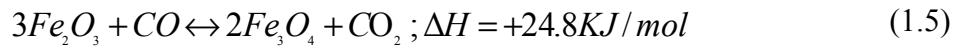
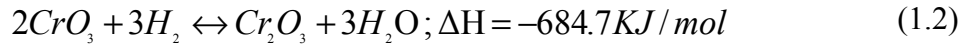
Even though the HT-WGS catalytic process based on iron-chromium oxides is well established industrially, during the manufacturing process, some of the Cr³⁺ is converted to Cr⁶⁺. This hexavalent chromium is highly toxic and harmful to both human beings and the environment. In addition, it is highly water soluble and can cause unnecessary reactions such as leaching of unreduced Cr³⁺ which in turn leads to considerable evolution of heat and causes large increase in the bed temperature

during the start up^{3, 16}. Due to its harmful effects Cr^{6+} is regarded as a Class I carcinogen and its presence is restricted according to EU legislation. Even though it is reduced during start up, caution must still be applied to eliminate any impurities present. Alternative promoters are desirable to develop a Cr-free HTS catalyst.

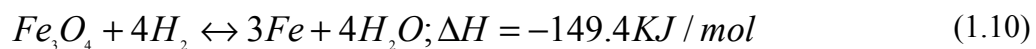
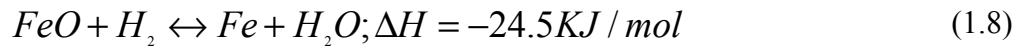
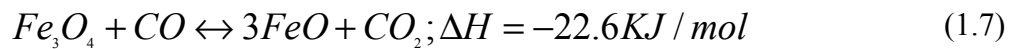
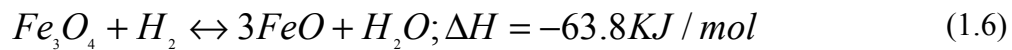
1.2.4 Preparation of the Catalyst

The preparation method has a strong influence on the properties of the catalyst material.²⁶⁻²⁸ Doppler *et al*²⁹ suggested that even with identical chemical composition, the samples made by different routes show different activities and stabilities due to their difference in particle size and the distribution of chromium through the mixed oxides. Fe-Cr oxide catalysts can be synthesised by precipitation or co-precipitation of the mixed iron and chromium nitrates with ammonium hydroxides. Alternatively in an impregnation method, iron hydroxide gel is first prepared and then impregnated with chromium nitrate solution. Although a surface enrichment of chromium ions was observed in samples prepared by both routes, the surface concentration of chromium is higher in the impregnated samples. During activation, which involves the reduction to magnetite, the relative concentration of chromium ions at the surface decreases significantly, this suggests migration of chromium ions from the surface into the bulk. Recently Pereira *et al*²⁶ conducted a comparison study between the precipitation and impregnation methods and found that the most active catalyst is obtained by adding chromium using the impregnation method due to the yield of a catalyst with high specific surface area.

The materials calcined at 773K or above consist of hematite. The calcinations must be carefully controlled to avoid the formation of chromic oxide (CrO_3)¹. The CrO_3 phase present must be reduced to Cr_2O_3 during start up (Eqns.1.2, 1.3). The catalytically active phase of iron oxide is magnetite. Catalyst pre-treatment involves the reduction of hematite to magnetite (Eqns. 1.4, 1.5) and any CrO_3 to Cr_2O_3 using hydrogen or process gas mixtures of hydrogen, nitrogen, carbon monoxide and water vapour^{1, 17}.



During the reduction process caution must be applied to avoid over-reduction of the active catalyst material to lower oxides, carbides and metallic Fe (Eqns. 1.6 - 1.10), which leads to undesirable processes such as methanation and Fischer Tropsch Synthesis (FTS)^{1, 8, 16}. Moreover, relatively a small degree of over-reduction can result in weakening and physical damage to the catalyst pellets¹⁷.



Furthermore, over reduction causes the consumption of hydrogen and causes damage to the industrial reactors due to the exothermic nature of these reactions and the pressure drop caused by the degradation of catalyst pellets. Lywood and Twigg¹⁷ developed an empirical formula to ensure a reliable reduction process for the catalyst.

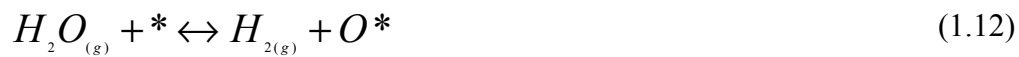
$$R = \{[CO] + [H_2]\} / \{[CO_2] + [H_2O]\} \quad (1.11)$$

where R is the reaction factor, which helps to predict the degree of reduction for a given gas composition in the presence of steam. According to this, the plants operating with a value of $1.2 < R > 1.6$ will sustain over-reduction. The authors¹⁷, suggested that steam must always be present during the reduction process, 10% steam in hydrogen at 400°C or 17% steam at 550°C is sufficient to prevent over-reduction.

1.2.5 Reaction Mechanisms: Regenerative and Associative

Extensive studies over the last two decades have suggested that the WGS reaction may involve two types of reaction mechanism^{4, 16} with contrasting pathways. The regenerative and associative, which were first proposed by Armstrong and Hilditch³⁰ in 1920. The regenerative or redox mechanism is based on the dissociation of water on the catalyst to produce hydrogen and subsequent oxidation of the catalyst surface (Eqn.1.12). The surface is then reduced by carbon monoxide (Eqn.1.13) to produce carbon dioxide and thereby complete the catalytic cycle^{31, 32}.

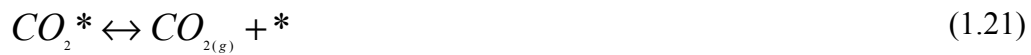
The overall reaction can be described as³²



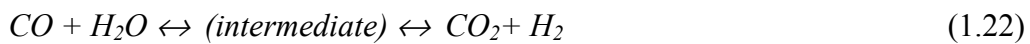
where * stands for a vacancy surface site formed by the removal of an oxygen atom and O* is the reducible oxygen on the oxide surface.

The elementary steps of the mechanism can be described as follows³³





The associative mechanism is based upon the interaction of adsorbed carbon monoxide and water on the catalyst surface to form an intermediate, which breaks down to form reaction products⁴.



The regenerative mechanism is believed to be the dominant pathway for the HT-WGS reaction over Fe-Cr catalysts. The importance of the redox mechanism in these high temperature catalysts has been confirmed by Boreskov³⁴ who showed that a Fe²⁺/Fe³⁺ coupling existed in Cr₂O₃-Fe₃O₄ catalysts, with Fe²⁺ being oxidised to Fe³⁺ by water and Fe³⁺ being reduced by carbon monoxide.

At low temperatures (LTS), considerable uncertainty still exists as to the exact reaction mechanism. A number of theoretical³⁵⁻⁴⁰ and experimental (redox^{9, 33} and associative^{41, 42}) studies have supported both mechanisms. Schumacher *et al*⁴⁰ conducted a density functional theory (DFT) modelling study of low temperature WGS catalysts by using a microkinetic model based on a redox mechanism and predicted that the activity of the copper based catalysts can be improved by increasing the strength with which carbon monoxide and oxygen bond to the

surface⁴⁰. Following this work, recently Gokhale *et al*³⁹ proposed a new alternative mechanism involving a highly reactive surface intermediate, carboxyl (COOH), in a DFT study employing a microkinetic model.³⁸

1.3 Structure and Properties of Iron Oxides

Iron oxides are materials with low cost and toxicity and are widespread in nature. For example, iron oxides are responsible for the red color of the planet Mars⁴³. These oxides represent an important class of materials which are used in a wide range of applications including catalysis^{1, 7, 43} in magnetic devices^{44, 45} and in lithium batteries^{46, 47}. Iron oxides are used as low temperature, high temperature and semiconductor heterogeneous catalysts and also serve as model systems for the investigation of dissolution mechanisms, adsorption of ions, molecules and oxidation/reduction reactions⁴⁸.

The structure and properties of the three different iron oxides; hematite, maghemite and magnetite, used in this study are now detailed.

1.3.1 Hematite (α -Fe₂O₃)

Hematite is one of the most abundant iron oxides⁴⁸ in the natural environment and is stable under atmospheric conditions. The crystal structure of hematite was determined by Pauling and Hendricks⁴⁹ in 1925. Hematite has the corundum type structure with a space group having the rhombohedral symmetry, $R\bar{3}c$ (no.167). This material exhibits ferromagnetism in addition to antiferromagnetism below the Neel temperature of 950 K⁵⁰. Hematite is an anti-ferromagnetic insulator below the Morin temperature (250 K)⁵¹. Although iron cations are most stable in their trivalent oxidation state, this oxide exhibits nonstoichiometry associated with oxygen vacancy formation^{52, 53}. Hematite is considered to be an intrinsic semiconductor at high temperature⁵⁴ and the material is suitable for oxidation/reduction reactions and can also be used as acid/base catalysts. Furthermore Chang *et al*⁵⁴ suggested that intrinsic electronic defects are more important than lattice defect concentrations and

the cations migrate interstitially, which was verified by Hoshino and Peterson *et al*⁵⁵. Oxidation-reduction processes at hematite surfaces in aqueous solutions involve small amounts of ferrous ions (Fe^{2+}) dissolved in ferric ions (Fe^{3+}) and the reactivity of the material depends on the structural arrangement of these ions.^{56, 57}

In hematite, the cations are six- coordinated and occupy two thirds of the octahedral sites of the slightly distorted hexagonal close- packed oxygen array in a repeating pattern of Fe-O3-Fe along the c axis. The iron atoms are staggered along the c-axis from the ideal octahedral lattice site positions (**Figure 1. 2**). This results in a slight distortion, which causes two types of Fe-O bonding, three short (1.944 Å) and three long (2.096 Å) Fe-O bonds. Isomorphic substitution is possible between the Fe^{3+} in the octahedral position and other trivalent metal cations of similar size⁴⁸.

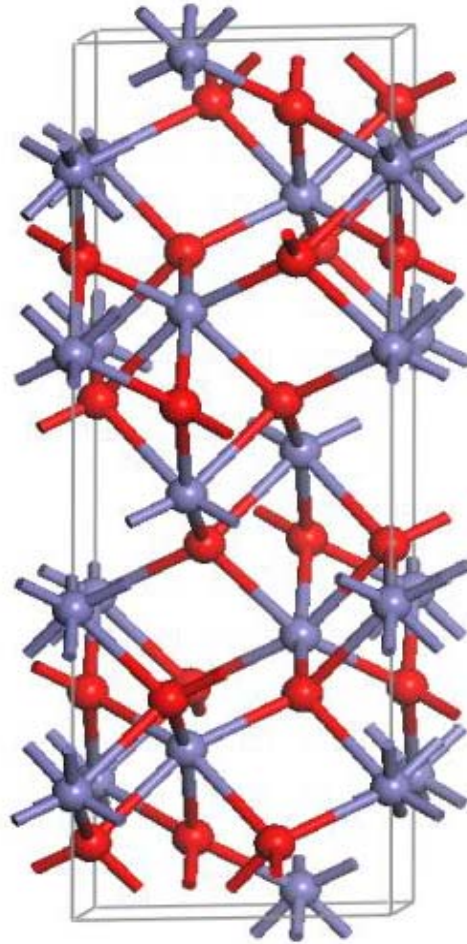


Figure 1. 2: The hexagonal unit cell of hematite (Fe_2O_3). Cations (Fe^{3+}) are represented by blue and O anions by red spheres.

Numerous studies^{51, 58-62} have focused on the electronic, structural and magnetic properties of hematite. Experimentally, the frequencies of the infrared normal modes and the optical constants have been determined from reflection and thermal emission spectra using dispersion theory^{63, 64}. Several works^{65, 66} have also focused on the effect of particle size, shape, and orientation on hematite infrared spectra. The band gap width of hematite was predicted by Mochizuki *et al*⁶⁷ in 1977 as 2eV. This wide band gap is the result of strong on-site Coulomb repulsion occurring between the Fe 3d electrons. Chamritski *et al*⁶⁸ calculated the phonon frequencies for the first time using atomistic simulation methods. Recently Blanchard *et al*⁵⁸ presented the first theoretical infrared spectrum of an iron oxide computed using first-principles methods. This work using atomistic simulations, predicted that the vibrational and

magnetic properties depend on the defect chemistry, which is explained in later chapters of this thesis.

1.3.2 Maghemite ($\gamma\text{-Fe}_2\text{O}_3$)

Maghemite was named in 1927⁶⁹. The name implies an intermediate character between *MAG*netite and *HEM*atite⁶⁹. Maghemite is used as metal oxide thin film preparation⁷⁰. It has the same structure as magnetite and is also ferrimagnetic. Maghemite is one of the technologically important iron oxides used in storage media in magnetic recording applications⁷¹. Due to its magneto-optical properties the material can be used as a sensor for the Earth's magnetic field⁷². Apart from its magnetic properties, maghemite also has applications in the field of catalysis⁷³⁻⁷⁵ and in a variety of bioseparations⁷⁶. The presence of cation vacancies in the structure makes maghemite a fascinating material. Maghemite can be considered as an iron deficient magnetite spinel, which has both octahedral and tetrahedral iron sites. Maghemite is usually obtained by the oxidation of magnetite, Fe_3O_4 or dehydration of lepidocrocite, $(\gamma\text{-FeO}(\text{OH}))$ ⁴⁸.

The basic structure of maghemite is closely related to the inverse spinel Fe_3O_4 , but differs from the latter by the presence of vacancies distributed on the cation lattice. The unit cell of Fe_3O_4 contains eight formula units, $[(\text{Fe}^{3+})_8]_{\text{A}}[(\text{Fe}^{3+}\text{Fe}^{2+})_{16}]_{\text{B}}\text{O}_{32}$ where A and B designate tetrahedral and octahedral coordination sites respectively (**Figure 1.3**). Oxidation of Fe_3O_4 to $\gamma\text{-Fe}_2\text{O}_3$ is accompanied by the creation of cation lattice vacancies and results in a cell which contains $\text{Fe}_{21\frac{1}{3}}^{3+}\Delta_2\text{O}_{32}$ where Δ represents a cation vacancy⁷⁷.

An ordered vacancy arrangement with tetragonal symmetry in maghemite has been verified by Greaves *et al*⁷⁸ with a lattice parameter of $a = 8.348 \text{ \AA}$. X-ray powder diffraction,^{77, 79} neutron diffraction⁸⁰, Mossbauer spectroscopy and magnetization studies^{81, 82} have revealed that there is a strong preference for vacancies to occur at

octahedral positions. Hence the molecular formula can be written as,

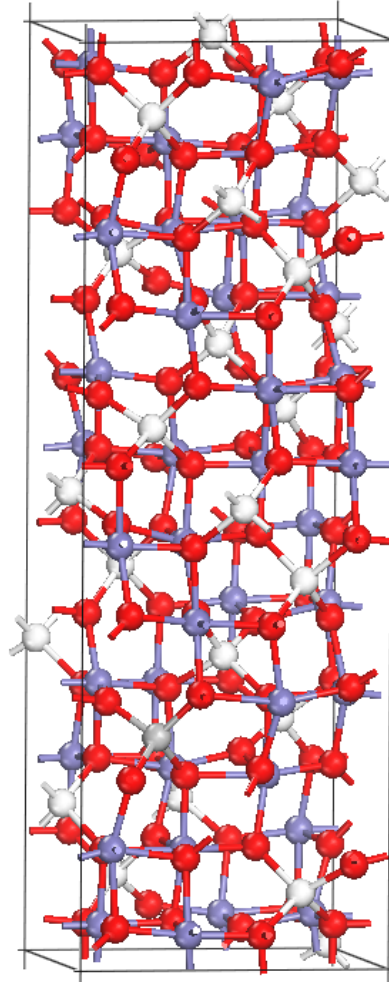
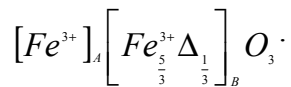


Figure 1.3: Ordered 1x 1x 3 supercell of Maghemite (blue spheres represent octahedral Fe^{3+} , white spheres tetrahedral Fe^{3+} and red spheres oxygen.)

According to Shmakov *et al*⁸⁰, the basic structure of γ - Fe_2O_3 corresponds to the space group $P4_332$, but the ordered structure would result in the formation of a threefold unit cell with $a'=b'=a$ and $c' \sim 3a$, where a', b', c' and a are the tetragonal and cubic lattice constants respectively, leading to a decrease of symmetry to space group $P4_12_12$ (no.92). The authors also suggested that cation vacancy ordering does not cause any distortion of the basic cubic spinel unit cell with space group $P4_332$. However, the results of Somogyvari *et al*⁸³ showed a slight distortion of the basic cubic cell lattice, which best describes the overall fit by the tetragonal $P4_12_12$ space

group⁸⁴. A recent NMR study⁸⁵ has proposed a more complex distribution of vacancy arrangement in both tetragonal and cubic structures. In magnetite, the anti-parallel coupling of the magnetic moments on the tetrahedral and octahedral sites causes the ferrimagnetic behaviour. All the Fe^{3+} ions in maghemite are ferrimagnetic like magnetite with the spins on the tetrahedral sites oppositely directed to those on the octahedral sites.

1.3.3 Magnetite (Fe_3O_4)

Magnetite, nicknamed lodestone is the longest known magnetic material and has been used by navigators to locate the magnetic North Pole^{86, 87}. It was discovered 2500 years ago by Thales of Miletus (625–547 BC)⁸⁸. It is a metallic ferrimagnet found on Earth as well as other planets^{43, 89}. At room temperature, magnetite crystallizes in the face centered – cubic (fcc) inverse spinel structure with iron ions occupying the tetrahedral A sites and octahedral B sites. The space group is $Fd\bar{3}m$, (no.227)^{90, 91}. The oxygen atom forms a close packed face centred cubic structure with iron ions occupying the interstitial positions (**Figure 1.4**).

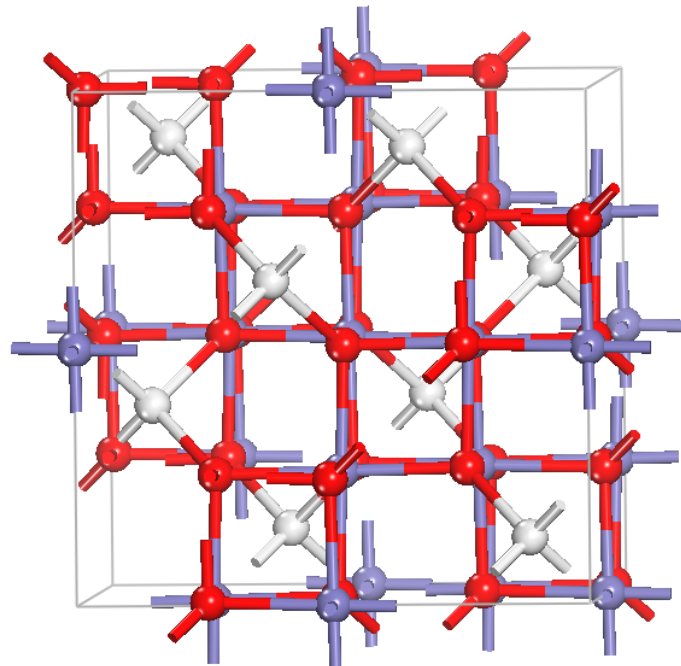


Figure 1.4: Cubic inverse spinel structure of magnetite (blue spheres - octahedral $\text{Fe}^{2.5+}$, white – tetrahedral Fe^{3+} and red - oxygen)

Magnetite undergoes a phase transition, first detected by Parks and Kelley⁹² (1926) by means of heat capacity measurements at a temperature, the Verwey⁹³ temperature, above 120K. At this phase transition, a decrease of two orders of magnitude in the electrical conductivity occurs in such a way that at low temperatures magnetite is an insulator and above the Verwey transition temperature it is a metallic conductor⁹³. Verwey characterized the discontinuity in the electrical conductivity as an order–disorder transition and proposed an ionic model in which above the Verwey temperature, Fe³⁺ and Fe²⁺ are dynamically disordered in the lattice. The structure becomes completely charge disordered with an ionic structure of Fe³⁺_A[Fe²⁺_BFe³⁺]_BO₄²⁻ similar to maghemite (**Figure 1.4**). This inverse spinel structure accounts for the high electric conductivity of magnetite, which is attributed to the electron hopping mechanism through the continuous exchange of electrons between the Fe²⁺ and Fe³⁺ ions in the octahedral sites.⁹⁴

Imada *et al*⁸⁹ demonstrated that the Verwey transition plays an important role in lattice, charge and orbital ordering. Magnetite is a well-known ferrimagnet and below the Neel temperature (851K) magnetite becomes ferromagnetic with the magnetic moments of the Fe ions antiparallel between A and B sites.⁹⁵ According to Neels⁹⁵ model, it is assumed that the magnetic interaction between the octahedral (B) and tetrahedral (A) iron ions is strongly negative and between the ions of the same lattice is weak and positive. These interactions favor an antiparallel arrangement of the sublattices A and B. The magnetic ordering in oxide spinels is mainly due to superexchange interactions via the oxygen ions. The superexchange interaction is a function of interatomic distances and depends on both the lattice parameter and oxygen position parameter.⁹⁶

The spinel structure of magnetite was first proposed by W.H. Bragg⁹⁰ in 1915. Below 120K, Verwey⁹³ proposed a charge ordered orthorhombic structure and this structure was refined by Hamilton⁹⁷ using neutron diffraction data and later reviewed by Fleet⁹⁸ using X-ray diffraction data. Iizumi *et al*⁹⁹ proposed a charge ordered monoclinic structure of magnetite below the Verwey temperature and this monoclinic symmetry was confirmed by Yoshido *et al*¹⁰⁰. Iizumi and co workers¹⁰¹ conducted a neutron diffraction study on the low temperature structure and imposed

an orthorhombic symmetry and claimed an ordered structure. However, the question of symmetry of the lower temperature phase still remains controversial. Later studies indicate that the charge ordered structure exhibits monoclinic symmetry, which is verified by neutron diffraction¹⁰¹ x-ray diffraction,¹⁰² electron scattering¹⁰³ and nuclear magnetic resonance^{104, 105} studies. Above 120K, a charge ordered model of 2.4+ and 2.6+ at the octahedral sites is proposed by Wright *et al*¹⁰⁶ by using high resolution x-ray and neutron diffraction data. Later studies from the same authors proposed⁸⁷ a charge ordered model of 2.5+ in the octahedral B sites and 3+ in tetrahedral A sites. Considering the electron hopping mechanism exhibited by these inverse spinels, the charge is averaged to 2.5+. Recently Piekarz *et al*¹⁰⁷ presented a group theory analysis of the Verwey transition and described the crystal transformation from high-temperature cubic phase to low temperature monoclinic phase by applying *ab-initio* density functional methods. The authors clarified the relation between charge order and the origin of the Verwey transition and found that the metal-insulator transition is promoted by electron interactions. Later on Palin *et al*¹⁰⁸ investigated the cation ordering of 2-3 spinels using Monte Carlo simulation and atomistic techniques. They found that at low temperatures, the octahedral cations in the inverse spinel become ordered. Most recently Yamauchi *et al*¹⁰⁹ conducted a first principles study and revealed that the insulating phase at low temperature is driven by the charge ordering. The metal-insulator transition and charge ordering of magnetite is still a matter of debate. Research is ongoing to explore more information regarding the charge ordering, magnetism, electronic structure and origin of the Verwey transition of magnetite.

1.3.4 Phase Transitions

Phase transitions are crucial for high temperature processes especially if more than one type of catalyst phase is involved. The conversion of the different phases arises mainly due to similarity in the structures of magnetite and maghemite and the latter is converted to hematite at high temperatures. In the WGS process three different iron oxide phases are reported^{5, 75}. The starting material is hematite which is then reduced to the active phase, magnetite. Some manufacturers reported the presence of maghemite in this reaction⁵. Hematite possesses only octahedral iron sites while both magnetite and maghemite possess tetrahedral and octahedral iron sites. With trivalent

iron there are five d electrons in the 3d orbitals. In the high spin state, each of these would be unpaired and occupy all of the t_{2g} and e_g orbitals in an octahedrally coordinated environment or all of the t₂ and e sites in a tetrahedrally coordinated environment. Since there are no degeneracies, the crystal field stabilization energies for each of these coordinations are zero. Thus there is no preference for either coordination. However the coordination will be driven by lattice energy and kinetic issues.

The conversion of hematite to magnetite occurs with the formation of maghemite as an intermediate. Maghemite is the meta-stable phase converted to hematite at about 350°C, and on further reduction magnetite is produced. In order to convert from maghemite to magnetite, either iron must be added or oxygen must be lost in addition to the valence change of the iron occupying the tetrahedral sites. The reverse is quite unlikely. The conversion from hematite to magnetite would also involve a complete rearrangement of the lattice to create the tetrahedral sites as well as to overcome any activation energy associated with this rearrangement. On the other hand, once a spinel is formed, conversion between magnetite and maghemite would not involve any lattice rearrangement and should proceed readily.

1.4 Developments in HTS Catalysts

Extensive research has been conducted on the WGS reaction using various experimental and theoretical techniques including IR¹¹⁰, X-ray photoelectron spectroscopy (XPS)¹¹¹, X-ray diffraction (XRD),¹¹² X-ray absorption fine structure (XAFS)¹¹³, Mossbauer spectroscopy¹¹⁴, electron microscopy (HREM), radioactive labelling, temperature programmed techniques (TPR&TPD), density functional theory (DFT) and molecular dynamics (MD).

1.4.1 Promotion of Fe/Cr Catalysts

Activity and thermal stability are two of the challenges faced by researchers in the development of WGS catalysts. The addition of promoters to the catalyst can significantly improve its activity.

Topsøe and Boudart¹⁴ in 1973 using Mossbauer spectroscopy analysis found that the addition of Pb^{4+} to the $\text{Fe}_3\text{O}_4/\text{Cr}_2\text{O}_3$ catalyst results in an increased activity at about 400°C . However the catalyst failed in terms of stability at high temperatures. The authors argued that the presence of Pb^{4+} increased the covalence in the system and subsequently improved electron hopping, which enhances the high conductance of the magnetite material¹⁶

Idakiev *et al*¹² using X-ray analysis found that $\text{Fe}_3\text{O}_4/\text{Cr}_2\text{O}_3$ doped with 15wt% CuO showed higher activity than 5wt% CuO which is attributed to the presence of metallic copper crystallites. However, the catalytic activity slowly decreases due to the sintering of Cu particles. Rhodes and co-workers¹¹ conducted research on Fe-Cr catalysts promoted with 2wt% B, Pb, Cu, Ba, Ag and Hg. All dopants were found to increase the activity across the temperature range (623-713K) except B. The results showed that the addition of Ba^{2+} , Ag^{2+} and Hg^+ increase the activity above the promotion levels observed with Cu^{2+} . The authors suggested that these promoters are incorporated into solid solution. Rhodes *et al*¹⁶ clarified the role of copper in modifying the electronic properties of the $\text{Fe}_3\text{O}_4/\text{Cr}_2\text{O}_3$ catalyst. Again Kappen *et al*¹³ in 2001 using an XAFS study observed that Cu^{2+} was incorporated into the iron and chromium phases and segregated out forming metallic clusters on the oxide surfaces during the reaction. Later Edwards *et al*¹¹ in 2002 using HREM examination showed that there was no evidence of supported Cu in metallic or nano particle forms. Further STEM-EDX measurements suggested that Cu was immersed into the solid solution, in a surface segregated state and this agrees with Rhodes *et al*.¹¹ These observations suggested that Cu electronically promotes the catalyst by producing active sites.

A gadolinium promoted iron-oxide based catalyst was tested by Tsagaroyannis *et al*¹¹⁵. This Gd promoted catalyst showed remarkable catalytic activity and stability. The catalyst appeared to show higher activity than magnetite, but was less active than the commercial catalyst.

Hu *et al*¹¹⁰ conducted a comparative study of CeO₂-Fe₂O₃-Cr₂O₃, Fe₂O₃-Cr₂O₃ and Fe₂O₃ catalysts using temperature-programmed desorption (TPD) and pulse reactions. The study revealed that ceria doped catalysts have the largest specific surface area and lowest reduction temperature. The reaction mechanism is confirmed as a redox process. The FT-IR spectroscopy results also suggested that the ceria promoted catalyst is structurally sensitive, highly active, selective and stable under reaction conditions.

Lei *et al*¹¹⁶ investigated the activity of HT-WGS oxide catalysts promoted by precious metals (Pt, Rh, Ni and Pd) on a ceria support, which promotes oxygen storage. The results showed that the performance of iron oxide–chromia catalysts can be significantly improved by promotion with small amounts of rhodium. Platinum is also found to increase the reactivity with ceria or ZrO₂ supports.

According to the studies carried out by Ivan *et al*¹¹⁷ vanadium doped catalysts exhibit higher catalytic performance than the commercial catalyst, however, the specific surface area of the vanadium catalyst is much lower than the chromium catalyst.

Recently Rarog-Pilecka *et al*¹¹⁸ replaced ruthenium with chromium and claimed that the Ru modified catalyst exhibited higher activity than the commercial catalysts. However, the authors failed to predict the stability of the catalyst.

1.4.2 Chromium Free Catalysts

The highly water-soluble hexavalent state of chromium causes health hazards to both human beings and the environment. In relation to the toxic nature of chromium, the first development of Cr - free catalysts were patented from 1982¹¹⁹ onwards. HTS catalysts containing calcium, cerium or zirconium were first reported by Chinchin¹¹⁹. However, the activities of these catalysts are far below that of the commercial Fe₂O₃-Cr₂O₃ catalysts.

Lund and Dumesic¹²⁰ investigated the activity of silica supported magnetite and outlined how the activity of the catalyst decreases with the decrease in particle size of the supported catalyst. The authors showed that the unsupported magnetite did not show any dependence on particle size and the highly polarising Si⁴⁺ around magnetite might create an electron deficiency at the surface octahedral iron cations and thereby disrupt the redox couple. The authors also investigated the effect on activity of the addition of divalent cations such as Mg²⁺, Mn²⁺, Co²⁺, Ni²⁺ and Zn²⁺. These ions have a similar charge to Fe²⁺ ions and consequently would not influence the covalency of Fe³⁺ ions and any electron exchange reaction. These results are in agreement with the studies led by Yur'eva *et al*¹²¹.

Rethwisch and Dumesic¹²² in 1986 developed iron oxide catalysts containing MgO, ZnO, SnO₂, Al₂O₃, TiO₂ and SiO₂ and found that ZnO, MgO and SnO are more active than TiO₂ and Al₂O₃. SiO₂ is the least active, which is the most acidic oxide in this group.

Gottaschalk *et al*¹²³ in 1988 found that Co-Mn and Cu-Mn catalysts were more active than commercial Fe₂O₃-Cr₂O₃ catalysts. However, Co-Mn catalysts produce methane during the reaction while Cu-Mn catalysts were very sensitive to sulphur. Later alkali promoted Cu, Co and Fe-Mn were reported by Hutchings *et al*¹²⁴. The authors calculated the rate constants of Fe-Mn, Cu-Mn and Co-Mn catalysts and found that Co-Mn exhibited significant methanation activity and Cu-Mn was more sensitive to sulphur than Fe-Cr catalysts. Another catalyst formulation for the WGS reaction was proposed by Hakkarainen *et al*¹²⁵ in 1994. The Co-Mo oxide catalysts

showed high tolerance to sulphur. These catalysts promoted by potassium and/or magnesium showed high catalytic activity.¹²⁶

Ladebeck and Kochloefl¹²⁷ in 1995 formulated another Cr-free catalyst containing about 5wt% Al₂O₃, 2wt% Cu and 2.5wt% CeO₂, ZrO₂, La₂O₃ or MnO. Initially these catalyst formulations showed high activity but with poor stability. In 1997, Kochloeft et al¹²⁸ found that iron oxide based catalyst containing 2.5wt% CeO₂ and 5wt% Al₂O₃ showed high activity for the WGS reaction. The incorporation of ZrO₂, La₂O₃ or MnO instead of CeO₂ led to high initial activity but exhibited poor stability.

Xue *et al*¹²⁹ in 1996 suggested that Pt/ZrO₂ catalyst have higher activity than that of a commercial catalyst. Even though these catalysts have good selectivity, they were deactivated in the presence of sulphur.

Later, zeolite supported catalysts¹³⁰ have been suggested and were found to be active catalysts for the WGS reaction. Combined Cu and Zn promoted catalysts are more active than a copper promoted catalyst. The authors suggested the role of zinc was probably to modify the distribution of copper species in the zeolite matrix. These catalysts were found to deactivate more rapidly which was one of their major drawbacks.

In 2000, Araujo and Rangel¹³¹ investigated the catalytic performance of Fe-Al catalysts with 3wt% Cu and these catalysts showed similar activity compared to the commercial Fe-Cr-Cu catalyst. Aluminium was found to increase the surface area of the catalyst¹³² acting as a textural promoter. The catalyst produces the active phase more easily and is resistant to further magnetite reduction. However, the stability of the catalyst is poor compared to the commercial catalyst. In addition, de Souza and Rangel^{133, 134} suggested that aluminium is a good replacement as it is non toxic and active.

Research was carried out along with non-Fe based catalysts. Nickolov and co-workers¹³⁵ investigated the effect of potassium on the texture and activity of Mo/Al₂O₃ catalysts. The authors found that the deposition of Mo onto K/Al₂O₃ led to a uniform distribution of oxomolybdenum species in the support and improved the

activity of the reaction at 400°C. Ni-Mo catalysts supported on Al₂O₃, TiO₂ and ZrO₂ were studied by Laniecki *et al*¹³⁶ who demonstrated that a Mo catalyst based on TiO₂ and Ni containing TiO₂ supports have the highest activity.

The ability of CeO₂ to promote precious metal catalysts for the WGS reaction has been known for many years¹³⁷. CeO₂ can store and release oxygen and hydrogen from intermetallic metal-Ce compounds¹³⁸. The Pt/CeO₂ catalyst is mainly used for the low temperature range. Choung *et al*¹³⁹ identified that Ceria promoted with Zr and Gd could improve WGS activity at temperature higher than 300°C. Ferrandon and co workers¹⁴⁰ studied these catalyst combinations further and conducted a study on Pt-Re, Pt-Co, Pt-Mo, Pt-Sn and Pt-Cu, supported on a zirconia doped ceria. The WGS activity of Pt alone, supported on zirconia and doped ceria was evaluated and it was found that Pt-Re and Pt-Co have higher activity than Pt and the Pt-Re catalyst is less prone to deactivation than the Pt-Co catalyst. Comparisons of WGS on ceria supported Pd, Pt and Rh catalysts by Bunluesin *et al*¹⁴¹ and Pd, Ni, Fe, Co and Pt catalysts by Hilaire *et al*¹⁴² suggested that even though all of them are effective promoters, the catalysts were deactivated due to the growth of ceria crystallites under high temperature calcinations.

Costa *et al*¹⁴³ 2002 conducted a study with thorium instead of chromium and found out that Fe-Th-Cu catalysts are more active than Fe-Cr-Cu catalysts at 370°C. The high activity of the catalyst is due to the increase in surface area. However, the radioactive nature of thorium will not be suitable to replace chromium by an environmentally friendly catalyst.

Ladebeck *et al*¹⁴⁴ in 2003 published recent catalyst developments for the WGS reaction including Ru/Fe₂O₃, Au/Fe₂O₃, Au/TiO₂ and precious metals supported on CeO₂ or ZrO₂. The authors pointed out that no WGS replacement catalyst satisfies all the requirements.

Liu *et al*⁷⁵ prepared oxides of Ce and Al to enhance the activity and stability of the commercial Fe-Cr catalysts. The authors used the maghemite phase instead of the

hematite phase and claimed that their catalyst had similar activity and thermal stability to the commercial catalyst.

Natesakhawat *et al*¹⁴⁵ investigated the Fe-Al-Cu/Co catalysts using BET surface area measurements, TPR, XRD, XPS and DRIFTS (diffuse reflectance infrared Fourier transform spectroscopy) and confirmed that the activity of the Fe-Al-Cu catalyst strongly depends on the preparation method.

Lim *et al*¹⁴⁶ have reported that platinum on ceria-zirconia catalysts displayed a high level of WGS activity. However, the surface area of the catalyst is far below that of the commercial catalyst. Recently Wilson *et al*¹⁴⁷(2009) reported that Pd/ZrO₂ catalysts are inactive for water gas shift due to its poor reforming nature.

Watanabe *et al*¹⁴⁸ have developed a solution-spray plasma (SSP) technique for the preparation of high temperature catalysts. The authors proposed a Ni-Fe-Al oxide formulation for the high temperature shift stage of the WGS reaction and claimed that these catalysts showed excellent catalytic activity with the suppression of the undesirable methanation reaction.

In 2009 Martos *et al*¹⁴⁹ studied the replacement of Cr by molybdenum and claimed that molybdenum increases the thermal stability of the catalyst and prevents the formation of metallic iron. However, the incorporation of molybdenum into the magnetite lattice gave rise to larger crystallite sizes and subsequently lower surface areas than the Fe-Cr catalysts. More recently Boudjemma *et al*¹⁵⁰ conducted a comparative TPR study of Fe-Cr-O and Fe-Mg-O catalysts and suggested magnesium promoted catalysts showed good activity however they could not predict the stability of the catalyst.

1.4.3 Summary of the Development of HT-WGS Catalysts

During the last decade, more active Cr-free catalysts have been under development for use in the HT-WGS process driven by the need for pure hydrogen in fuel cells and other applications and by impending EU legislation concerning Cr⁶⁺ toxicity. Even though many chromium free formulations have been suggested by different researchers, they are not yet proven in commercial usage and many have fallen short in terms of performance compared to the Fe-Cr system. In addition, some materials studied introduced their own toxic issues for example, thorium. However, a number of interesting ideas have been discussed. For example aluminium improves surface area relative to pure iron and it has thermal stability. In this thesis, atomistic computational modelling methods are applied for the better understanding of the role played by chromium in generating the appropriate catalyst particle size, surface morphology and surface chemistry and in promoting the fundamental reaction steps with the aim of identifying promising potential non-toxic alternatives to chromium. The main criteria is to identify a non-toxic metal dopant, which promotes the elementary catalytic reaction steps and inhibits unwanted processes such as thermal sintering and over reduction of the catalyst material.

1.6 References

- 1 M. V. Twigg, *Catalyst Handbook* Wolfe Publishing, London, 1989.
- 2 T. Chapman, *Physics World*, 2002, 152.
- 3 C. Ratnasamy and J. P. Wagner, *Catalysis Reviews*, 2009, **51**, 325.
- 4 D. S. Newsome, *Catalysis Reviews : Science and Engineering*, 1980, **21**, 275.
- 5 M. L. Kundu, A. C. Sengupta, G. C. Maiti, B. Sen, S. K. Ghosh, V. I. Kuznetsov, G. N. Kustova and E. N. Yurchenko, *Journal of Catalysis*, 1988, **112**, 375-383.
- 6 <http://www.icdachromium.com/pdf/publications/ICDAGuidelines.pdf>.
- 7 L. R. Lloyd, D. E.; Twigg, M. V. E., *Catalyst Handbook*, Wolfe Publications, London, 1989.
- 8 R. B. Anderson, *The Fischer-Tropsch Synthesis*, Academic Press, New York 1984.
- 9 N. A. Koryabkina, A. A. Phatak, W. F. Ruettinger, R. J. Farrauto and F. H. Ribeiro, *Journal of Catalysis*, 2003, **217**, 233-239.
- 10 L. Barreto, A. Makihira and K. Riahi, *International Journal of Hydrogen Energy*, 2003, **28**, 267-284.
- 11 C. Rhodes, B. Peter Williams, F. King and G. J. Hutchings, *Catalysis Communications*, 2002, **3**, 381-384.
- 12 L. Mond and C. Langer, *British Patent 12*, 1988, **12**, 608.
- 13 M. C. Kung and H. H. Kung, *Surface Science*, 1981, **104**, 253.
- 14 R. L. Keiski and T. Salmi, *Applied Catalysis*, 1992, **87**, 185.
- 15 B. Anilin and S. Fabrik., *Patents: EP 21151/1911; GP 254571/1911; 256296/1911; 259870/1911; 265295/1912*.
- 16 C. Rhodes, G. J. Hutchings and A. M. Ward, *Catalysis Today*, 1995, **23**, 43-58.
- 17 J. W. Lywood and M. V. Twigg, *Eur patent*, 1990, **0362648**.
- 18 M. I. Markina, G. K. Borekov, F. P. Ivanowski and L. Yudkovskaya, *Kinetics of Katalysis*, 1961, **2**, 867.
- 19 F.Domka, A.Basinska and R.Fielcrow, *Surface Technology*, 1983, **18**, 275-282.

-
- 20 A. Andreev, V. Idakiev, D. Mihajlova and D. Shopov, *Applied Catalysis*, 1986, **22**, 385.
- 21 T. Salmi, S. Boström and L. E. Lindfors, *Journal of Catalysis*, 1988, **112**, 345-356.
- 22 G. C. Chinchin, R. H. Logan and M. S. Spencer, *Applied Catalysis*, 1984, **12**, 89-96.
- 23 M. Chandra, S. S. Singh, B. Banerjee, A. K. Sinha and S. R. Ghosal, *Technology*, 1973, **10**, 208.
- 24 J. Hoogschagen and P. Zwietering, *Journal of chemical physics*, 1953, **21**, 2224.
- 25 P. Mars, *Chemical Engineering Science*, 1961, **11**, 275.
- 26 A. L. C. Pereira, G. J. P. Berrocal, S. G. Marchetti, A. Albornoz, A. O. de Souza and M. d. C. Rangel, *Journal of Molecular Catalysis A: Chemical*, 2008, **281**, 66-72.
- 27 E. Matijevic and P. Sheider, *J. Colloid Interface Science* , 1978, **63**, 509-524.
- 28 M. C. Rangel, M. S. Santos and A. Albornoz, *Studies in Surface Science Catalysis*, 2006, **162**, 753-760.
- 29 G. Doppler, A. X. Trautwein, H. M. Ziethen, E. Ambach, R. Lehnert, M. J. Sprague and U. Gonser, *Applied Catalysis*, 1988, **40**, 119-130.
- 30 E. F. Armstrong and T. P. Hilditch, *Proceedings of the Royal Society of London. Series A, Containing Papers of a Mathematical and Physical Character*, 1920, **97**, 265-273.
- 31 M. Tinkle and J. A. Dumesic, *Journal of Catalysis*, 1987, **103**, 65-78.
- 32 R. L. Keiski, T. Salmi, P. Niemistö, J. Ainassaari and V. J. Pohjola, *Applied Catalysis A: General*, 1996, **137**, 349-370.
- 33 C. V. Ovesen, P. Stoltze, J. K. Nørskov and C. T. Campbell, *Journal of Catalysis*, 1992, **134**, 445-468.
- 34 G. K. Boreskov, *Kinetics of Catalysis*, 1970, **11**, 374.
- 35 P. Liu and J. A. Rodriguez, *Journal of Chemical Physics*, 2007, **126**, 164705.
- 36 J. A. Rodriguez, P. Liu, J. Hrbek, J. Evans and M. Perez, *Angewandte Chemie, International Edition* , 2007, **46**, 1329.
- 37 G. Wang, L. Jiang, Z. Cai, Y. Pan, X. Zhao, W. Huang, K. Xie, Y. Li, Y. Sun and B. Zhong, *Journal of Physical Chemistry B*, 2003, **107**, 557.

-
- 38 L. C. Grabow, A. A. Gokhale, S. T. Evans, J. A. Dumesic and M. Mavrikakis, *Journal of Physical Chemistry C*, 2008, **112**, 4608-4617
- 39 A. A. Gokhale, J. A. Dumesic and M. Mavrikakis, *Journal of American Chemical Society*, 2008, **130**, 1402-1414.
- 40 N. Schumacher, A. Boisen, S. Dahl, A. A. Gokhale, S. Kandoi, L. C. Grabow, J. A. Dumesic, M. Mavrikakis and I. Chorkendorff, *Journal of Catalysis*, 2005, **229**, 265-275.
- 41 C. T. Campbell and K. A. Daube, *Journal of Catalysis*, 1987, **104**, 109-119.
- 42 D. C. Grenoble, M. M. Estadt and D. F. Ollis, *Journal of Catalysis*, 1981, **67**, 90-102.
- 43 R.V.Morris, D. G. Agresti, H. V. L. Lauer Jr., J. A. Newcomb, T. D. shelfer and A. V. Murali, *Journal of Geophysical Research*, 1989, **94**, 2760.
- 44 Y. Xiong, J. Ye, X. Gu and Q. Chen, *Journal of Magnetism and Magnetic Materials*, 2008, **320**, 107-112.
- 45 F. Yang, Y. Li, Z. Chen, Y. Zhang, J. Wu and N. Gu, *Biomaterials*, 2009, **30**, 3882-3890.
- 46 H. Duan, J. Gnanaraj, X. Chen, B. Li and J. Liang, *Journal of Power Sources*, 2008, **185**, 512-518.
- 47 S. Morzilli and B. Scrosati, *Electrochimica Acta*, 1985, **30**, 1271-1276.
- 48 R. M. Cornell and U.Schwertmann, *The Iron Oxides Structure, Properties, Reactions, Occurrence and Uses*, 1996.
- 49 L. Pauling and S. Hendricks, *Journal of American Chemical Society*, 1925, **47**, 781-790.
- 50 G. Shirane, S. J. Pickart, R. Nathans and Y. Ishikawa, *Journal of Physics and Chemistry of Solids*, 1959, **10**, 35-43.
- 51 M. P. J. Punkkinen, K. Kokko, W. Hergert and I. J. Vayrynen, *Journal of Physics: Condensed Matter* 1999, **11**, 2341-2349.
- 52 K. J. W. Atkinson, R. W. Grimes, M. R. Levy, Z. L. Coull and T. English, *Journal of the European Ceramic Society*, 2003, **23**, 3059-3070.
- 53 K. Hoshino and N. L. Peterson, *Journal of American Ceramic Society*, 1983, **66**, C202.
- 54 R. H. Chang and J. B. Wagner Jr, *Journal of American Ceramic Society*, 1972, **55**, 211-213.

-
- 55 K. Hoshino and N. L. Peterson, *Journal of Physics and Chemistry of Solids*, 1985, **46**, 1247-1254.
- 56 L. E. Eary and D. Rai, *American Journal of Science*, 1989, **289**, 180-213.
- 57 J. Wang and J. R. Rustad, *Geochimica Et Cosmochimica Acta*, 2006, **70**, 5285-5292.
- 58 M. Blanchard, M. Lazzeri, F. Mauri and E. Balan, *American Mineralogist* 2008, **93**, 1019-1027.
- 59 A. Bandyopadhyay, J. Velez, W. H. Butler, S. K. Sarker and O. Bengone, *Physical Review B*, 2004, **69**, 174429.
- 60 G. Rollmann, A. Rohrbach, P. Entel and J. Hafner, *Physical Review B*, 2004, **69**, 165107.
- 61 M. Catti, G. Valerio and R. Dovesi, *Physical Review B*, 1995, **51**, 7441.
- 62 G. K. Rozenberg, L. S. Dubrovinsky, M. P. Pasternak, O. Naaman, T. Le Bihan and R. Ahuja, *Physical Review B*, 2002, **65**, 064112.
- 63 S. Onari, T. Arai and K. Kudo, *Physical Review B*, 1977, **16**, 1717.
- 64 T. D. Glotch, P. R. Christensen and T. G. Sharp, *Icarus*, 2006, **181**, 408-418.
- 65 J. L. Rendon and C. J. Serna, *Clay Minerals*, 1981, **16**, 375-381.
- 66 Y. Wang, A. Muramatsu and T. Sugimoto, *Colloids and Surfaces A: Physicochemical and Engineering Aspects*, 1998, **134**, 281-297.
- 67 S. Mochizuki, *Physica Status Solidi (a)*, 1977, **41**, 591-594.
- 68 I. Chamritski and G. Burns, *Journal of Physical Chemistry B*, 2005, **109**, 4965-4968.
- 69 R. V. Gaines, H. C. W. Skinner, E. E. Foord, B. Mason, A. Rosenzweig and "Dana's new mineralogy", John Wiley & Sons, 1997.
- 70 K. Shi, L.-M. Peng, Q. Chen, R. Wang and W. Zhou, *Microporous and Mesoporous Materials*, 2005, **83**, 219-224.
- 71 A. H. Morrish and K. Haneda, *Journal of Magnetism and Magnetic materials*, 1980, **15-18**, 1089.
- 72 E. Matijević and M. Borkovec, *Surface and Colloid Science*, New York, 2004.
- 73 A. Basinska, L. Kepinski and F. Domka, *Applied Catalysis A: General*, 1999, **183**, 143-153.
- 74 D. E. Miser, E.-J. Shin, M. R. Hajaligol and F. Rasouli, *Applied Catalysis A: General*, 2004, **258**, 7-16.

-
- 75 Q. Liu, W. Ma, R. He and Z. Mu, *Catalysis Today*, 2005, **106**, 52-56.
- 76 D. Li, W. Y. Teoh, S. Cordelia, W. Robert, A. Rose and R. Bettina, *Chemistry of Materials*, 2006, **18**, 6403-6413.
- 77 G.W. Van Oosterhout and C. J. M. Rooijans, *Nature* **181**, 1958, **44**.
- 78 C. Greaves, *Journal of Solid State Chemistry*, 1983, **325**.
- 79 K. Haneda and A. H. Morrish, *Solid State Communications*, 1977, **22**, 779.
- 80 N. Shmakov, G.N. Kryukova, S.V. Tsibula, A.I. Chuvilin and L. P. Solovyeva, *Journal of Applied Crystallography*, 1995, **141**.
- 81 E. Schmidbauer and R. Keller, *Journal of Magnetism and Magnetic Materials*, 1996, **152**, 99.
- 82 G. M. da Costa, E. De Grave, R. E. Vandenberghe and P. M. A. De Bakker, *Clays and Clay Minerals*, 1994, **42**, 628.
- 83 Z. Somogyvari, E. Svab, G.M'esz'aros, K. Krezhov, I.Nedkov, I. Saj'o and F. Bour'ee, *Applied Physics A*, 2002, **74**.
- 84 J.-E. Jørgensen, L. Mosegaard, L. E. Thomsen, T. R. Jensen and J. C. Hanson, *Journal of Solid State Chemistry*, 2007, **180**, 180-185.
- 85 T. J. Bastow, A. Trinchi, M. R. Hill, R. Harris and T. H. Muster, *Journal of Magnetism and Magnetic Materials*, 2009, **321**, 2677-2681.
- 86 <http://www.solarnavigator.net/compass.htm>.
- 87 J. P. Wright, J. P. Attfield and P. G. Radaelli, *Physical Review B*, 2002, **66**, 214422.
- 88 J. B. Carlson, *Science*, 1975, **189**.
- 89 M. Imada, A. Fujimori and Y. Tokura, *Reviews of Modern Physics*, 1998, **70**, 1039.
- 90 W. H. Bragg, *Philosophical Magazine B*, 1915, **30**, 305-315.
- 91 R. J. Hill, J. R. Craig and G. V. Gibbs, *Physics and Chemistry of Minerals*, 1979, **4**, 317-339.
- 92 G. S. Parks and K. K. Kelley, *Journal of Physical Chemistry*, 1926, **30**, 47.
- 93 E. J. W. Verwey, *Nature*, 1939, **144**.
- 94 R. Bauminger, S. G. Cohen, A. Marinov, S. Ofer and E. Segal, *Physical Review*, 1961, **122**, 1447-1450.
- 95 L. Neel, *Annals of Physics (Leipzig)*, 1948, **3**, 137.
- 96 N.Nakagiri, M.H.Manghnani, L.C.Ming and S.Kimura, *Phys Chem Minerals*, 1986, **13**, 238-244.

-
- 97 W. C. Hamilton, *Physical Review*, 1958, **110**, 1050-1057.
- 98 M. E. Fleet, *Acta Crystallographica B*, 1981, **37**, 917-920.
- 99 M. Iizumi and G. Shirane, *Solid State Communications*, 1975, **17**, 433.
- 100 J. Yoshido and S. Iida, *Journal of Physical Society of Japan*, 1979, **47**, 1627.
- 101 M. Iizumi, T. F. Koetzle, G. Shirane, S. Chikazumi, M. Matsui and S. Todo, *Acta Crystallographica*, 1982, **B38**, 2121-2133.
- 102 J. Yoshida and S. Iida, *Journal of Physical Society of Japan*, 1977, **42**, 230.
- 103 J. M. Zuo, J. C. H. Spence and W. Petuskey, *Physical Review B*, 1990, **42**, 8451.
- 104 P. Novák, H. Å tÄpÃ;nkovÃ;j, J. Englich, J. Kohout and V. A. M. Brabers, *Physical Review B*, 2000, **61**, 1256.
- 105 M. Mizoguchi, *Journal of Physical Society of Japan*, 2001, **70**, 2333.
- 106 J. P. Wright, J. P. Attfield and P. G. Radaelli, *Physical Review Letters*, 2001, **87**, 266401.
- 107 P. A. Piekarz, K. Parlinski and A. M. OleÅ›, *Physical Review B*, 2007, **76**, 165124.
- 108 E. J. Palin and R. J. Harrison, *American Mineralogist*, 2007, **92**, 1334.
- 109 K. Yamauchi, T. Fukushima and S. Picozzi, *Physical Review B*, 2009, **79**, 212404.
- 110 Y. Hu, H. Jin, J. Liu and D. Hao, *Chemical Engineering Journal*, 2000, **78**, 147-152.
- 111 M. A. Edwards, D. M. Whittle, C. Rhodes, A. M. Ward, D. Rohan, M. D. Shannon, G. J. Hutchings and C. J. Kiely, *Physics and Chemistry of Chemical Physics*, 2002, **4**, 3902-3908.
- 112 V. Idakiev, D. Mihajlova, B. Kunev and A. Andreev, *Reaction Kinetics Catalysis Letters*, 1987, **35**, 119-124.
- 113 P. Kappen, J.-D. Grunwaldt, B. S. Hammershøi, L. Tröger and B. S. Clausen, *Journal of Catalysis*, 2001, **198**, 56-65.
- 114 H. Topsøe and M. Boudart, *Journal of Catalysis*, 1973, **31**, 346-359.
- 115 J. Tsagaroyannis, K. J. Haralambous, Z. Loizos, G. Petroustos and N. Spyrellis, *Material Letters*, 1996, **28**, 393-400.
- 116 Y. Lei, N. W. Cant and D. L. Trimm, *Catalysis Letters*, 2005, **103**, 133-136.
- 117 I. L. Júnior, J.-M. M. Millet, M. Aouine and M. do Carmo Rangel, *Applied Catalysis A: General*, 2005, **283**, 91-98.

-
- 118 W. Rarog-Pilecka and A. Magdziarz, *Przemysl Chemiczny*, 2007, **86**, 883-887.
- 119 G. C. Chinchen, *Euro Patent*, A-0 062410, 1982.
- 120 C. R. F. Lund and J. A. Dumesic, *Journal of Catalysis*, 1982, **76**, 93-100.
- 121 T.M. Yur'eva, G.K. Borekov, V.V. Popovskii, V. A. Chirginia and L. S. Egorova., *Kinetics of Katalysis*, 1971, **12**, 116.
- 122 D. G. Rethwisch and J. A. Dumesic, *Applied Catalysis*, 1986, **21**, 97-109.
- 123 F. M. Gottschalk, R. G. Copperthwaite, M. Van Der Riet and G. J. Hutchings, *Applied Catalysis*, 1988, **38**, 103-108.
- 124 G. J. Hutchings, R. G. Copperthwaitet, F. M. Gottschalk, R. Hunter, J. Mellor, S. W. Orchard and T. Sangiorgio, *Journal of Catalysis*, 1992, **137**, 408-422.
- 125 R. Hakkarainen, T. Salmi and R. L. Keiski, *Catalysis Today*, 1994, **20**, 395-408.
- 126 V. Kettmann, P. Balgavý and L. Sokol, *Journal of Catalysis*, 1988, **112**, 93-106.
- 127 J. Ladebeck and K. Kochloefl, *Studies of Surface Science Catalysis* , 1995, **91**, 1079.
- 128 K. Kochloefl, *Handbook of heterogeneous catalysis*, VCH, Germany, 1997.
- 129 E. Xue, M. O'Keeffe and J. R. H. Ross, *Catalysis Today*, 1996, **30**, 107-118.
- 130 T. Regina Oliveira de Souza, S. Modesto de Oliveira Brito and H. Martins Carvalho Andrade, *Applied Catalysis A: General*, 1999, **178**, 7-15.
- 131 G. C. Araujo and M.C.Rangel, *Catalysis Today*, 2000, **62**, 201.
- 132 H. Topsøe, J. A. Dumesic and M. Boudart, *Journal of Catalysis*, 1973, **28**, 477-488.
- 133 J. M. T. de Souza and M. do Carmo Rangel, *Reaction Kinetics and Catalysis Letters*, 2002, **77**, 29-34.
- 134 A. de Souza and M. do Carmo Rangel, *Reaction Kinetics and Catalysis Letters*, 2003, **79**, 175-180.
- 135 R. N. Nickolov, R. M. Edreva-Kardjieva, V. J. Kafedjiysky, D. A. Nikolova, N. B. Stankova and D. R. Mehandjiev, *Applied Catalysis A: General*, 2000, **190**, 191-196.
- 136 M. Laniecki, M. Malecka-Grycz and F. Domka, *Applied Catalysis A: General*, 2000, **196**, 293-303.

-
- 137 L. Mendelovici and M. Steinberg, *Applied Catalysis*, 1982, **4**, 237-243.
- 138 A. Trovarelli, F. Zamar, J. Llorca, C. d. Leitenburg, G. Dolcetti and J. T. Kiss, *Journal of Catalysis*, 1997, **169**, 490-502.
- 139 Choung.S.Y, K. J, F. M, R. Souleimanova, M. D and T. Krause, in *Hydrogen, fuel Cells, and Infrastructure Technologies, 2003 Merit Review*, Berkeley, CA, 2003.
- 140 S. Y. Choung, M. Ferrandon and T. Krause, *Catalysis Today*, 2005, **99**, 257-262.
- 141 T. Bunluesin, R. J. Gorte and G. W. Graham, *Applied Catalysis B: Environmental*, 1998, **15**, 107-114.
- 142 S. Hilaire, X. Wang, T. Luo, R. J. Gorte and J. Wagner, *Applied Catalysis A: General*, 2001, **215**, 271-278.
- 143 J.L. Rangle Costa, G. S. Marchetti and M. C. Rangel, *Catalysis Today*, 2002, 205.
- 144 J. R. Ladebeck and J. P. Wagner, *Catalyst development for water-gas shift. In: Vielstich W, Lamm A, Gasteiger HA, editors. Handbook of fuel cells.* , John Wiley & Sons, Chichester, 2003.
- 145 S. Natesakhawat, X. Wang, L. Zhang and U. S. Ozkan, *Journal of Molecular Catalysis A: Chemical*, 2006, **260**, 82-94.
- 146 S. Lim, J. Bae and K. Kim, *International Journal of Hydrogen Energy*, 2009, **34**, 870-876.
- 147 M. S. Wilson, *International Journal of Hydrogen Energy*, 2009, **34**, 2955-2964.
- 148 K. Watanabe, T. Miyao, K. Higashiyama, H. Yamashita and M. Watanabe, *Catalysis Communications*, 2009, **10**, 1952-1955.
- 149 C.Martos, J.Dufour and A. Ruiz, *Int. J. Hydrogen Energy*, 2009, **34**, 4475.
- 150 A. Boudjema, A. Auroux, S. Boumaza, M. Trari, O. Cherifi and R. Bouarab, *Reaction Kinetics and Catalysis Letters*, 2009, **98**, 319-325.

Chapter 2

METHODOLOGY

This chapter describes the theoretical methods used in this thesis. Computer modelling has developed into a valuable tool for the prediction and understanding the structure and stability of materials, especially at the atomic level where the available laboratory tools are not generally explicit. The modelling techniques can be divided into two categories: atomistic methods based on interatomic potentials (or forcefields) and electronic structure methods, solving to some approximation of the the fundamental quantum-mechanical equation proposed by Schrödinger¹.

Computer modelling techniques in combination with experiment can be implemented for the better understanding of catalyst systems. In this thesis, atomistic simulation techniques have been used to investigate bulk, surface and defect properties of three different types of technologically important iron oxide phases. GULP^{2, 3}(The General Utility Lattice Program) and METADISE⁴ (Minimum Energy Technique Applied to Dislocations Interface and Surface Energies) codes were used throughout this study.

2.1 The Potential Model

Atomistic simulation methods based on the Born model of ionic solids⁵ are employed in this thesis, which assumes that the ions in the crystal interact via long-range electrostatic forces and short-range forces, which include Pauli repulsions and vander Waals attractions between electron charge clouds. Simple analytical equations are used to describe the forces between atoms.

2.1.1 The Coulombic Potential

The lattice energy of the crystal is the sum of the interactions, between all atoms, which can be described by the equation,

$$U_{ij} = \sum_{ij} \frac{q_i q_j}{4\pi\epsilon_0 (r_{ij} + 1)} + \sum_{ij} \Phi_{ij} \quad (2.1)$$

where the first term in the equation represents the Coulombic or electrostatic interactions between charged species and the second term represents the short-range interactions between the ions. q_i and q_j are the charges on atoms i and j respectively, r_{ij} is the distance between the ions, ϵ_0 is the permittivity of free space and ‘1’ is the set of lattice vectors reflecting the periodicity of the lattice.

The long ranged coulombic interactions in periodic systems are calculated using the Ewald method⁶, where the Parry method^{7,8} a special application of Ewald method, which is used for surfaces and here ‘1’ represents the surface lattice vectors.

2.1.2 Ewald Summation

The electrostatic energy is an important term in many inorganic materials, particularly in oxides. The accurate evaluation of this energy is achieved through the Ewald summation⁶. This method is used to overcome the problems in the summation of the long-range coulombic interactions when the lattice is periodic. It can be expressed as the total sum of the real – space sum, the reciprocal or imaginary (Fourier) sum and the constant term known as the self-energy.

$$\Psi = \left[\frac{1}{2\pi V} \sum_{i,j}^N q_i q_j \sum_{m \neq 0} \frac{\exp(-(\pi m / \eta)^2 + 2\pi i m (r_i - r_j))}{m^2} \right] + \left[\frac{-\eta}{\sqrt{\pi}} \sum_{i=1}^N q_i^2 \right] + \left[\frac{1}{2} \sum_{i,j}^N \sum_n q_i q_j \frac{\text{erfc}(\eta r_{ij,n})}{r_{ij,n}} \right] \quad (2.2)$$

where η is the convergence parameter, which controls the distribution of the summation between real and reciprocal space. As η increases, the real-space sum converges more rapidly and the reciprocal sum more slowly. V is the volume, m is the reciprocal space vector, n is the cell co-ordinate vector and N is the number of particles. The self-term is a correction term, which cancels out the interaction of each of the introduced counter charges. $\text{erfc}(\eta r)$, is the complimentary error function^{9, 10} which can be evaluated and truncated in real space.

$$\text{erfc}(\eta r) = 1 - \text{erf}(\eta r) = \frac{2}{\sqrt{\pi}} \int_{\eta r}^{\infty} \exp(-u^2) du \quad (2.3)$$

2.1.3 Parry Method

The Parry method^{7, 8} is a modification of the Ewald summation for two-dimensional periodic systems such as surfaces. For the summation of the electrostatic interactions, the vectors are divided into in-plane vectors ρ_{ij} and vectors perpendicular to the plane, u_{ij} and are given by:

$$\psi = \frac{\pi}{A} \left[-2u_{ij} \text{erf}(\eta u_{ij}) - \frac{2 \exp(-\eta^2 u_{ij}^2)}{\eta \pi^{\frac{1}{2}}} + \sum_{k \neq 0} \frac{\exp(ik\rho_{ij})}{k} \left[\exp(ku_{ij}) \text{erfc}\left(\frac{k}{2\eta} - \eta u_{ij}\right) + \exp(-ku_{ij}) \text{erfc}\left(\frac{k}{2\eta} + \eta u_{ij}\right) \right] \right] \quad (2.4)$$

2.1.4 The Short Range Potentials

The most important contributions to the short-range potentials are from the two-body interactions, which are used to simulate two different effects: Pauli repulsions and van der Waals attractions between neighbouring electron charge clouds. The repulsive interactions arise when the electron distributions of a pair of ions overlap, when the ions get close to each other. The attractive force arises from the correlation of the electronic motion in different atoms. The common functional forms for interatomic potentials are:

Buckingham potential

When simulating ionic or semi-ionic solids¹¹, the most frequently used functional form for the short-range two body potential is the Buckingham potential which is given by the expression;

$$\Phi_{ij} = A_{ij} \exp(-r_{ij}/\rho_{ij}) - C_{ij}/r_{ij}^6 \quad (2.5)$$

where A_{ij} , and ρ_{ij} , are parameters specific to the interaction of the ions i and j represent the ion size and hardness, C_{ij} is the van der Waals constant and r_{ij} is the ion separation. When the C_{ij}/r_{ij}^6 term is omitted, the potential function is known as a Born-Mayer potential.

Lennard–Jones Potential

This widely used potential function for non-bonded interactions has the form;

$$\Phi_{ij} = \frac{A}{r_{ij}^{12}} - \frac{C}{r_{ij}^6} \quad (2.6)$$

The first term represents the Pauli repulsion term and the second the van der Waals attraction. The equilibrium separation depends on the variable parameters A and C . C in both Buckingham and Lennard-Jones potentials depends on the polarisability of the interacting ions as it represents the dipole-dipole interactions between the ions.

Morse Potential

This is a two body potential function where the energy is exponentially related to the interatomic spacing (r_{ij}) and the equilibrium distance (r_0). It is used for covalent bonding when distances can vary away from the equilibrium bond distance as it displays anharmonic behaviour. It has the form

$$\Phi_{ij} = D(1 - e^{-\alpha(r_{ij} - r_0)})^2 \quad (2.7)$$

where D is the dissociation energy of the molecule, measured from the potential minimum, and α controls the width of the potential well which can be obtained from spectroscopic measurements¹².

$$\alpha = \sqrt{\frac{k}{2D}} \quad (2.8)$$

where k is the bond force constant.

Harmonic Potential

This is the simplest of the two body functions and is proportional to the square of the difference of the separation of the two atoms from the equilibrium value.

$$\Phi_{ij} = \frac{k_{ij}}{2} (r_{ij} - r_0)^2 \quad (2.9)$$

where k_{ij} is the force constant between atoms i and j , r_{ij} is the distance between atoms and r_0 the equilibrium separation.

2.1.5 The electronic polarisability

Accurate calculations of the system energies generally require the inclusion of polarisable ions. The electronic polarisability of the ions is included via the shell model of Dick and Overhauser¹³, where an ion is treated as a flexible pair of charges. Each polarisable anion, here the oxygen ion, is represented by a core and a shell connected by a harmonic spring (**Figure 2.1**). The whole mass of the ion is in the core, which has a positive charge, and around the core there is a negatively charged massless shell. The total charge of the ion is the sum of the core charge and the shell charge. The polarisability (α) of the model ion is determined by the spring constant (k) and the shell charge (q).

$$\alpha = \frac{q^2}{k} \quad (2.10)$$

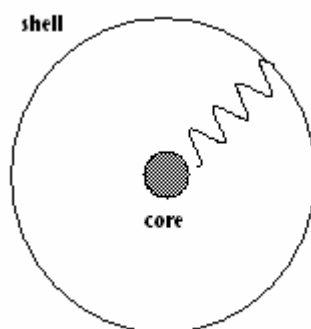


Figure 2.1: Schematic representation of the shell model

The parameters q and k are obtained by empirical fitting to dielectric data, elastic constants or phonon dispersion curves. Since polarisation is described in terms of the displacement of the shells relative to the core, the model includes the required coupling between short-range repulsion and polarisation.

The potential parameters used in this study were derived by Lewis and Catlow¹¹, and for water and hydroxide derived by de Leeuw and Parker^{14, 15} and are summarized in **Table 2.1**.

Buckingham Potential

Interaction	A (eV)	ρ (Å)	C (eV Å ⁶)
Fe2 – O	694.1	0.3399	0.0
Fe3 – O	1102.4	0.3299	0.0
Cr-O	1734.1	0.3010	0.0
Al-O	111.4	0.3299	0.0
Mn-O	1257.9	0.3214	0.0
Fe2 – OH	485.9	0.3399	0.0
Fe3 - OH	771.70	0.3299	0.0
Cr - OH	1213.9	0.3010	0.0
Fe2 - OW	277.64	0.3399	0.0
Fe3 - OW	441.00	0.3299	0.0
Cr - OW	693.6	0.3010	0.0
O– O	22764.3	0.1490	27.88
O – OH	22764.3	0.1490	13.94
O - OW	22764.3	0.1490	28.92
OH - OH	22764.3	0.1490	6.97
OH - OW	22764.3	0.1490	17.14
H - O	396.27	0.25	0.0
H - OH	311.97	0.25	0.0
H - OW	396.27	0.25	0.0
HW - O	396.27	0.25	0.0
HW - OH	311.97	0.25	0.0
HW - OW	396.27	0.25	10.0

Lennard-Jones Potential

	A (eV ¹²)	B(eV ⁶)
OW - OW	39344.98	42.15

Morse Potential

	D(eV)		
H - OH	7.0525	3.1749	0.9258

Harmonic Potential

O - O	27.29
-------	-------

Shell Charge: -2.21

Table 2.1: The potential set used in this study ^{11, 14-16} (Short-range cutoff 20 Å).

2.2 Energy Minimization

The basis of the simulation techniques is the calculation of the lattice energy of the system. The lattice energy is the energy released when the ions are brought together from infinite distance to their current lattice sites. The calculated lattice energy should be a minimum in order to describe a perfect crystal, which can be achieved in two ways:

Constant Pressure minimization: In this approach, the pressure is kept constant. The unit cell is repeated throughout space using periodic boundary conditions and the total energy is minimized by removing all strain through allowing relaxation of both the ions in the unit cell and the lattice vectors¹⁷.

Constant volume minimisation: when this approach is followed, no variation in the cell dimension is allowed as the volume is kept constant.

2.2.1 Optimisation Methods

There are many algorithms, which can be used to find a minimum energy structure from an initial configuration. Initially, a configuration is specified for a system, and the energy is calculated using interatomic potentials, which are a function of structural variables, x . Using an iterative scheme, the structure is then adjusted to attain the minimum energy configuration. Minimisation of a function of many variables can be classified into two groups: Those that

- i) require a gradient (First derivative) and a Hessian (Second derivative).
- ii) only require a gradient.

If the Hessian is available, the minimisation is achieved by a Newton-Raphson method.

The Newton-Raphson method is widely used in both perfect and defect lattice energy minimization, as it is rapidly convergent. This method requires the first and second derivatives of the energy in the minimisation procedure.

Consider locating the local energy minimum nearest to the initial input structure; the energy at a given point can be expanded as a Taylor series:

$$E(x + dx) = E(x) + E'(x)dx + \frac{1}{2}E''(x)dx^2 + \dots \quad (2.11)$$

where $E'(x)$ is the vector of first derivatives at x (gradient, g) and $E''(x)$ is the matrix of second derivatives (Hessian, H), where we terminate the Taylor expansion at the second order term by neglecting higher order terms. To estimate the vector dx from the current point to the energy minimum by differentiating,

$$dx = -H^{-1}g \quad (2.12)$$

The two drawbacks to this method are: a) the second derivative matrix is computationally expensive to calculate for large systems and b) if the Hessian is not positive, Newton-Raphson procedure will converge towards the maximum along any imaginary mode instead of the minimum.

If the Hessian is large, there is an alternative method, the conjugate gradient method¹⁸ which makes use of the first derivatives, does not require the use of hessian and is hence less compute-intensive, although less accurate.

Updating the algorithms can solve the second problem. A large number of methods have been evolved in which the inverse hessian is updated between cycles of minimisation based upon the gradient, g and position, x . The most widely used of these methods is the Davidon, Fletcher and Powell (DFP) method¹⁹. A later improved alternative is Broyden Fletcher Goldfarb and Shanno (BFGS) method²⁰. The methods largely differ in the degree in which the retention of positive definitivity of the inverse Hessian is guaranteed during updating.

2.2.2 Simulation Codes

The two computer simulation codes used in this study are GULP^{2, 3} (General Utility Lattice Program) and METADISE⁴ (Minimum Energy Technique Applied to dislocation Interface and Surface Energies)

GULP

The energetics and structures of the perfect and defective bulk lattices were calculated using the simulation code, GULP. Using the periodic boundary conditions, it employs the Mott-Littleton approach to calculate point defects, and supercell calculations for high defect concentrations, where an interaction between defects may exist. This code allows the minimisation of the lattice energy of the crystal in order to obtain the optimum ion coordinates and cell parameters at zero or finite temperature. Geometry optimizations were performed using the BGFS algorithm with a gradient tolerance of 10^{-8} .

METADISE

The lattice energies of the pure, defect and hydroxylated surface structures were calculated using the energy minimisation code METADISE, where periodic boundary conditions and sufficiently large supercells are employed to avoid surface and finite size effects and interactions between the repeating images. It allows the use of interatomic potentials to simulate not only the bulk structure but also the surfaces and interfaces of the material. When calculating the surface energies, it takes account of the two dimensional periodicity.

2.3 Defect Energy Calculations

We can obtain defect formation energies from the atomistic simulation studies. A defect can be a vacant lattice site, an atom in an interstitial position, as well as an impurity atom.

2.3.1 Point Defects

Point defects are defects in the crystal which include substitutional impurities, vacancies and self- or foreign interstitial atoms. Many properties (diffusion, conductivity, chemical reactions etc) are influenced by the existence of these point defects in inorganic solids. A convenient form of expressing these point defects is the Kröger-Vink notation²¹, which is used to describe the charge and position of the point defect in crystals. In this notation a defect is defined with respect to the perfect lattice and is described by three parts, a main symbol, a subscript and a superscript. The symbol is either the chemical symbol for the atom type or denotes a vacancy. The subscript denotes the perfect lattice site at which the defect is located, where (*i*) denotes an interstitial site. A superscript denotes the charge relative to the normal charge on this site.

(⁻) denotes an effective negative charge, (^x) a neutral defect and ([•]) denotes a positive charge.

For example,

$V_O^{\bullet\bullet}$ denotes an oxygen vacancy, whereas an oxygen interstitial is represented as $O_i^{\prime\prime}$.

Different types of point defects: Intrinsic and extrinsic disorders

The disorder in crystalline solids can be divided into two, depending on their stoichiometric compositions: intrinsic disorder and extrinsic disorder.

Intrinsic disorder occurs due to the temperature-dependent vibration of the lattice atoms and it varies with temperature²². As the temperature increases, contributions to the free energy due to the entropy term increases as a result of the number of atoms displaced from their lattice positions. Intrinsic disorder thus requires thermal activation, but the concentration of the defects remains constant.

The two common types of intrinsic disorder in the bulk structure of an ionic material are Frenkel²³ and Schottky^{24, 25} defects (**Figure 2.2**). The Frenkel defect involves a vacancy and an interstitial ion, where the two defects are at an infinite distance and therefore non-interacting. For a MO crystal, in the Kröger-Vink notation, the reaction for the creation of a Frenkel defect is



In a Schottky defect, ions of opposite charge are removed from the lattice in a stoichiometric ratio in order to keep the charge neutrality of the crystal. The Kröger-Vink notation for the reaction involving the creation of a Schottky defect in a MO crystal is:



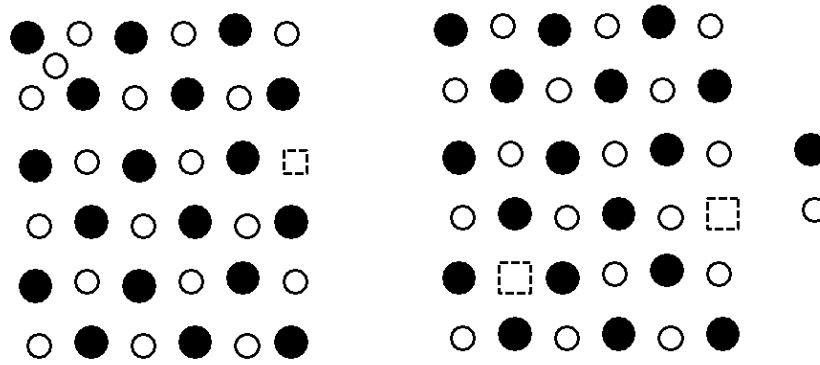


Figure 2.2: Left-hand figure is the Frenkel defect, where the dotted square denotes a vacancy left by a cation which has moved to an interstitial site. Right-hand figure shows a Schottky defect, where cation and anion vacancies are formed simultaneously to balance the charge.

Extrinsic disorder is caused by non-stoichiometry of the crystal, which includes defects resulting from oxidation or reduction reactions. The non-stoichiometry of the metal oxides can be subdivided into two categories: metal-deficient or oxygen-deficient. In metal-deficient oxides, if metal vacancies are formed, they are complemented by electronic defects, either increasing the valence states on metal sites or lowering the charge on oxygen sites or by a delocalized charge. For oxygen-deficient oxides, metal interstitials or oxygen vacancies will be the predominant defects.

Modelling Point defects

The two approaches to modelling of point defects within the crystal lattice are the Mott-Littleton method and Supercell approaches.

The Mott Littleton Method²⁶ is a well-established method for calculating the geometry and point defects in the bulk of ionic materials, where it uses a two-region approach (**Figure 2.3**). A defect is placed at a defined point and the crystal around the defect centre is divided into two spherical regions, where the inner sphere is labelled as region I and the outer sphere is region II. Region I extends from the centre to a predetermined radius and within region I, all ions can relax to zero force and interactions can be calculated explicitly. Region II is further subdivided into region IIa and IIb, where IIa acts as the transition between regions I and II. Region IIb extends to infinity. In region IIa, ions are present but they are kept at their equilibrium position without further relaxation due to the defect. Region I needs to be large enough to avoid strains at the I-IIa boundary. For example, the radius has a direct impact on the accuracy of calculation of the defect energy²⁷. For larger ions a bigger region size is needed for maximum convergence. This method can be used to study the defects in infinite dilution.

The total energy can be calculated,

$$U_{tot(x,\xi)} = U_{1(x)} + U_{12(x,\xi)} + U_{2(\xi)} \quad (2.15)$$

where, $U_1(x)$, $U_2(\xi)$: Energy of region 1 and 2.

$U_{12}(x,\xi)$: Energy of interaction between the two regions.

x, ξ : Displacements of the region 1 and 2 respectively.

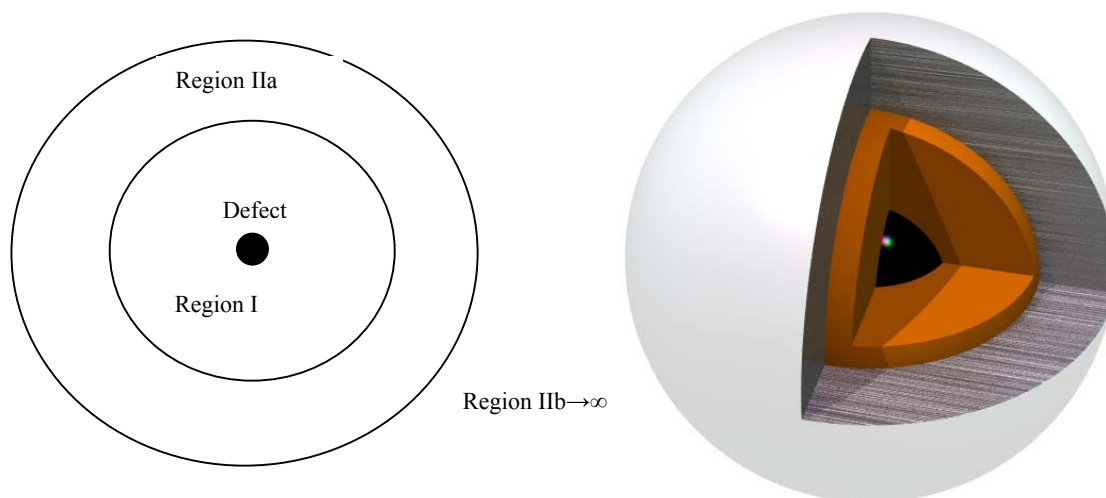


Figure 2.3: A schematic representation of the two-region approach (left). The right figure²⁸ shows a three-dimensional representation of the Mott-Littleton set-up, where the inner black sphere represents a defect, the orange sphere represents the boundary of Region I, the grey sphere Region IIa, while Region IIb extends to infinity.

In supercell calculations, a supercell is constructed from the primitive unit cell which is repeated throughout space, using periodic boundary conditions²⁹. These boundary conditions allow the supercell to wrap around on itself and as an ion moves out of one side of the supercell it simultaneously moves back in through the opposite side (**Figure 2.4**). The Coulombic summation will diverge if the system is not charge - neutral.

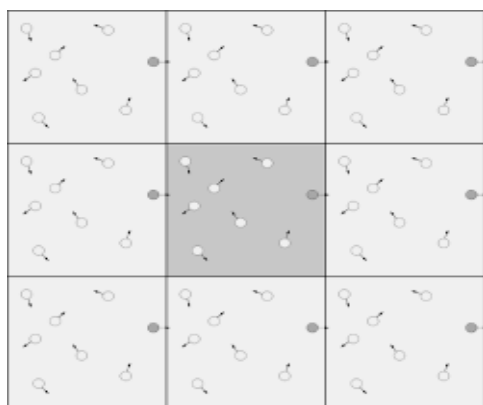


Figure 2.4: Schematic representation of supercell approach

Supercell calculations are usually employed to calculate higher defect concentrations. From the total lattice energy generated, the defect energy can be calculated by comparing the defect lattice with the perfect lattice using a suitable energy cycle. The defect energy involved in this process is then converted to solution energy to enable the substitution of different cations to be compared directly.

Mean Field Approach

One of the main problems of simulating complex materials is that they are often partly disordered systems or involve partial occupancies of sites. Mean Field Theory is often used to treat these partial occupancies. In this work, the mean field approach in Gulp was used to model magnetite, where in addition to the coordinates the site occupancies can be specified.

According to the mean field approach, each site experiences a potential, which is the mean of all possible configurations at the disordered positions. Therefore all the interactions can be scaled by the site occupancies of the atoms, it is assumed here that there is an equal possibility of finding less stable and most stable configurations, which will apply to materials where there is little energetic difference between

configurations. If two different ions share one site with partial occupancies, they can be treated as a single ion and the total occupancy on the site does not exceed unity. If two different partially occupied sites are very close to each other, then their occupancy would be mutually exclusive and in this case, it is necessary to exclude potentials between these atoms to obtain the correct behaviour.

2.3.2 Simulating Site Occupancy Disorder in Ionic Solids

Non-periodic occupation of lattice sites in a crystal is a common problem in solid state chemistry. Computer modelling techniques can be applied to investigate the structural disorder in solids. One of the strategies^{30, 31} being employed in this work is the evaluation of the energies of different configurations in a supercell structure. This has many limitations, for example the computational expense of large supercells and the large numbers of possible configurations. An alternative scheme³² is the mixing of potentials, but this model may not simulate the energy of mixing. Recently Todorov *et al*³³ discussed an approach based on the determination and comparison of space groups. The methodology for calculating the required configurational averages and entropies has been explained by Todorov *et al* and the technique has recently been adapted to operate in the reduced space of all the inequivalent configurations.³⁴ In this study the system symmetry is used to reduce the number of configurations as suggested by Grau-Crespo *et al*.³⁴ This procedure typically reduces the size of the configurational space by one or two orders of magnitude, which is often enough to make the problem tractable^{30, 35, 36}.

The investigation of configurational effects in solid solutions using computer simulations methods is complicated by the large number of possible configurations that can exist for a particular supercell. In order to overcome this problem, the complete configurational space for each composition of the supercell is generated, before extracting the subspace of symmetrically inequivalent configurations. The methodology is implemented in a computational

program, SOD³⁴ (Site Occupancy Disorder) which identifies the different site occupancy configurations. The criterion for the equivalence of two configurations is the existence of an isometric transformation that converts one configuration into the other. The transformations considered are the symmetry operators of the parent structure (the structure from which all configurations are derived via site substitutions). The methodology is based on the assumption that the extent of occurrence of one particular configuration in the disordered solid can be described by a Boltzmann-like probability (P_m) which, ignoring the vibrational or external pressure effects, can be calculated from the energy of the configuration (E_m), and its degeneracy (Ω_m , the number of times that the configuration is repeated in the complete configurational space):

$$\tilde{P}_m = \frac{1}{Z} \Omega_m \exp(-E_m / k_B T) = \frac{1}{Z} \exp(-\tilde{E}_m / k_B T) \quad (2.16)$$

where $m=1, \dots, M$ (M is the number of inequivalent configurations), $k_B=8.6173 \times 10^{-5}$ eV/K is Boltzmann's constant,

$$Z = \sum_{m=1}^M \exp(-\tilde{E}_m / k_B T) \quad (2.17)$$

is the configurational partition function, and we have introduced the reduced energy:

$$\tilde{E}_m = E_m - T\tilde{S}_m \quad (2.18)$$

which can be seen as a temperature-dependent free energy associated with the degeneracy entropy:

$$\tilde{S}_m = k_B T \ln \Omega_m \quad (2.19)$$

The above equations can be generalised in terms of finite temperatures and pressures if the vibrational Gibbs free energy of each configuration is used instead of its energy, to calculate the probability of occurrence. The extension is straightforward, and is well explained by Todorov *et al*³³. In the present work the pressure effects are not considered, but the role of vibrations has been

carefully investigated by comparing the results with and without vibrational calculations. In order to simplify the notation, the symbol E_m is used to denote either the energy or the vibrational free energy characterising the stability of each configuration, while the symbol G is reserved for the configurational free energy. The average value of E_m at each composition can be calculated as:

$$E = \sum_{m=1}^M \tilde{P}_m E_m \quad (2.20)$$

while the configurational free energy G can be obtained directly from the partition function:

$$G = -kT \ln Z \quad (2.21)$$

Configurational entropy is a measure of the degree of disorder in a system.

The configurational entropy at any temperature and composition can then be obtained as:

$$S = \frac{E - G}{T} = -k_B \sum_{m=1}^M \tilde{P}_m \ln \tilde{P}_m + \sum_{m=1}^M \tilde{P}_m \tilde{S}_m \quad (2.22)$$

where two limiting cases are of particular interest:

- i) when there is one non-degenerate configuration much more stable than the rest (for example, the perfect ordering case, Al-Fe₂O₃ system), the system will have zero configurational entropy;
- ii) in the limit $T \rightarrow \infty$, or when all the energies E_m are the same, the configurational entropy reaches its maximum value:

$$S_{\max} = k_B \ln N = k_B \ln \frac{(N_{\text{sites}})!}{(xN_{\text{sites}})!(N_{\text{sites}} - xN_{\text{sites}})!} \quad (2.23)$$

where $N = \sum_{m=1}^M \Omega$ is the total number of configurations for the given composition (including equivalent configurations), N_{sites} is the total number of sites in the cell and x is the fraction of sites which have been substituted. In the evaluation of configurational entropy it is common to employ this last expression, or its approximation for an infinite cell ($N_{\text{sites}} \rightarrow \infty$) based on the Stirling formula^{37, 38}

$$S_{\infty} = k_B N_{\text{sites}} (-x \ln x - (1-x) \ln(1-x)) \quad (2.24)$$

Equations (2.23) and (2.24) are only applicable in the limit of ideal or perfectly disordered solid solutions. In this work there are no assumptions made regarding the degree of ordering of the solid solution for the computation of the configurational entropy, and therefore, the more general equation (2.22) has been employed. The calculations in this thesis show that the solid solutions are highly disordered at most temperatures of interest, and the results from the evaluation of (2.22) are very close to those obtained from the maximum entropy expression (2.23), which can be extrapolated to an infinite cell using equation (2.24).

The effect of configurational contributions and the vibrational contributions, which are normally responsible for thermal effects in the cell size, are included. Using vibrational free energies instead of energies or enthalpies in the equation for the configurational probabilities can incorporate these effects. Vibrational free energies were obtained using a Monkhorst-Pack scheme³⁹ (see section 2.3.3). Finally, not only energies but any other average observable A can be estimated, by analogy to equation (2.20), through configurational averaging:

$$A = \sum_{m=1}^M \tilde{P}_m A_m \quad (2.25)$$

This is a significant advantage of this methodology in comparison with others where a simplified interaction model is employed to compute only the energy of each configuration. A full set of properties for each calculated configuration (e.g. cell parameters or mechanical properties) can be accessed, that define the configurationally averaged observable $\vec{a}_m, \vec{b}_m, \vec{c}_m$ values via equation (2.25). However, if the averaging is performed in the reduced space of inequivalent configurations, each configuration m represents a set of Ω_m equivalent ones, and therefore the property A_m must be the same for all configurations in that set. For example, if \vec{a}_m are the equilibrium cell vectors for each inequivalent configuration m , the average value of the cell parameter a corresponding to the disordered crystal cannot be calculated as the direct average of the a_m values. The obtained result could be different from the direct average of the b_m values, breaking the rotational symmetry of the cell. Therefore the a cell parameter is calculated as:

$$a = \frac{2}{\sqrt{3}} \left(\sum_{m=1}^M \tilde{P}_m |\vec{a}_m \times \vec{b}_m| \right)^{1/2} \quad (2.26)$$

since the absolute value of the vector product $|\vec{a}_m \times \vec{b}_m|$ is invariant within a set of equivalent configurations. The cell volumes V_m are also invariant within each set of equivalent configurations and therefore its average value V can be obtained directly following the general equation (2.24), while the average c parameter can then be obtained as.

$$c = 2V / \sqrt{3}a^2 \quad (2.27)$$

This procedure provides consistent values of a , c and V as functions of composition and temperature.

2.3.3 Vibrational Free energies : Monkhorst-Pack Scheme

GULP uses a standard scheme developed by Monkhorst and Pack³⁹ to determine the suitable k-points for the calculations following the periodic boundary conditions. This is based on three shrinking factors, n_1 , n_2 and n_3 – one for each reciprocal lattice vector. These specify the number of uniformly spaced grid points along each direction. It is important to ensure that the calculated properties, here the free energy, are well converged with respect to the shrinking factors. Vibrational free energies are calculated using this scheme with a 3x3x1 partition for the integration across the Brillouin zone related to the hematite unit cell, which was sufficient to converge the free energies with respect to the number of k points. The program is capable of computing analytical derivatives of the vibrational free energies, making the finite temperature geometry optimizations more efficient⁴⁰.

2.3.4 Spin Models of Cation Ordering

Spin models can be derived for complex systems by analogy with magnetic systems. If ‘ S ’ is the magnetic moment, the interaction between two moments i and j can be expressed through an Ising-type⁴¹ Hamiltonian in the form,

$$H_{mag} = -2\sum_{i,j} J_{ij} S_i S_j \quad (2.28)$$

Where J_{ij} is the superexchange coupling constant between a pair of neighbouring magnetic ions with spins S_i and S_j and the sum goes over all the pairs. The coupling constant depends on the separation of the magnetic ions. In a metal the direction of any moment S_j can be free to rotate, but in many crystals, S_j lie along preferred directions by the local fields. In an Ising Model, S_j is constrained to lie along in only one direction so that it can only point up or down. A simple way to estimate the effect of magnetic interactions for each configuration is given by an Ising-type Hamiltonian model and this model turns out to be a useful representation of cation site ordering.

2.4 Surface

The surface of a material is as important as the bulk because the surface properties control the interaction between the bulk and the outside environment. For in-depth investigation of a material, the understanding of the nature of surfaces is essential. The surface energy γ is the energy required to produce a surface or cleave a crystal into surfaces. It is defined as the difference in energy between the surface and an equivalent number of bulk ions and is calculated using the equation,

$$\gamma = \frac{(E_{surf} - E_{bulk})}{Area} \quad (2.29)$$

A stable surface has a small positive value of γ .

2.4.1 Types of Surfaces

According to Tasker⁴², a crystal is considered to consist of a stack of charged planes with three different types of surfaces. In Type I, (**Figure 2.5**, left) each layer consists of equal number of anions and cations, maintaining a stoichiometric ratio with an overall net charge of zero and zero net dipole perpendicular to the surface. In Type II, (**Figure 2.5**, right) the surface has charged planes, but the repeat unit consists of several planes in a symmetrical configuration, and there is no resulting charge or dipole moment perpendicular to the surface.

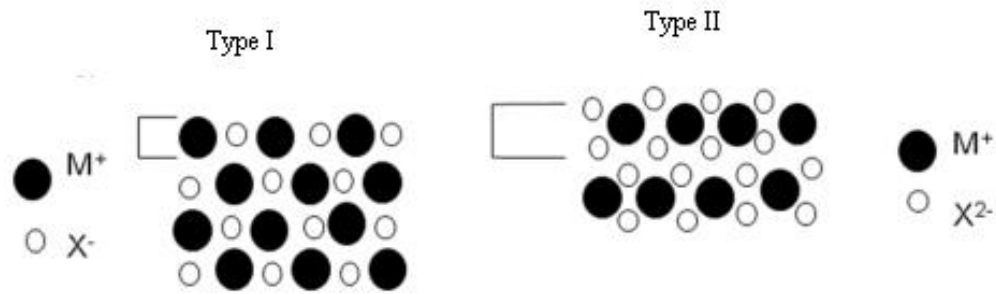


Figure 2.5: Type I surface consist of neutral layers of ions, Type II surface consisting of both cations and anions with charge neutral non-dipolar repeat unit.

In type III (**Figure 2.6**) surfaces, the stack of charged planes produces a net dipole moment perpendicular to the surface. When a dipole moment is perpendicular to the surface of a unit cell, its surface energy diverges and is infinite⁴³. In order to remove the surface dipole, half of the ions from the surface layer at the top of the repeat unit are shifted to the bottom layer resulting in the formation of a surface, which is partially vacant in either cations or anions. These partially vacant surfaces are usually very unstable and reactive towards impurities or the addition of water and are often found to reconstruct into different surface geometries.

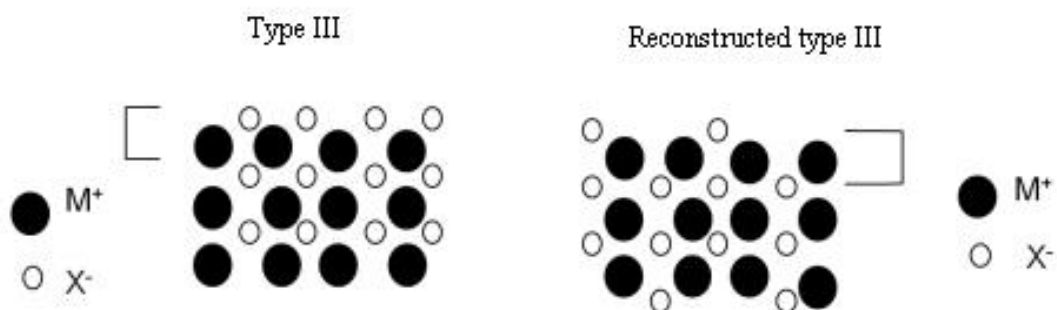


Figure 2.6: Type III surface consists of alternate layers of cations and anions results a net dipole, reconstructed surface with zero total dipole perpendicular to the surface.

2.4.2 Modelling the Surfaces

The two approaches considered for the modelling of solid surfaces use either two-dimensional or three-dimensional simulation cells. In both cases periodic boundary conditions are employed, which are effective for the computer modelling of solid surfaces to limit the computer time required to model a system of realistic size. Periodic boundary conditions allow a finite number of particles to generate behaviour by mimicking an infinite system in such a way that an infinite number of images are produced from the original cell in either two or three dimensions. In this study, we model surfaces using two dimensional simulation cells.

In the computer simulation code, METADISE⁴, the crystal is divided into two blocks, block I and block II (**Figure 2.7**) and each block is further divided into two regions, region I and region II where region I represents the surface. The ions in region I are allowed to relax explicitly while in region II they are held fixed at their equilibrium positions and may move as a whole. The two regions are allowed to move in relation to each other. It is essential to include region II to ensure the potential of an ion in the bottom of region I is modelled correctly and the energies are fully converged. A surface is created when block II is removed with the top of region I as the free surface.

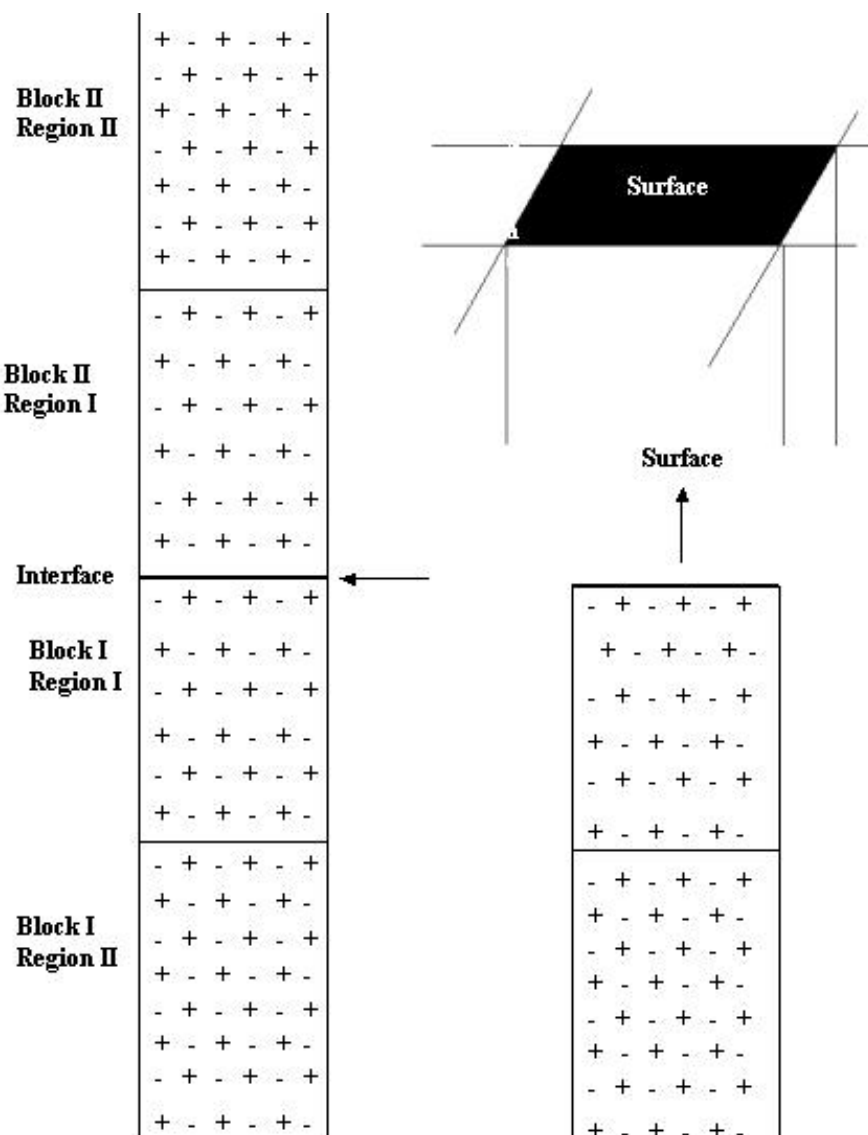


Figure 2.7: The two-region approach, complete crystal (left), half a crystal, exposing the surface (right).

2.4.3 Surface Defects

Again, there are two approaches to model surface defects, *the Supercell approach* and *Isolated effects*. In the supercell approach any defects in the bulk or surface are periodically repeated laterally in the crystal. The *Isolated defects* approach is used for modelling defects such as charged vacancies or adsorbed molecules and is a modification of the Mott-Littleton method for bulk defects. The crystal is divided into region I and II. Region II is again subdivided into two regions region IIa and IIb. The interactions between the regions are modified to include a charge-induced dipole to offset the charge of the defect and defect energy is calculated with respect to the relaxed surface.

Segregation

Segregation is the movement of a species towards or away from a surface, interface or boundary. Significant segregation of impurities can change the surface composition and hence its properties. The segregation energy is defined as the energy difference between placing an impurity in the surface with that of placing the same impurity in the bulk.

$$\text{Segregation Energy, } E_{\text{seg}} = E_{\text{def}}(\text{surf}) - E_{\text{def}}(\text{bulk}) \quad (2.30)$$

$$\text{The defect surface energy, } \gamma_{\text{def}} = \gamma_{\text{pure}} + E_{\text{seg}} \cdot X_0 \quad (2.31)$$

where X_0 , is the number of defect atoms per area.

2.4.4 Hydroxylated Surfaces

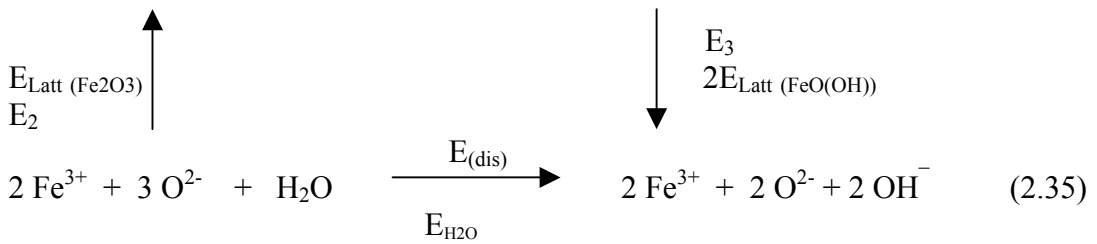
As water plays an important role on surfaces, the effect of surface hydroxylation is investigated, which can have a significant effect on the surface structure. Usually, there is a strong interaction between water and ionic surfaces. As the most stable surface structure has the lowest surface energy, the difference in surface energy between the dry and hydroxylated surface provides on which surfaces are stabilised by the reaction with water. In this study we consider the adsorption of one molecule of dissociated water. When a water molecule dissociates on the surface of Fe_2O_3 , the OH will be bonded to the cation and the proton will bind to a surface oxygen atom. The surface energies of the hydrated surfaces are defined by⁴⁴:

$$\gamma_{hydrated} = \frac{(E_{s+water} - nE_{water} - E_b)}{A} \quad (2.32)$$

where $E_{s+water}$ is the energy of the surface with adsorbed water, E_{water} is the energy of the water molecule, n is the number of water molecules, in this case, $n=1$, E_b is the bulk energy containing same number of atoms as the surface block and A is the surface area. The dissociation energy of the water molecule,



is calculated from an energy cycle as follows:



where E_l is the enthalpy of the reaction (eqn. 2.34), which can be calculated from the formation energies of Fe_2O_3 (-8.54 eV), $\text{FeO}(\text{OH})$ (-5.82 eV) and H_2O (-2.96 eV),⁴⁵ which was calculated as -0.14 eV, E_2 and E_3 are the calculated lattice energies of Fe_2O_3 and $\text{FeO}(\text{OH})$, ie, -150.37 and -71.7 respectively.

$$\text{Dissociation Energy, } E_{(dis)} = E_1 + E_2 - E_3 \quad (2.36)$$

This energy of dissociation of one molecule of water, -7.1 eV is used to calculate the energy released upon the adsorption of one molecule of water on the hematite surface. Therefore the adsorption energy can be calculated as,

$$E_{ads} = E_{s+water} - E_s + E_{dis} \quad (2.37)$$

where $E_{s+water}$ and E_s are the lattice energies of the hydroxylated and dehydrated surfaces obtained from the simulations.

2.4.5 Crystal Morphology

According to Wulff⁴⁶, the equilibrium shape of the crystal that minimises the total free energy of the system. When a crystal is in its equilibrium shape, the height of a face is directly proportional to its specific free energy and this ratio is constant. If σ_i is the specific free energy of the i^{th} plane, and h_i is the distance from the centre of the crystal to the i^{th} plane⁴⁷ this can be expressed as

$$\frac{\sigma_1}{h_1} = \frac{\sigma_2}{h_2} = \frac{\sigma_3}{h_3} = \frac{\sigma_n}{h_n} \quad (2.36)$$

According to Gibbs⁴⁸, the equilibrium morphology of a crystal structure is the morphology that minimises the surface free energy for a given volume. If two faces have the same specific surface energy, they will have the same area. The surface with highest surface energy will grow faster, resulting in a small surface area with a longer distance from the centre, while the surface with a lower surface energy will grow more slowly resulting in a larger surface area or short distance from the centre and this surface will be expressed in the crystal morphology.

$$\gamma = \sum_i \gamma_i A_i \text{ minimum for constant volume.} \quad (2.37)$$

where γ_i is the surface energy of the i^{th} surface and A_i is the surface area.

When using static lattice simulations, the surface free energy is a close approximation of the surface energy at 0 K as the entropy term is small compared to the enthalpy term. Thus, the surface energies can be assumed to determine the equilibrium morphology of the crystal. The crystal morphology represents the relative surface stabilities and it will depend on a wide variety of factors, such as pH, ionic strength, and supersaturation. The INSIGHT II program is used to generate the equilibrium morphologies of the crystals in this work.

2.5 Summary

This chapter has described with the methods and techniques employed throughout this study, including the interatomic potentials used to describe the interactions in the bulk and the surface. Atomistic simulations are widely used in the prediction of equilibrium structures, physical properties, defects, and surface stability.

In the next session, the bulk and a number of low index surface structures of hematite are modelled and we explore the system in an aqueous environment, where the results are compared with experiment.

2.6 Reference

1. E.Schrodinger, *Annals of Physics*, **1926**, 79, 361.
2. J.D.Gale, *Philosophical Magazine B*, **1996**, 73.
3. J.D.Gale, *Journal of Chemical Society, Faraday Transactions*, **1997**, 93.
4. G W Watson; E Toby Kelsey; Nora H de Leeuw; Duncan J Harris; S. C. Parker, *Journal of Chemical Society, Faraday Transactions*, **1996**, 92, (3), 433-438.
5. M Born; K. Huang., *Oxford* **1954**.
6. P. P. Ewald, *Annalen der Physik*, **1921**, 64, 253.
7. D. E. Parry, *Surface Science*, **1975**, 49, 433.
8. D. E. Parry, *Surface Science*, **1976**, 54, 195.
9. C. R. A. Catlow; M. J. Norgett, *personal communication*, **1976**.
10. N. Karasawa; W. A. Goddard, III *Macromolecules* **1992**, 25, 7268.
11. G.V.Lewis; C. R. A. Catlow, *Journal of Physics, C;Solid state Physics*, **1985**, 18, 1149-61.
12. P. M. Morse, *Physical Review* **1929**, 34, (1), 57.
13. B.G. Dick; A. W. Overhauser, *Physical Review*, **1958**, 112, 90-103.
14. N. H. de Leeuw; S. C. Parker, *Physical Review B*, **1998**, 58, (20), 13901.
15. P. S. Baram; S. C. Parker, *Philosophical Magazine B*, **1996**, 73, 49.
16. C. R. A. Catlow, *Proceedings of Royal Society of London A*, **1977**, 353.
17. C. R. A. Catlow, *Computer modelling in Inorganic Crystallography*. Academic Press Limited: 1997.
18. R. Fletcher; M. J. D. Powell, *Computer Journal*, **1963**, 6, 163.
19. R. Fletcher, *Practical Methods of Optimisation*. Wiley: New York, 1980.
20. W. H. Press; S. A. Teukolsky; W. T. Vetterling; B. P. Flannery, *Numerical Recipes*. 2 ed.; Cambridge University Press: Cambridge, 1992.
21. H. Kröger F.A and Vink, *Journal of Solid state Physics*, **1956**, 3, 307.
22. J. Nölting, *Angewandte Chemie International Edition in English*, **1970**, 9, (7), 489-500.
23. J. Frenkel, *Zeitschrift fur Physik*, **1926**, 35, 652.
24. W.Schottky; C. Wagner, *Zeitschrift fur Physik Chemie*, **1930**, 11B, 335.

25. W. Schottky, *Zeitschrift fur Physik Chemie*, **1935**, 29B, 335.
26. Mott.N.F; Littleton.M.J, *Transactions Faraday Society*, **1938**, 34, 485.
27. R. A. Jackson; R. D. Murray; J. H. Harding; C. R. A. Catlow, *Philosophical magazine A* **1986**, 53, (1), 27-50.
28. C. R. Stanek, **2003**.
29. C. R. A. Catlow; E.Kotomin, *Computational Materials Science*. IOS Press: 2001.
30. Z. Du ; N. H. de Leeuw; R. Grau-Crespo; P. B. Wilson; J. P. Brodholt; M. Calleja; M. T. Dove, *Molecular Simulations*, **2005**, 31, 339.
31. A. Bosenick; M. T. Dove; V. Heine; C. A. Geiger, *Physics and Chemistry of Minerals*, **2001**, 28, 177.
32. B. Winkler; M. T. Dove; M. Leslie, *American Mineralogist*, **1991**, 76, 313.
33. I. T. Todorov; N. L. Allan; M. Y. Lavrentiev; C. L. Freeman; C. E. Mohn; J. A. Purton, *Journal of Physics-Condensed Matter*, **2004**, 16, (27), S2751-S2770.
34. R. Grau-Crespo; S. Hamad; C. R. A. Catlow; N. H. de Leeuw, *Journal of Physics-Condensed Matter*, **2007**, 19, 256201.
35. R. Grau-Crespo; C. R. A. Catlow; N. H. de Leeuw, *Journal of Materials Chemistry*, **2003**, 13, 2848.
36. R. Grau-Crespo; C. R. A. Catlow; N. H. de Leeuw, *Chemistry of Materials*, **2004**, 16, 1954.
37. L. Farber; M. Matjaz Valant; M. A. Akbas; P. K. Davies, *Journal of the American Ceramics Society*, **2002**, 85, (9), 2319 - 2324.
38. J. A. L. Rabone; N. H. de Leeuw, *Journal of Computational Chemistry*, **2006**, 27, (2), 253-266.
39. H. J. Monkhorst; J. D. Pack, *Physical Review B*, **1976**, 13, 5188.
40. J. D. Gale, *Journal of Physical Chemistry B*, **1998**, 102, 5423.
41. E. Ising, *Zeitschrift fur Physik*, **1925**, 31, 253-258.
42. P. W. Tasker, *Journal of Physics solid state Physics*, **1979**, 12, 4977.
43. F. Bertaut, *Compute Rendus*, **1958**, 246, 3447.

-
44. N. H. de Leeuw; T. G. Cooper, *Geochimica et Cosmochimica Acta*, **2007**, 71, 1655-1673.
 45. D. R. Lide, *CRC Handbook of Chemistry and Physics*, CRC Press: 1999.
 46. G. Wulff, *Zeitschrift fur Kristallography*, **1901**, 34, 449-530.
 47. V. L. Tauson, M. G. Abramovich, V. V. Akimov, *Geochimica et Cosmochimica Acta*, **1993**, 57, (4), 815.
 48. J. W. Gibbs, Longman: New York, **1928**.

Chapter 3

Hematite: Bulk, Surfaces and Defects

3.1 Introduction

This chapter describes the simulations to characterise the bulk and different types of low index surface structures of pure haematite (α -Fe₂O₃). Hydroxylation has a significant effect on iron oxide surfaces and may affect the catalytic performance. To find out the impact of water on these surfaces, calculations are performed with dissociated water molecules.

Fe₂O₃-Cr₂O₃ catalysts are used exclusively in the high temperature stage of the WGS reaction. The potential toxic effects of chromium make it important to seek an efficient and improved catalyst. Firstly, studies are conducted to gain an understanding of the behaviour and influence of chromium on the hematite system and establish the criteria for a good catalyst. The effect of different isovalent metal dopants on the same system are analysed as a preliminary stage to conduct more detailed studies on the most promising alternatives.

3.2 Pure Hematite: Bulk and Surfaces

3.2.1. Bulk calculations

In hematite, the Fe^{3+} cations are six- coordinated and occupy two thirds of the octahedral sites of the slightly distorted hexagonal close- packed oxygen array in a repeating pattern of Fe-O-Fe along the c axis. (see **Chapter 1**). The experimentally determined unit-cell parameters used as a starting point for this work were those reported by Cox et al¹ with dimensions $a = b = 5.04 \text{ \AA}$ and $c = 13.75 \text{ \AA}$, $\alpha = 90^\circ$, $\beta = 90^\circ$, $\gamma = 120^\circ$. On geometry optimisation, using constant pressure energy minimization, these cell dimensions became $a = b 5.06 \text{ \AA}$ and $c = 13.36 \text{ \AA}$. The calculated interatomic distances of Fe-O in pure Fe_2O_3 are 1.944 \AA and 2.096 \AA which are in agreement with the experimental bond lengths² of 1.96 and 2.08 \AA respectively.

The potentials used within this work are shown in **Table 3. 1** which have been compared to different oxygen potentials used in other models³. The potential parameters chosen for this study, Type 3, $(-2.21, 0.21, 27.29)$ ⁴ predicted the crystal cell parameters satisfactorily and provided the best match when compared to the experimental results.

Different Oxygen Potentials ³ used	Shell Charge	Core Charge	Spring
Type 1	-2.86	0.86	74.72
Type 2	-2.86	0.86	27.29
Type 3	-2.21	0.21	27.29

Table 3. 1: Different oxygen potentials considered. Type 3 is used in this study, since it is found to give the best fit with the experimental results.

The results obtained have been compared using two different computer simulation codes, METADISE⁵ and GULP⁶ (**Table 3. 2**).

Properties	Metadise	Gulp	Experimental
Lattice Energy (eV)	-150.37	-150.36	-149.05 ⁷
Elastic Constant ($\rho/g\text{ cm}^{-3}$)	5.12 (C_{11})	5.11	5.24
Static Dielectric Constant	ϵ_{11} : 8.008 ϵ_{22} : 8.008 ϵ_{33} : 12.05	ϵ_{11} : 7.997 ϵ_{22} : 7.998 ϵ_{33} : 12.03	ϵ_{ijk} 12
Lattice vectors (\AA)	10.13 10.13 13.36	10.13 10.13 13.365	10.08 10.08 13.75

Table 3. 2: Comparison of the mechanical properties obtained in a 2x2x1 supercell using the computer codes METADISE and GULP with reference to experimental calculations¹.

3.2.2 Surface Calculations

Understanding the surface reactions of iron oxides is critical for a variety of applications including catalysis,^{8, 9} corrosion¹⁰ and metal-oxide thin film preparations¹¹. There are two stages involved in the calculation of surfaces, the creation of the surface from the bulk and the calculation of its structure and properties. The lower index surfaces have been considered here are (0001), (01 $\bar{1}2$), (10 $\bar{1}2$), (10 $\bar{1}1$), (10 $\bar{1}0 = 01\bar{1}0$), (11 $\bar{2}0$), (11 $\bar{2}1$), and (01 $\bar{1}1$). For each surface except for there are two terminations possible, usually an iron and oxygen surface. From the calculated surface energies, the (01 $\bar{1}2$) oxygen-terminated surface is energetically more stable than the other surfaces considered (**Table 3.3**). The order of stability is:

(01 $\bar{1}2$)Ox > (10 $\bar{1}0 = 01\bar{1}0$)Ox > (0001)Fe > (11 $\bar{2}1$) > (01 $\bar{1}2$)Fe > (10 $\bar{1}2$)Fe > (10 $\bar{1}1$)Ox > (01 $\bar{1}1$) > (10 $\bar{1}1$)Fe > (10 $\bar{1}2$)Ox > (11 $\bar{2}0$)Fe > (0001)Ox > (10 $\bar{1}0 = 01\bar{1}0$)Fe.

Miller Indices	Iron Termination Fe (III) (Jm ⁻²)	Oxygen Termination Surface (Jm ⁻²)
0001	2.41	3.86
01 $\bar{1}2$	2.84	2.11
11 $\bar{2}1$	2.87	2.87
10 $\bar{1}2$	2.96	3.24
01 $\bar{1}1$	3.01	—
10 $\bar{1}1$	3.13	2.98
11 $\bar{2}0$	3.27	2.45
10 $\bar{1}0 = 01\bar{1}0$	3.92	2.35

Table 3.3: Calculated surface energies of the surfaces. The figures in red indicate the most stable surfaces.

A detailed discussion of the individual surfaces follows:

(0001) Surface

The Fe-terminated (0001) surface is the natural cleavage plane of hematite and has been studied extensively by a number of researchers.¹²⁻¹⁸ This is one of the stable planes of hematite, **Figure 3.1**. The Fe-terminated surface is non-polar, flat and has a lower energy than the oxygen-terminated surface (**Table 3.3**). Only one Fe is at the surface and it is equally bonded to three neighboring oxygen atoms. The Fe-O bond distance is 1.77Å, shorter than the normal bond length in the bulk (1.96Å). In the bulk, the Fe-O bond distances vary from 1.882Å to 2.096Å, where anions are in four to six-fold coordination. The inter-layer spacing on this surface is compared with experiment¹⁹ and displayed in **Figure 3.2**.

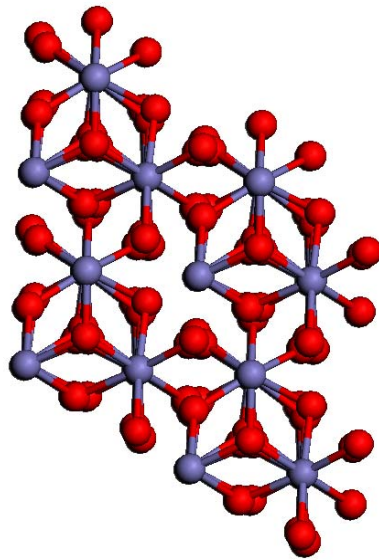


Figure 3.1: Top view of Fe-terminated surface (0001)

Bergmayer²⁰ and Rohrbach²¹ predicted the presence of ferryl terminations (Fe=O) on the (0001) Fe-terminated surface using ab-initio calculations and later Lemire et al²² supported this argument experimentally, using scanning tunneling microscopy and infrared reflection absorption spectroscopy. However, although we cannot model single or double bonds with these simulations, the study in this thesis showed that the Fe-O bond distances at the surface decrease significantly from 1.96/2.09 Å to 1.73 Å (the Fe=O bond length is 1.65 Å²³) adding weight to this argument.

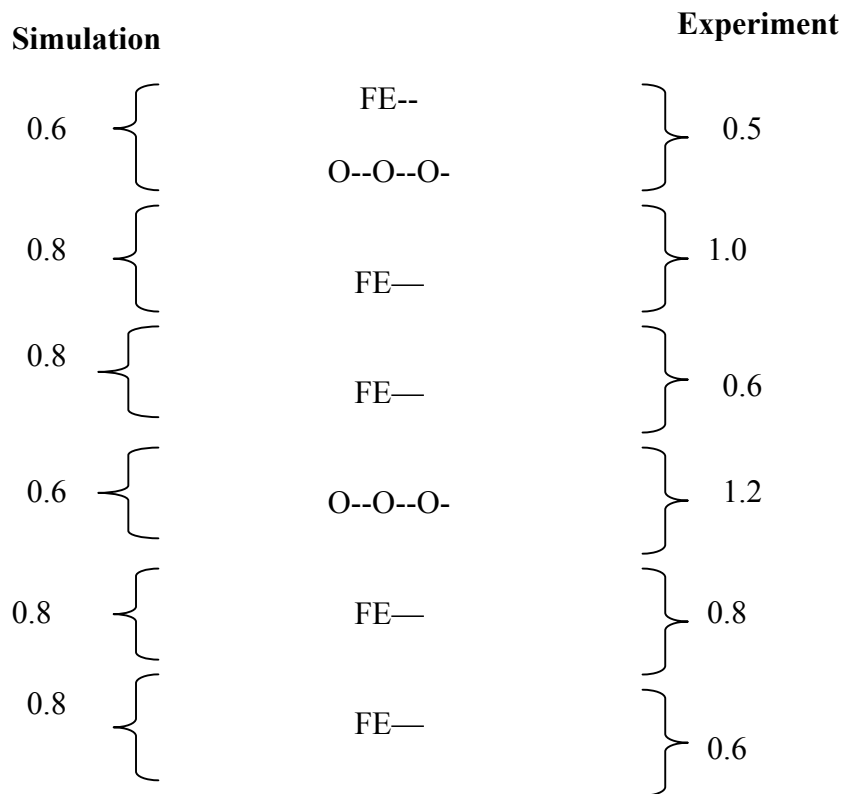


Figure 3.2: Comparison of calculated and experimental¹⁹ interlayer spacing (Å) on the Fe terminated (0001) surface.

The oxygen-terminated surface is dipolar and modeling of the surface is made possible by a rearrangement (discussed in **Chapter 2**), where half of the oxygen ions are moved to the bottom of the unit cell.²⁴ The surface anions are two-coordinated and are highly reactive. The cations in the second layer show coordination from three to five.

(01 $\bar{1}$ 2) Surface

For the Fe-terminated surface, the Fe atoms on the surface show four- and five-fold coordination (**Figure 3.3**). Henderson et al²⁵ and Wang et al²⁶ discussed the presence of ferrous ions on these surfaces. According to the authors, the presence of four- and fivefold-coordinated Fe sites influences the distribution of the ferrous ions on the surface. In this work, the oxidation state of iron is +3. Hence, the presence of lower coordinated Fe ions cannot indicate the presence of ferrous ions on these surfaces, but the coordination found would be compatible with their presence.

The oxygen surface has a stable, well ordered structure (**Figure 3.3**). In the surface layer, cations are either five- or six-coordinated, while anions are three- or four-coordinated. The high-fold coordination is thought to contribute to the stability of the surface. In the bulk layers, both ions are fully coordinated.

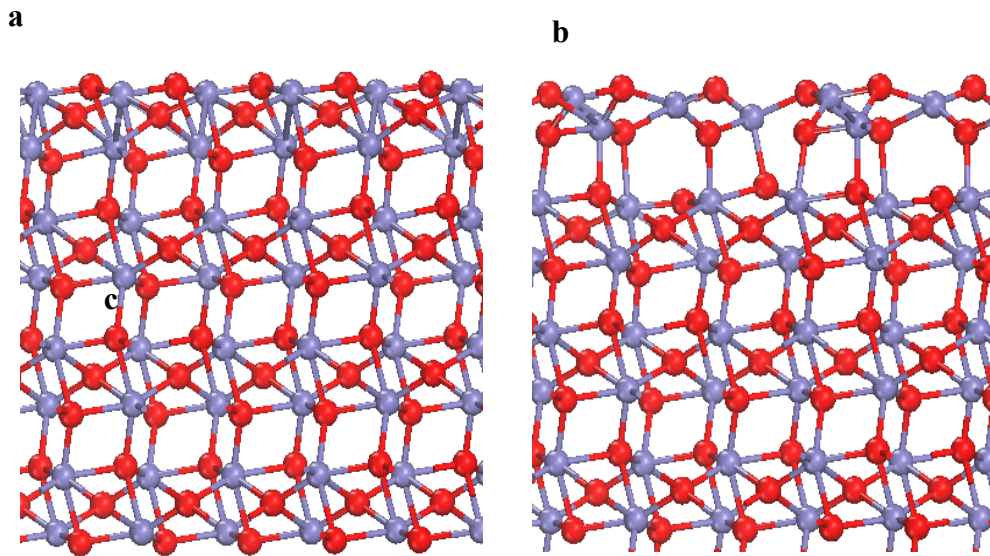


Figure 3.3: a) Oxygen terminated $(01\bar{1}2)$ surface. b) Fe terminated surface.

$(11\bar{2}1)$ Surface

Both Fe- and O-terminations have the same surface energy, indicating the similarity of these surfaces. The stacking sequence of the Fe-terminated surface is shown in **Figure 3.4**. In the Fe-terminated surface, there is only one Fe ion on the surface showing four-fold coordination. The distance between the cations on the surface and sub surface layers is closer compared to the bulk. Oxygen ions are two-three- and four - coordinated.

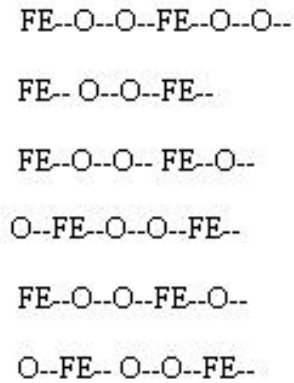


Figure 3.4: Stacking sequence of Fe-terminated surface.

The oxygen-terminated surface is not planar and Fe-O bond stretching (2.27\AA) causes an irregular surface, which is shown in **Figure 3.5**.

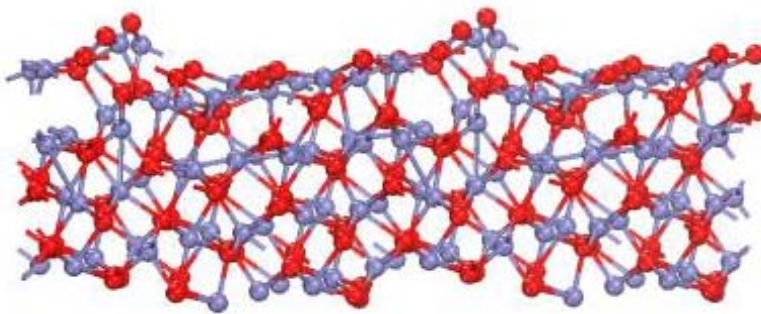


Figure 3.5: The oxygen terminated $(11\bar{2}1)$ surfaces.

$(10\bar{1}2)$ Surface

The stacking sequence of the Fe-terminated and oxygen-terminated surfaces are shown in **Figure 3.6**. On the Fe-terminated surface, the two Fe ions are in the same layer, showing three-fold coordination. The Fe-O bond distance is shorter at the surface (1.75\AA , 1.79\AA and 1.81\AA) in agreement with DFT studies (1.83\AA) by Lo *et al.*²⁷ In the immediate subsurface layer, the Fe ions are four-coordinated and bond

distances are 1.91 Å (3) and 1.83 Å. The oxygen ions are two- and three-coordinated in this subsurface layer.

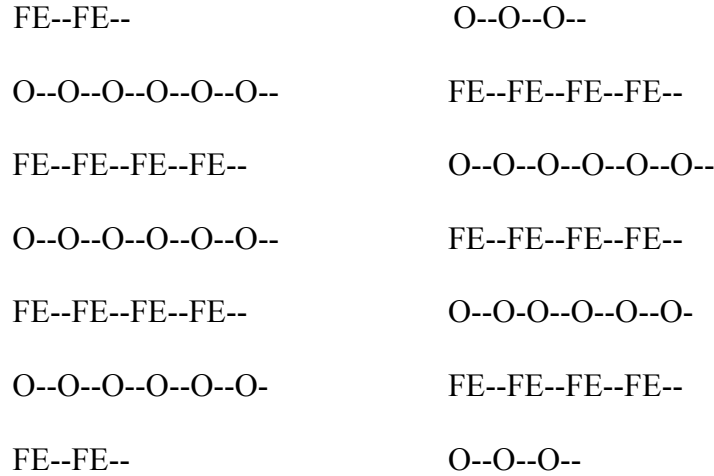


Figure 3.6: a) The stacking sequences of Fe and O terminated surfaces of $(10\bar{1}2)$

At the oxygen-terminated surface, the cations are 2.79 Å apart, and the Fe-O bond length varies from 1.78-2.05 Å.

$(01\bar{1}1)$ Surface

There is only one possible termination with one Fe on this surface, which is in three-fold coordination (**Figure 3.7**). The surface is irregular with one Fe^{3+} and O^{2-} shifted slightly upward. (**Figure 3.8**). Like the other surfaces, the cations are closer in the surface compared to the bulk. The Fe-O bond lengths vary from 1.72 Å - 2.26 Å, which causes the irregular shape of the surface. After relaxation, the bond distance varies from 1.776 Å to 2.12 Å and significant movement occurs in the second layer. Here the Fe-O bond distances increase, resulting in the exposure of lower-coordinated Fe ions on the surface (**Figure 3.8**), which may attract impurities such as water.

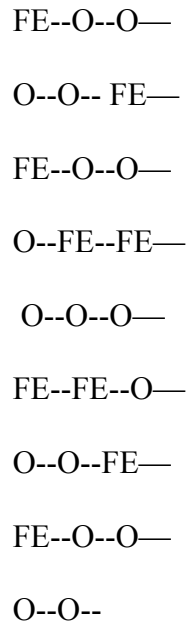


Figure 3.7: Stacking sequence of $(01\bar{1}1)$ surfaces.

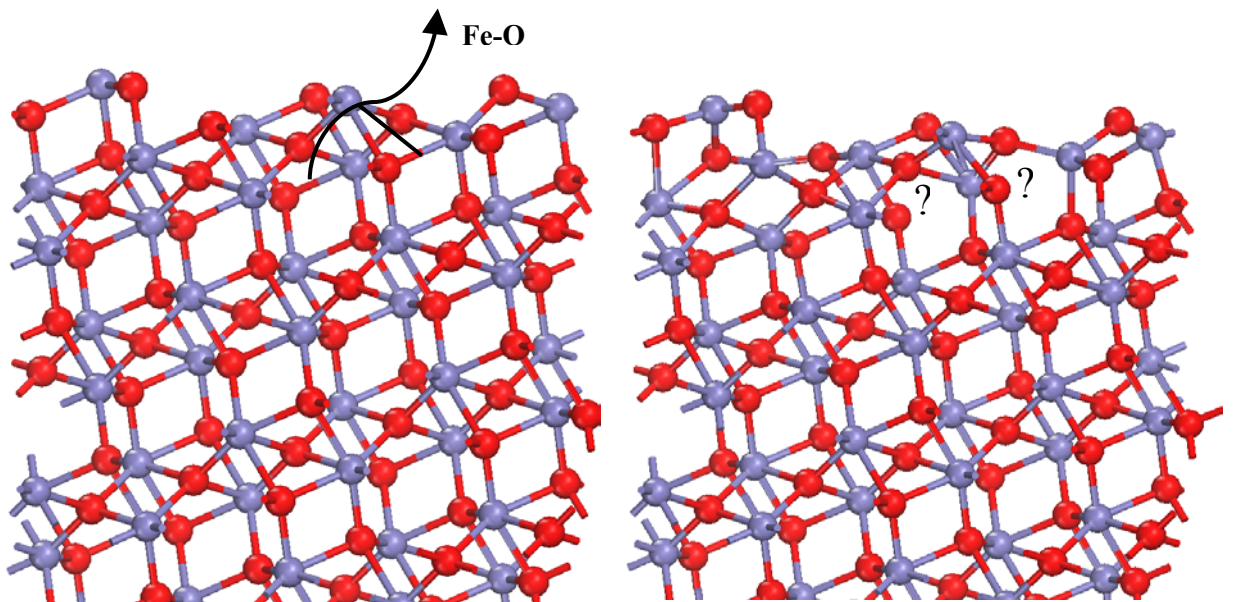


Figure 3.8: $(01\bar{1}1)$ surface before and after relaxation. Rearrangement occurs resulting in the accumulation of lower - coordinated Fe on the surface layer.

$(10\bar{1}1)$ Surface

The Fe-terminated surface is irregular and consists of only one Fe atom on the surface in four-fold coordination, whereas they are three- to six-coordinated in the bulk. The possible stacking sequences of the Fe-terminated surfaces are shown in **Figure 3.9**. The oxygen atoms are two- three- and four-coordinated. The Fe-Fe and Fe-O bond distances in the bulk are smaller than on the surface, and the spread of bond distances (**Figure 3.10**) results in an irregular shape to compensate the surface strain. A rearrangement occurs on the Fe-terminated surface after relaxation. The Fe-O bond distance increases resulting in the conversion of three-coordinated oxygen positions to two-coordinated oxygens, which are directed slightly upwards in relation to the other surface atoms (**Figure 3.11**). The Fe-O bond lengths decrease from 2.096 Å and 1.944 Å to 1.816 Å and 1.781 Å respectively. The low-coordinated oxygen ion on the surface could be reactive towards impurities, such as cations or protons, or catalytic reactants.

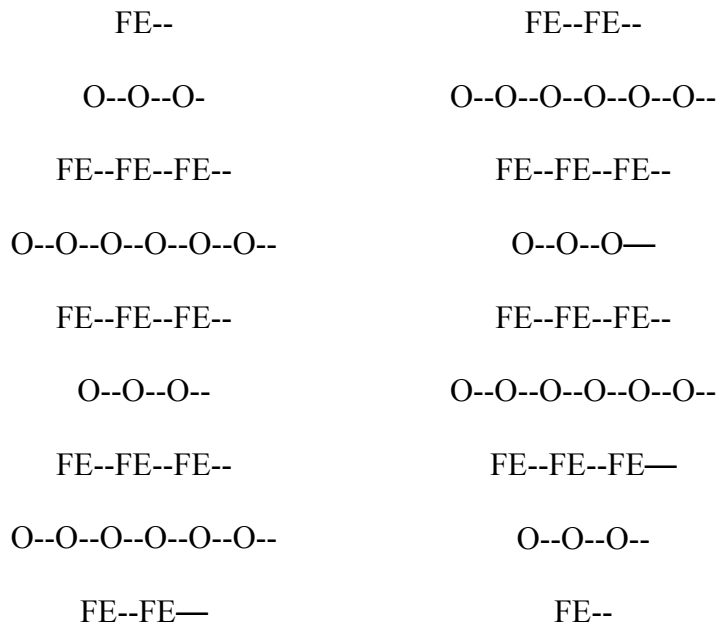


Figure 3.9: The possible stacking sequences of the $(10\bar{1}1)$ Fe terminated surface.

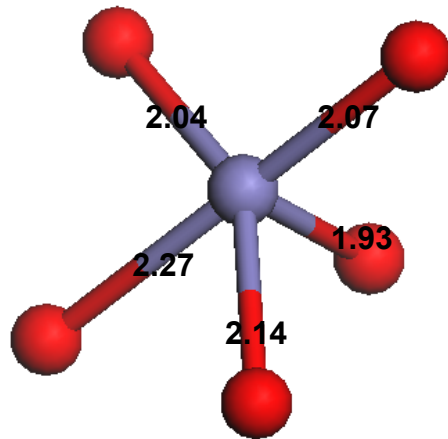


Figure 3.10: The different Fe-O bond distances (Å) observed in the Fe-terminated $(10\bar{1}1)$ surface compared to the bulk value. (Fe-O - 1.945/2.096 Å)

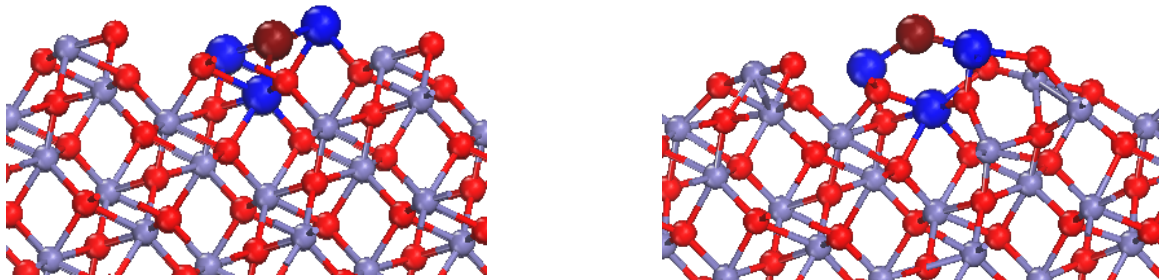


Figure 3.11: Fe terminated $(10\bar{1}1)$ surface before and after relaxation. The dark red ball is the three coordinated oxygen bonded to three bright blue Fe ions and after relaxation, it becomes two coordinated.

There is only a small difference between the Fe-terminated and oxygen-terminated surfaces. The oxygen-terminated surface has a pyramidal shape. The stacking sequence of the stable oxygen-terminated surface is shown in **Figure 3.12**. There are six oxygen ions on the surface, three of which are positioned slightly upwards. Here the cations show four-fold coordination, while the anions are two- to four-coordinated. In the second layer, the Fe-O bond length increases to 2.25 Å resulting in a gap between the layers.

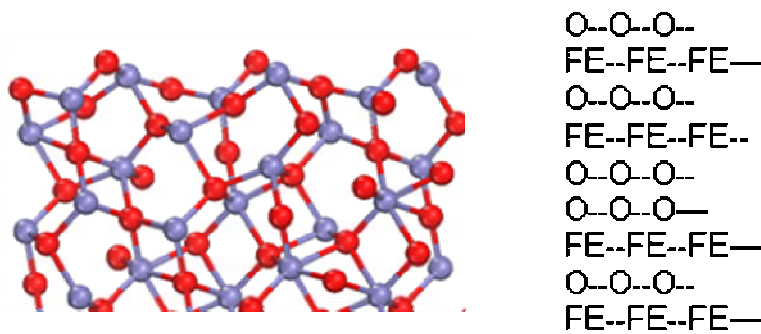


Figure 3.12: Oxygen-terminated ($10\bar{1}1$) surface and the stacking sequence.

($11\bar{2}0$) Surface

There are two possible terminations for this surface. The Fe-terminated surface has six Fe ions on the surface and it has an irregular shape. The surface layer cations exhibit four-fold coordination, while in the layer below the Fe ions are five- and six-coordinated. The distance between the surface cations and anions is smaller than in the bulk.

The oxygen-terminated surface is one of the stable surfaces of hematite. The surface has a very well ordered structure (**Figure 3.13**) with six oxygen atoms on the surface layer in two- and three-fold coordination.

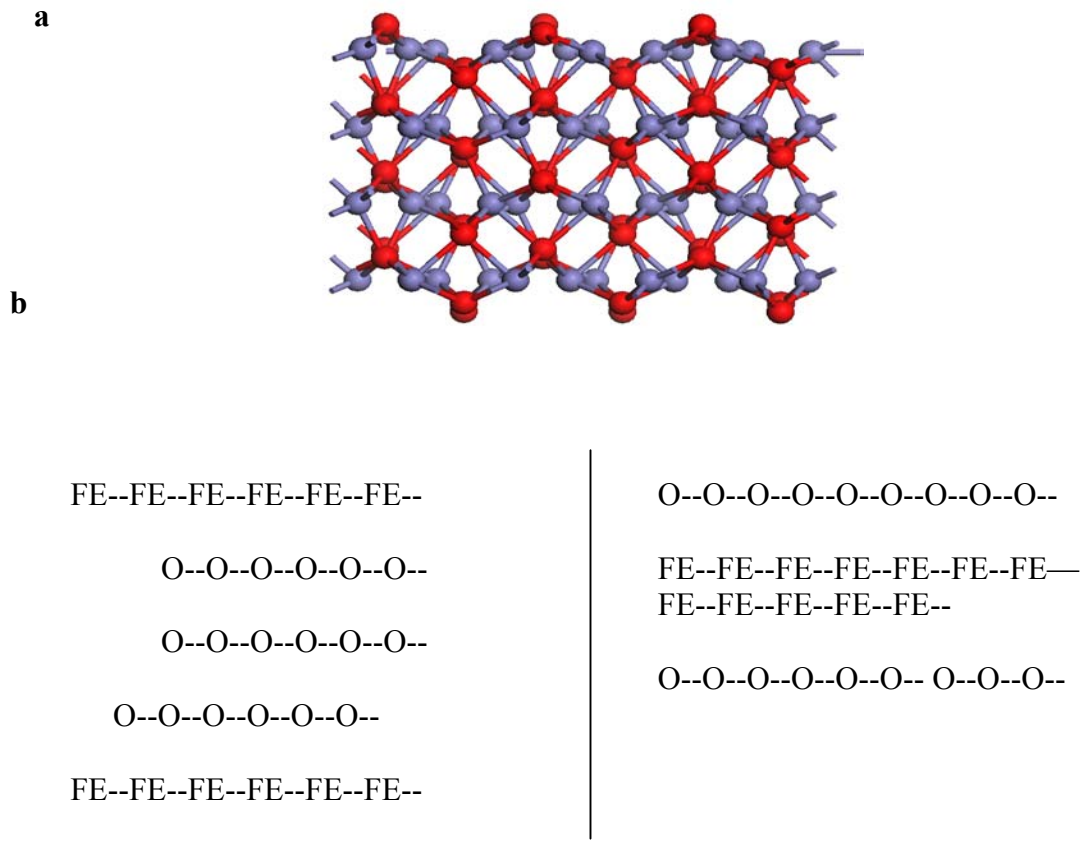


Figure 3.13: a) $(11\bar{2}0)$ oxygen terminated surface b) Stacking sequence of the possible terminations of both Fe- and O-terminated surfaces.

$(10\bar{1}0)$ Surface

On the optimized Fe-terminated surface, the cations are closer compared to the other surfaces (2.66\AA). The distance between the cations increases in the bulk. In the first layer, Fe ions are initially in three- and four- fold coordination, which will make them more active than the five- and six- coordinated cations. After relaxation, one of the four-coordinated surface Fe ions becomes three- coordinated and moves towards the surface leaving a void (**Figure 3.14**). The Fe-O bond length increases to 2.25\AA , giving an unstable irregular shape compared to the bulk.

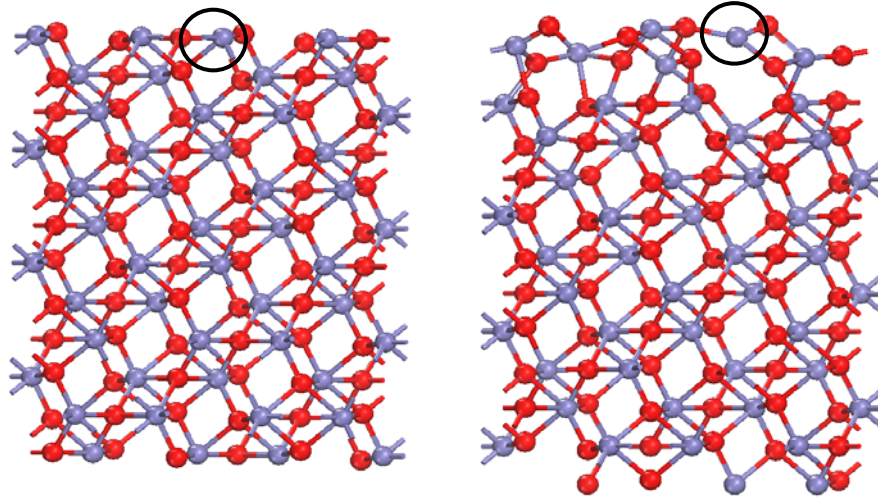


Figure 3.14: $(10\bar{1}0)$ Fe terminated surface. a) Structure before relaxation, b) after relaxation Fe (circled) becomes three coordinated.

On the oxygen-terminated surface, the surface oxygens are in two-fold coordination, with the Fe ions next to the surface layer in four and five - fold coordination. The cations are far apart compared to other surfaces and the four surface oxygen ions are positioned slightly above the surface plane.

3.3 Defects

3.3.1 Dissociated Water

We first investigate adsorption of a dissociated water molecule to the (0001) , $(01\bar{1}2)$, $(11\bar{2}1)$ and $(01\bar{1}1)$ surfaces, as described in Chapter 2. The interaction between the dissociated water and the surface is through bonding of an OH group to surface Fe ions and the proton to surface oxygen ions (**Figure 3.15**), where hydrogen-bonding between surface species also occurs. There is a strong interaction between water and the hematite surfaces. The differences in surface energies between the dry and hydroxylated surfaces indicate which surfaces are stabilised by the reaction with water (**Table 3. 4**).

Miller Indices	Pure Iron Surface Fe (III) (Jm^{-2})	Hydroxylated iron surface (Jm^{-2})	Pure Oxygen Surface (Jm^{-2})	Hydroxylated Oxygen Surface (Jm^{-2})
0001	2.41	1.37	3.86	0.47
01 $\bar{1}$ 2	2.84	2.69	2.11	1.84
11 $\bar{2}$ 1	2.87	2.37	2.87	2.28
01 $\bar{1}$ 1	3.01	1.21	—	—

Table 3. 4: Surface energies of pure and hydroxylated surfaces.

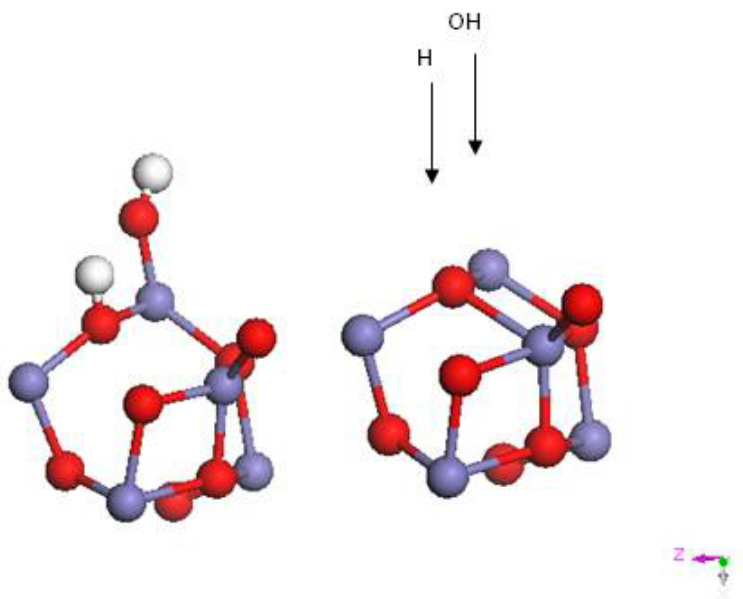


Figure 3.15: Dissociated water on the surface.

The adsorption energies of water molecules were calculated by comparing the energy of the surface with the adsorbed water molecule and the sum of the energies of pure surface and the ‘self-energy’ for dissociated water obtained from an energy cycle, as explained in Chapter 2.

$$E_{\text{ads}} = E_{\text{s+water}} - E_{\text{s}} + E_{\text{water}} \quad (3.1)$$

where E_{ads} is the adsorption energy, $E_{\text{s+water}}$ is the energy of the surface with an adsorbed water molecule and E_{water} is the ‘self energy’ of the dissociated water molecule (-7.1 eV).

The adsorption energies are displayed in **Table 3.5**

Surface	Adsorption energy, eV
(001) Fe	-1.4
O	-3.2
(01 $\bar{1}$ 2) Fe	-0.8
O	-1.3
(11 $\bar{2}$ 1) Fe	-3.7
O	-4.4
(01 $\bar{1}$ 1)	-3.2

Table 3.5: Adsorption energies of one molecule of dissociated water.

(0001) Surface

Both (0001) surface terminations favour hydroxylation. Rustad et al^{28, 29} using molecular dynamics simulation methods investigated the effect of iron oxides in aqueous solutions. The authors argued that the large surface relaxation energy is due to the presence of four-fold Fe ions on the hydroxylated surface layer.

The hydroxylated oxygen-terminated surface is much more stable than Fe-terminated surface, which implies the occurrence of the oxygen-terminated surface under aqueous environment. This result is also verified by recent DFT studies conducted by Trainor *et al*³⁰. However, Chambers *et al*³¹ using a molecular beam epitaxial study, only found Fe-terminated surfaces under highly oxidizing conditions if the crystal were cleaved under ultra-high vacuum conditions. Eggleston *et al*³² using scanning tunneling microscopy and resonant tunneling calculations have identified that under aqueous conditions both Fe- and O-terminated surfaces co-exist. As the dehydrated Fe-terminated surface is more stable than the O-terminated surface, upon hydroxylation both surface terminations can be expected due to the exothermic adsorption of water.

(01 $\bar{1}$ 2) Surface

Hydroxylation takes place by the explicit dissociation of water. On the Fe-terminated surface, adsorption of the hydroxide ions occurs at Fe sites over the oxygen valleys and protonation of the ridge of oxygen, where the Fe-OH bond distance is found to be 1.7 Å. Wasserman *et al*³³ in their study of hydroxylated surfaces suggested the formation of non-uniform hydroxylated surfaces. The current research verifies the work carried out by the above authors. When the surface is hydroxylated, a significant rearrangement of ions takes place in the top Fe layer. The Fe atoms become six-coordinated resulting in the formation of a monolayer of water on the surface. Wang *et al*²⁶ confirmed the presence of six-fold Fe ions, which favour the movement of Fe ions to the surface sites, resulting in increased stability. Kerisit *et al*³⁴ using classical molecular dynamics simulations showed that water absorbs weakly to the fivefold-coordinated Fe cation sites. However, in the present study, pre-dissociated molecules of water are used to consider the surface interactions. Henderson *et al*²⁵ stated that the hydroxylated (01 $\bar{1}$ 2) surface is more stable than the wet oxygen-terminated (0001) surface, but the surface energy results (**Table 3. 4**) from this study do not support this argument, although we have only considered here the adsorption of a single water molecule per simulation cell.

The hydroxylated oxygen surface is more stable than the dry surface. The surface stability increases with the number of molecules of water dissociated onto the surface, as the surface ions have a higher coordination number after hydroxylation. Kerisit and Rosso^{35, 36} proposed that the stability of the hydroxylated surface is due to an electron hopping mechanism between neighbouring Fe cations. However, in this classical potential model, the description of electron mobility is not included. Tanwar *et al*^{37, 38} investigated these surfaces by X-ray diffraction and crystal truncation rod (CTR) diffraction studies. These studies revealed the presence of different functional groups for example Fe-O, Fe-OH etc on these surfaces. Furthermore, the authors stated that these surfaces show an affinity towards the adsorption of ferrous ions (Fe^{2+}) which converts to Fe^{3+} in an oxidation reaction.

$(11\bar{2}1)$ Surface

The only difference between the hydroxylated surface terminations is the positioning of hydroxyl groups. On the Fe-terminated surface, the OH ions after relaxation are closer to each other due to an electrostatic force of attraction experienced on these surfaces, which binds them near to the surface, as can be seen in **Figure 3.16**. The bond distance changes considerably after relaxation. The Fe-OH bond distances before relaxation are 2.01 Å and 1.92 Å which shorten to 1.71 Å and 1.899 Å respectively after relaxation.

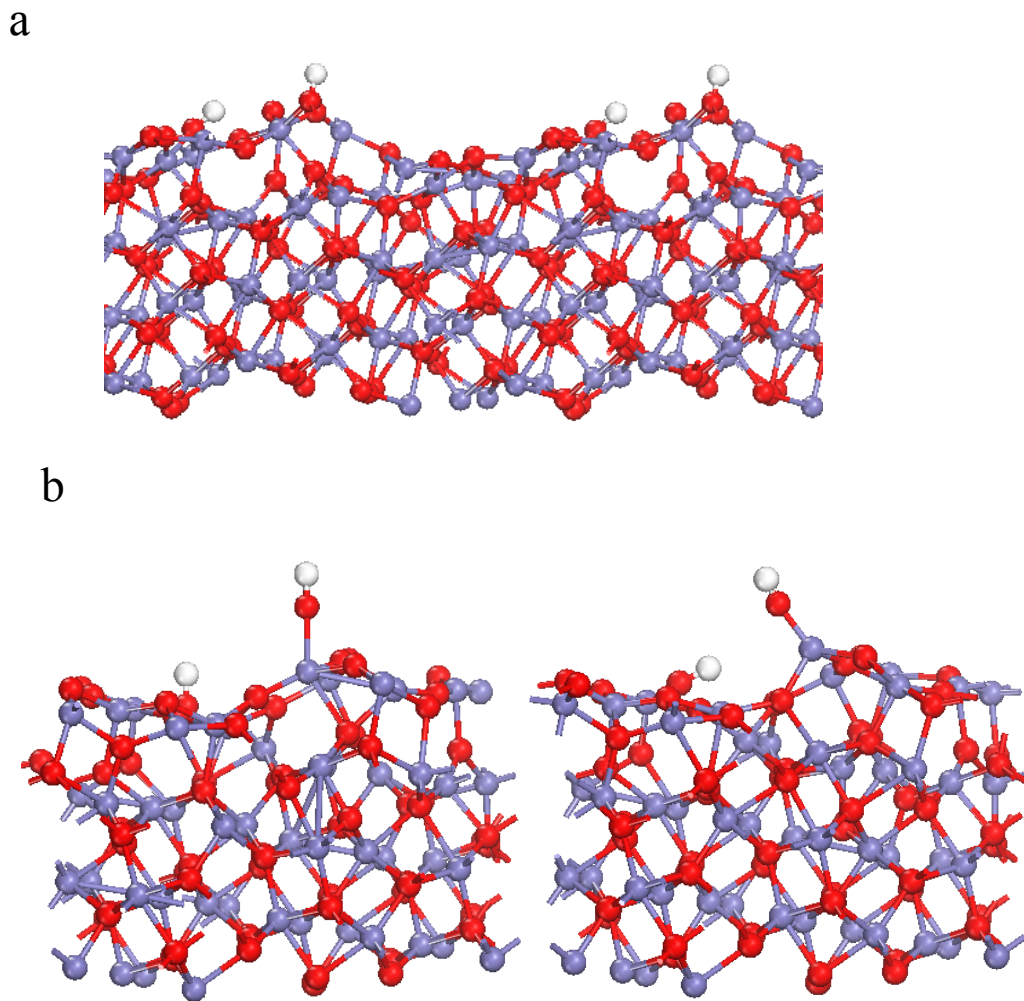


Figure 3.16: $(11\bar{2}1)$ surfaces a) hydroxylated oxygen-terminated surface and b) hydroxylated iron-terminated surface before and after relaxation.

On the oxygen-terminated surface, the enrichment of oxygen ions on the surface causes an electrostatic repulsion, which moves the OH ions more than 2 Å apart.

(01 $\bar{1}1$) Surface

In the (01 $\bar{1}1$) hydroxylated surface, the oxygen ions in the bulk are three- and four-coordinated whereas in the surface layer the oxygen ions have two-fold coordination and are reactive towards protonation. The hydroxylated surface is considerably more stable than the pure surface.

In the next section, the doping of a range of trivalent metal ions at the (0001) surface of hematite has been investigated.

3.3.2 The Role of Cation Dopants in Hematite: Al³⁺, Sc³⁺, Ti³⁺, V³⁺, Cr³⁺, Mn³⁺, Y³⁺ and La³⁺.

In order to investigate the behaviour of Cr³⁺ and potential alternatives in hematite, defect calculations have been carried out with a range of isovalent cations in the bulk and at the surfaces.

Bulk Calculations

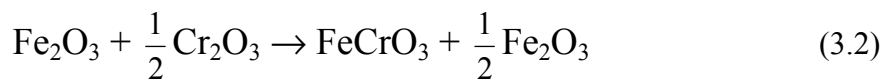
A single cation substitution was made in the 2 x 2 x 1 supercell containing 48 cation sites, followed by lattice energy minimization at constant pressure³⁹. The defect energy is calculated from the difference between the lattice energies of the perfect and the defective supercell. The results obtained are compared with the defect formation energy obtained from the Mott–Littleton method. A number of isovalent cations with varying ionic radii (

Table 3. 6), Al³⁺, Sc³⁺, Ti³⁺, V³⁺, Mn³⁺, Y³⁺ and La³⁺ are considered along side Cr³⁺.

Dopants	Ionic radii (Å)
Al ³⁺	0.535
Mn ³⁺	0.58
Cr ³⁺	0.615
V ³⁺	0.64
Fe ³⁺	0.645
Ti ³⁺	0.67
Sc ³⁺	0.745
Y ³⁺	0.90
La ³⁺	1.032

Table 3. 6: The dopants considered and their radii⁴⁰ for octahedral coordination.

To calculate the energetics of ionic substitution, it is necessary to calculate the solution energy from the Born-Haber cycle incorporating all the steps in the substitution⁴¹. In this calculation, it is assumed that the dopant ion, M³⁺ is introduced into the lattice of Fe₂O₃ from M₂O₃ where the dopant cation replaces the Fe³⁺ ion, which then combines with the anion to form FeMO₃. The solution energy is the total energy involved in this process, and it gives an indication of the ease of substitution of the dopant ion into the lattice. An example of the calculation of the solution energy for Cr³⁺ is shown below:



Here Fe^{3+} is replaced by a Cr^{3+} ion. The solution energy can be calculated as follows,

$$E_{\text{Solution}} = \left[E_{\text{Cr}(\text{def})} + \frac{1}{2} E_{\text{Fe}_2\text{O}_3} \right] - \frac{1}{2} E_{\text{Cr}_2\text{O}_3} \quad (3.3)$$

where $E_{\text{Cr}(\text{def})}$ is the defect energy, which is the difference in energy between the doped and perfect lattice and $E_{\text{Fe}_2\text{O}_3}$ and $E_{\text{Cr}_2\text{O}_3}$ are the respective lattice energies.

Using Mott-Littleton approach, the solution energy is calculated as,

$$E_s = \frac{1}{2} E_{\alpha\text{-Fe}_2\text{O}_3} + E_{\text{M}^{3+}} - \frac{1}{2} E_{\text{M}_2\text{O}_3} \quad (3.4)$$

where, $E_{\text{M}^{3+}}$ is the defect energy of the dopant, $\text{M} = \text{Al}^{3+}/\text{Sc}^{3+}/\text{Ti}^{3+}/\text{V}^{3+}/\text{Mn}^{3+}/\text{Y}^{3+}/\text{La}^{3+}$.

In the case of supercell calculations, the defect energy is the energy difference between the two $2 \times 2 \times 1$ cells, $E_{\text{Fe}_{47}\text{CrO}_{72}}$ and $E_{\text{Fe}_{48}\text{O}_{72}}$.

The defect energy is tabulated in (**Table 3. 7**) For the ions that are smaller than or a similar size to Fe^{3+} , i.e. Al^{3+} , Cr^{3+} , Mn^{3+} , Ti^{3+} and V^{3+} , the doped structure is more stable than or at least as stable as pure hematite, where Al^{3+} -doped hematite is the most stable system (-4.63eV) observed. This could be due to the smaller ionic size of Al^{3+} compared to other dopants, making it easy to incorporate into the lattice of hematite. For the larger ions: Sc^{3+} , Y^{3+} and La^{3+} , the defect energy is calculated as a positive value, suggesting that the doped structures are not energetically favoured. However, V^{3+} has low positive defect energy, so even though it has a very similar ionic radius as Fe^{3+} , the doped system is not favoured.

Dopant ions(3+)	Defect energy (eV)
Al	-4.63
Mn	-0.46
Cr	-1.94
V	0.054
Ti	-0.29
Sc	3.01
Y	8.72
La	14.72

Table 3. 7: Defect energy of each dopant is calculated

The results of the solution energy calculations for both the dilute Mott-Littleton and more concentrated supercell calculations are shown in **Table 3. 8**.

Dopants (M^{3+})	Solution Energy (eV)		$ \Delta r $ (Å)
	Supercell	Mott-Littleton	
Al	0.48	0.4	0.11
Cr	0.12	0.12	0.03
Mn	0.11	-0.01	0.065
Ti	0.11	0.01	0.025
V	0.12	0.02	0.005
Sc	0.24	0.26	0.10
Y	1.12	1.13	0.255
La	2.74	2.91	0.387

Table 3. 8: The solution energies are calculated using Mott-Littleton method and supercell calculations. $|\Delta r|$ is the absolute value of the difference in ionic radii between Fe^{3+} (0.645 Å) and the dopant.

The data in **Table 3. 8** show good agreement between the Mott-Littleton and supercell calculations. The solution energy from both calculations (Mott-Littleton and Supercell) is similar, as all the ions are isovalent. The difference will be more pronounced for aliovalent ions (ie, with different oxidation states) as the charged defects will interact over a longer range in the supercell calculations. The solution energy increases with difference in the size of the dopant⁴² compared to Fe^{3+} . For Mn^{3+} , Cr^{3+} , V^{3+} and Ti^{3+} , it is less than 0.2 eV as their ionic radii is more or less the same as Fe^{3+} , and for the bigger dopants such as La^{3+} and Y^{3+} , it is in the range of 1 to 3 eV, whereas the solution energy for the much smaller aluminium ion is large at > 0.4 eV. To conclude, for those ions whose radii are closest to that of Fe^{3+} in particular Mn^{3+} , Cr^{3+} , V^{3+} and Ti^{3+} , the solution energies are low indicating favorable solubility into the bulk of Fe_2O_3 (**Figure 3.17**). As the difference in ionic radii between the dopant and Fe^{3+} increases, so does the solution energy. Thus, Al^{3+} and Sc^{3+} are less soluble in bulk Fe_2O_3 than Cr^{3+} , Mn^{3+} , V^{3+} or Ti^{3+} whereas Y^{3+} and La^{3+} will be insoluble, based on their very large solution energies.

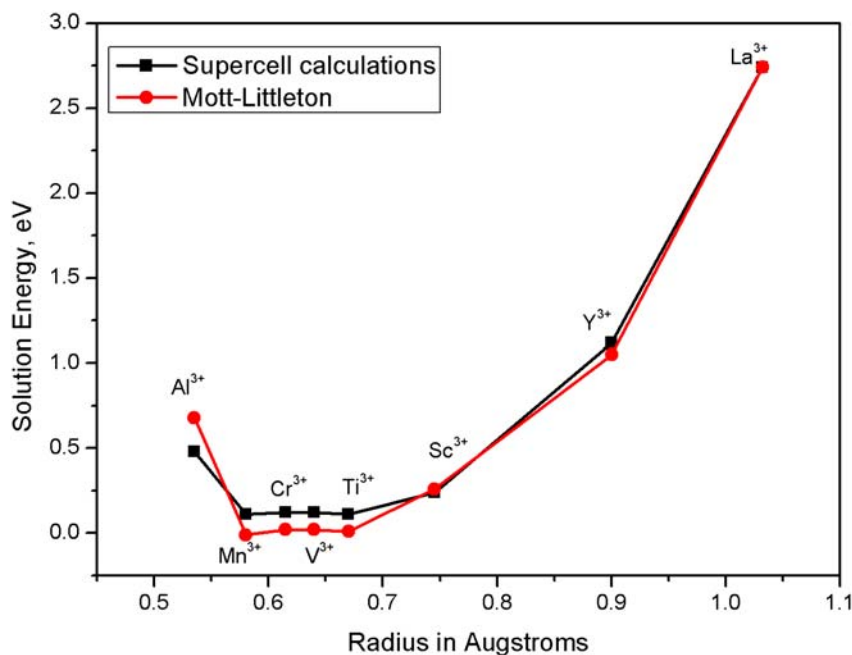


Figure 3.17: The solution energies of the dopants calculated using Mott-Littleton method and supercell calculations plotted against ionic radius.

Surface calculations

Segregation of impurity ions to or from the surface is important in surface chemistry and in particular for catalytic reactions. The (001) Fe-terminated surface, which is one of the stable planes, is used to analyse the nature and position of the dopants at the surface. Of the surfaces considered here, the oxygen-terminated (012) surface is the most stable plane of hematite. However, in this study, where we are mainly interested in cation dopants and their stability and segregation to the surface, the most stable Fe-terminated surface, the (001) is considered. In the unit cell, there is only one Fe^{3+} ion on the surface in three-fold coordination, while the six-fold sites are below the surface. As in the calculations discussed previously (**Section 3.2.2**), the surface is created by employing the two-region strategy, (discussed in detail in Chapter 2) with a finite thickness. The top region (1) has a thickness of 20 Å with 48 Fe^{3+} cations and the bottom region (2) extends down to a total of more than 150 Å (**Figure 3.18**). The dopant is placed on the surface, ie, the top layer of region (1), and then systematically moved towards the bottom of region (1), which represents the interior or bulk site. Energy minimization calculations have been performed for each dopant position and the total lattice energy, solution energy and segregation energy were calculated and compared.

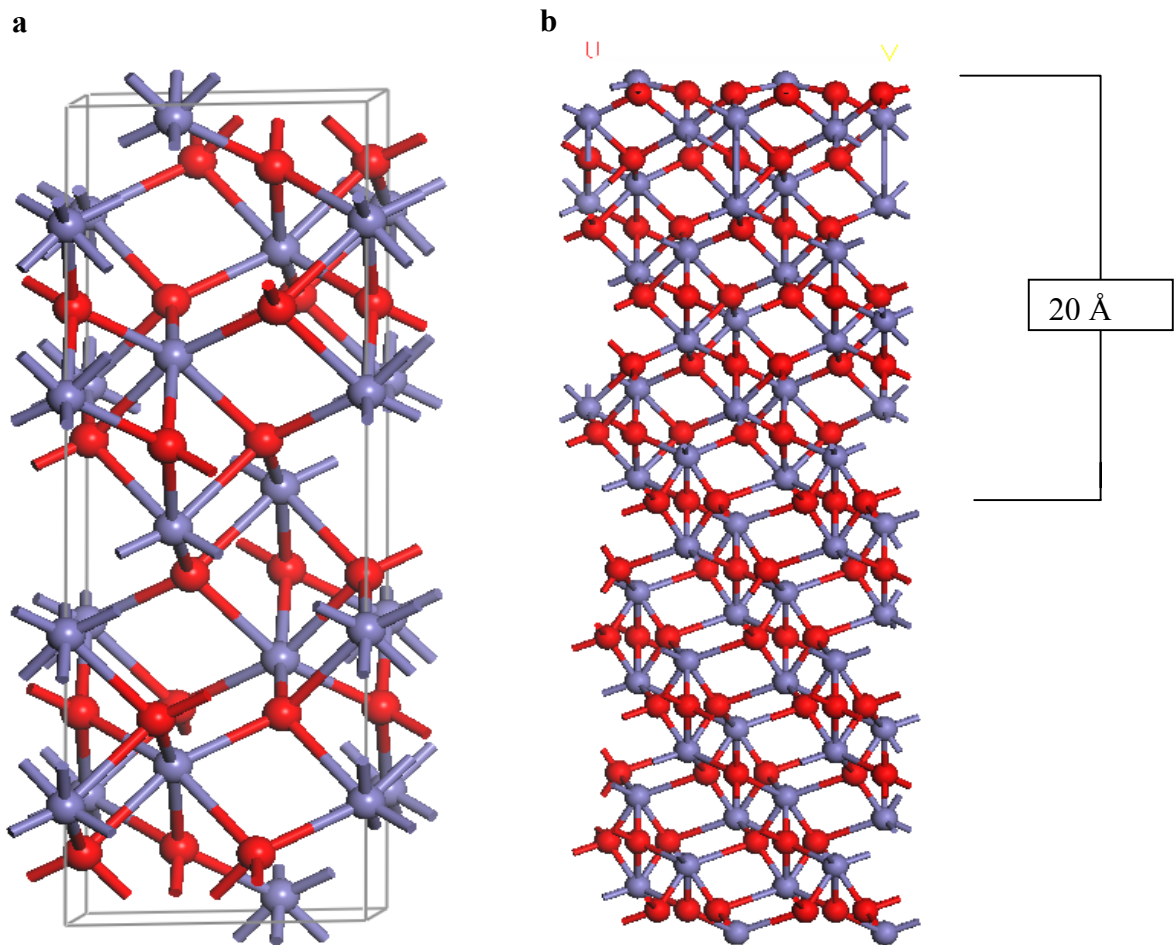


Figure 3.18: Hematite: a) Bulk structure and b) Fe terminated (0001) surface with a thickness of 20 Å.

The segregation energy, E_{seg} is the energy difference between placing an impurity on the surface with that of placing the same impurity in the bulk and is given by,

$$E_{\text{seg}} = E_{\text{def}}(\text{surf}) - E_{\text{def}}(\text{bulk}) \quad (3.5)$$

The relative size of the impurity ion has an effect on the segregation energy, with a negative value representing segregation to the surface. The results examined here show a tendency of subsurface segregation.⁴³

There is a second useful term known as the trap energy⁴⁴, E_T , which can be defined as the difference in energy between a dopant in the surface and the most stable position in the subsurface layers, given by

$$E_T = E_s^{\text{SUBSURF}} - E_s^{\text{SURF}} \quad (3.6)$$

where the E_s terms are the respective solution energies for the trap minimum and the surface.

A negative trap energy indicates that the dopant would segregate to a region in the subsurface layer. This energy trap is seen by Stanek *et al*^{45, 46}, for example, in their studies of Y^{3+} segregation in ZrO_2 . For relatively bigger ions, for example, Sc^{3+} , which do not have entirely stable positions in the bulk, the trap energy is considerably lower than its segregation energy, which means it will not segregate to the surface but is weakly trapped just below the surface (**Table 3.9**). This trap is not evident for dopants with similar ionic radii.

Dopants(M^{3+})	Radius(\AA)	Surface Solution Energy (eV)	Segregation Energy (eV)	Trap Energy (eV)	Barrier Energy (eV)
Al	0.535	0.12	-0.36	-0.1	0.18
Mn	0.58	0.38	0.27	–	–
Cr	0.615	0.95	0.83	–	–
V	0.64	0.99	0.87	–	–
Ti	0.67	0.93	0.82	–	–
Sc	0.745	0.32	0.08	-0.1	0.5
Y	0.9	0.53	-0.59	–	1.1
La	1.032	0.84	-1.9	–	–

Table 3.9: Calculated segregation, solution and trap energy.

The above definitions of segregation and trap energies relate to simple cases depicted in **Figure 3.19**.

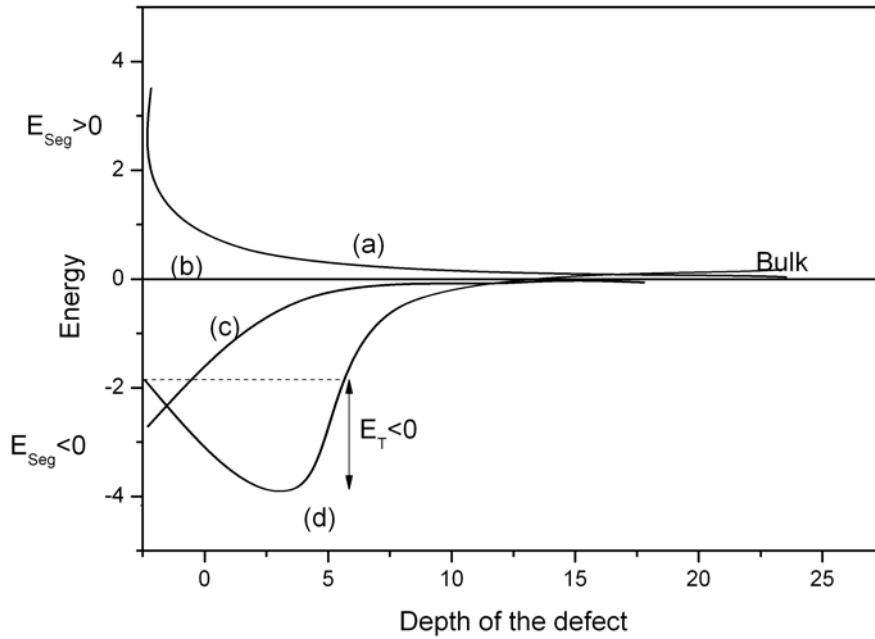


Figure 3.19: Definitions of segregation and trap energy to the bulk (a) segregation away from the surface (b) homogenous solution (c) segregation to the surface (d) enrichment of subsurface region.

Surface, solution, segregation and trap energies derived from the data in **Table 3.9** are plotted in Figures 3.21 to 3.28. Figures 3.22 to 3.28 show the computational results for the variation of energy (normalised to the bulk) plotted as a function of depth from the surface for each of the eight dopants under consideration in this section. The data taken from **Table 3.9** on the variation of segregation energy with dopants radius are shown in **Figure 3.20**. In addition **Table 3.10** list the variation in dopant cation-anion bond distances at the surface and in the subsurface and bulk.

M-O (Bond distance, Å)	Surface layer	Subsurface layer	Bulk Layers
Al-O Fe _{surf} -O: 1.763 1.77	1.653	1.911 1.948	1.824 2.028
Cr-O Fe _{surf} -O: 1.767	1.784	1.945 2.052	1.947 2.063
Mn-O Fe _{surf} -O: 1.767	1.776	2.015 2.022	1.949 2.095
Ti-O Fe _{surf} -O: 1.765 1.77	1.882	1.92 2.046	1.976 2.102
V-O Fe _{surf} -O: 1.765	1.835	1.930 2.055	1.985 2.110
Sc-O Fe _{surf} -O: 1.765	1.859	1.951 2.113	2.008 2.155
Y-O Fe _{surf} -O: 1.760 1.777	2.003	2.060 2.302	2.109 2.276

Table 3. 10: The bond distance between the dopant ion (Al³⁺, Cr³⁺, Mn³⁺, Ti³⁺, V³⁺, Sc³⁺ and Y³⁺) and O²⁻ ion in the surface, subsurface and bulk layers.

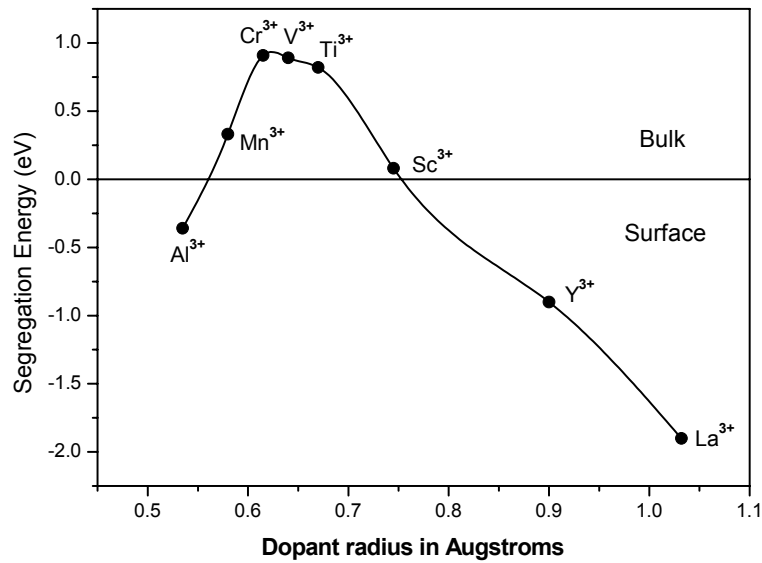


Figure 3.20: Calculated segregation energy is plotted against the radii of the dopants.

The actual computational results of the variation of energy as a function of dopant depth in Figures.3.22 to 3.28 in several cases deviate considerably from the idealised plots in **Figure 3.19**. However, a number of important conclusions can be drawn from the data. It can be observed that the segregation energy varies significantly as the size of the dopant ion differs from Fe^{3+} . Bigger ions such as La^{3+} and Y^{3+} have a large driving force for segregation to the surface, while Mn^{3+} , V^{3+} , Cr^{3+} , and Ti^{3+} , which are similar in size to Fe^{3+} , segregate to the bulk. Al^{3+} and Sc^{3+} which differ in size from Fe^{3+} to the same extent but in opposite direction, show similar subsurface segregational properties and trap energies. These results suggest that there is a close relationship between the ionic size and the segregation energy.

We now continue discussion of the dopant behaviour in groups based on the similarities within each group.

1. $\text{Cr}^{3+} / \text{Mn}^{3+} / \text{V}^{3+} / \text{Ti}^{3+}$
2. $\text{Al}^{3+} / \text{Sc}^{3+} / \text{Y}^{3+}$
3. La^{3+}

1. $\text{Cr}^{3+} / \text{Mn}^{3+} / \text{V}^{3+} / \text{Ti}^{3+}$

a) Cr^{3+} doping

There is no driving force for the segregation to surface (**Figure 3.21**) as the segregation energy is positive, due to the similar radii of Fe^{3+} and Cr^{3+} which can incorporate Cr^{3+} into the bulk lattice of hematite without causing strain as proposed by McLean *et al*⁴⁷. As the Cr-O bond is shorter than Fe-O, Cr is closely coordinated to oxygen. On the surface the cations are only three co-ordinated which may be the reason why Cr^{3+} prefers to stay in the bulk.

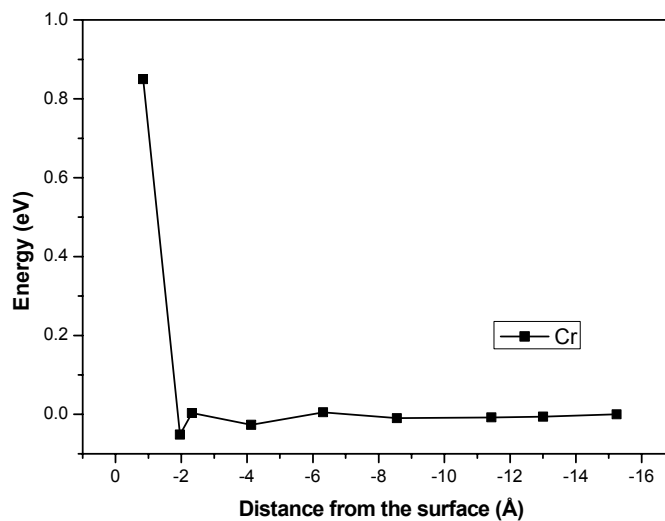


Figure 3.21: Segregation energy of Cr as a function of defect depth.

From the results, it can be observed that the energy is at a minimum in the subsurface where the Cr-O distance is small. From the third layer onwards the total energy remains the same and is equal to the bulk energy.

b) Mn^{3+} doping

The ionic radius of Mn^{3+} is slightly smaller than Fe^{3+} and the segregation energy is small. The most stable position of the dopant is in the bulk, similar to Cr^{3+} and it follows a similar pattern in the depth profile (**Figure 3.22**). The energy profile shows a sharp fall in energy when the dopant moves away from the surface.

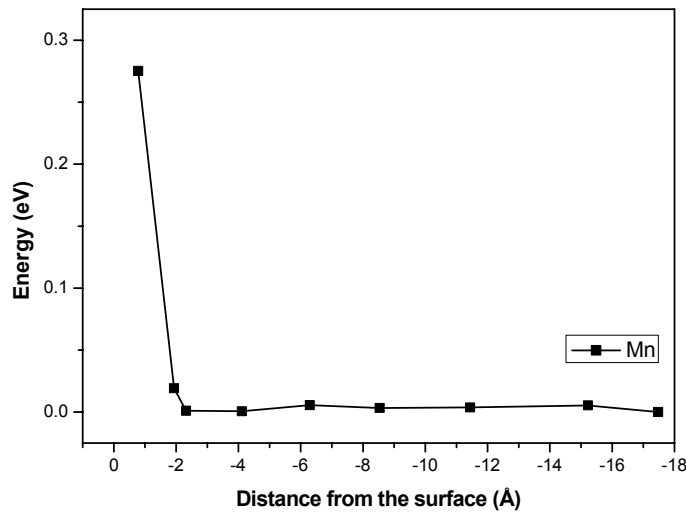


Figure 3.22: Total lattice energy as a function of dopant depth.

c) V^{3+} doping

When Fe^{3+} is replaced by V^{3+} , the distance between the cations increases, (the Fe-Fe distance is 2.845 Å and Fe-V is 2.863 Å). On the surface the V-O distance is 1.835 Å whereas the Fe-O distance is 1.77 Å. The curve of the energy with depth (**Figure 3.23**) is less abrupt than for Cr^{3+} or Mn^{3+} , although the energy difference between the first and second layers is still large. There is no tendency for subsurface trapping, which has also moved to the third layer. As the dopant moves away from the surface to the inner layers, the distance between V and O is 2.014/1.984 Å and Fe and V is 3.013 Å. As the cations are further apart, the interactions are weaker and it stabilises the bulk.

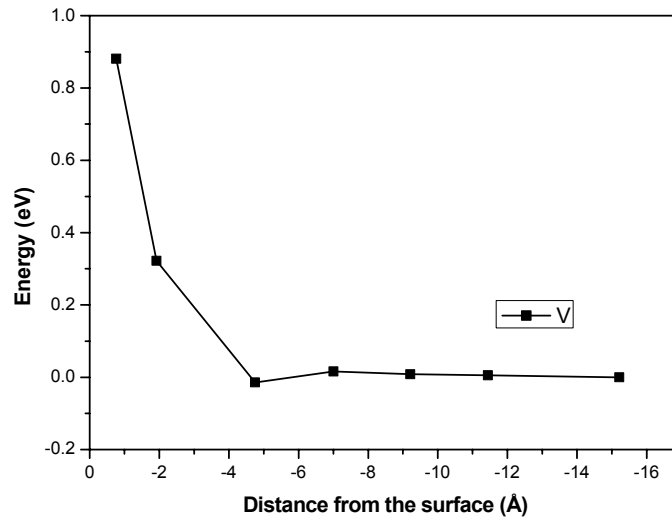


Figure 3.23: Segregation energy versus the distance of the dopant from the surface

d) Ti^{3+} doping

The energy profile (**Figure 3.24**) of Ti^{3+} is very similar to V^{3+} . At the surface, the Ti^{3+} ion is three coordinated and the distance between Ti^{3+} and O is 1.82\AA . In the subsurface layers the Ti- O distance is 1.92 and 2.05\AA and Fe-O is very similar at 1.93 and 2.15\AA . The minimum is observed in the third layer, where the distance between the cations (Fe and Ti) is closer (2.84\AA), and the repulsive force is high enough to separate Fe^{3+} cations from each other along the direction perpendicular to the surface which results in an increase in the inter planar spacing.

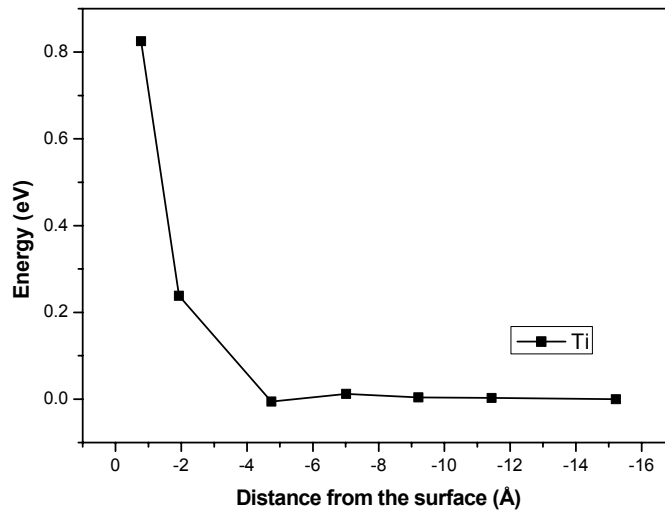


Figure 3.24: Calculated segregation energy of Ti^{3+} as a function of depth.

It has been reported^{48, 49} based on their physical properties that in FeTiO_3 , the Ti cations appear to be Ti^{4+} but Ti^{3+} is also present to some degree. This possibility of electron transfer between cations can cause complications including cation ordering and chemical impurities. More recently Brown *et al*⁵⁰ conducted a calorimetric study, which revealed that in FeTiO_3 solutions, Fe is in the +2 oxidation state, verifying that electron transfer occurs between Fe^{2+} - Ti^{4+} pairs. However, the study of these effects is beyond the limit of atomistic simulation methods.

The above dopants, Cr^{3+} , Mn^{3+} , V^{3+} and Ti^{3+} have similar solution energies and are soluble in hematite. The segregation energies also show that these dopants prefer to be in the bulk and not at the surface indicating that they may not play a direct role in catalytic processes, although they may still have a part in controlling particle size.

2. $Al^{3+}/Sc^{3+}/Y^{3+}$

a) Al^{3+} doping

Aluminium shows a different energy profile from Cr^{3+} (**Figure 3.25**). The smaller size of the ion, compared to Fe^{3+} , and the possibility of shortening the Al^{3+} -O distance at the surface (1.653 Å) results in a negative segregation energy. (In $\alpha-Al_2O_3$, the Al^{3+} -O distance is 1.87/1.992 Å). The surface cations are three-coordinated and on the surface, the distance between Fe^{3+} and Al^{3+} is 3.059/5.066 Å. The surface minimum can be explained by the electrostatic interactions between the ions due to the large Fe^{3+} - Al^{3+} distance on the subsurface layers and the short Al^{3+} -O distance on the surface.

It has been reported that Al_2O_3 exists as a separate phase in the hematite bulk with a high thermal stability and that the catalytic activity increases with temperature⁵¹. The segregation energy (-0.36 eV) evidences a considerable driving force for the segregation of Al^{3+} to the surface of hematite. Although Al^{3+} has the lowest energy at the surface, the energy increases sharply when it moves to the second layer and exhibits a trap or energy minimum in the subsurface layers. This result suggests that Al^{3+} does not segregate to the surface, but segregates to the subsurface layers. However, the energy barrier is not very high (0.2eV), so it can be proposed that when the temperature is increased, this barrier can be overcome and more Al from the subsurface layer may move to the surface resulting in an Al-rich surface.

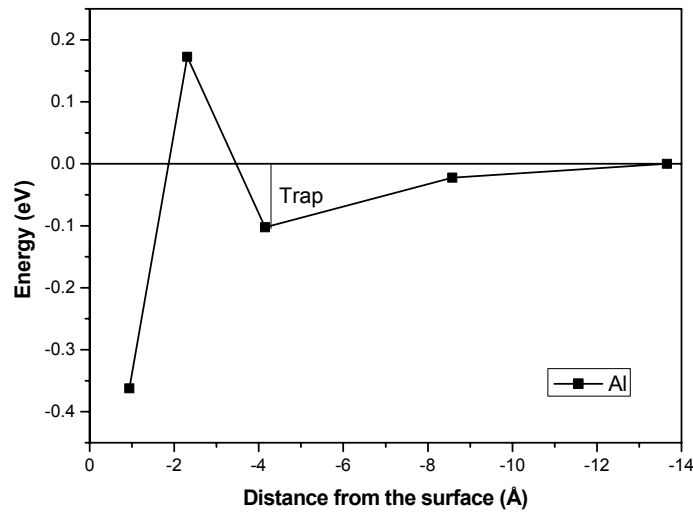


Figure 3.25: Segregation energy of Al^{3+} as a function of depth from the surface.

Experimental data (XPS and XRD) obtained in collaboration on this project also suggests the segregation of Al^{3+} to hematite surfaces. These experimental results are explained in detail in Chapter 7.

b) Sc^{3+} doping

Sc^{3+} is different from the other dopants, in that the size of the ionic radius is slightly larger than Fe^{3+} , and according to the trend, it should segregate to the surface. However, from examining the energy profile (**Figure 3.26**), the most stable site is in the bulk. A small minimum can be found in the third layer, where the dopant is most stable. As the segregation energy is positive overall (**Table 3.9**), the Sc^{3+} should show a tendency for subsurface segregation in Sc^{3+} -doped systems.

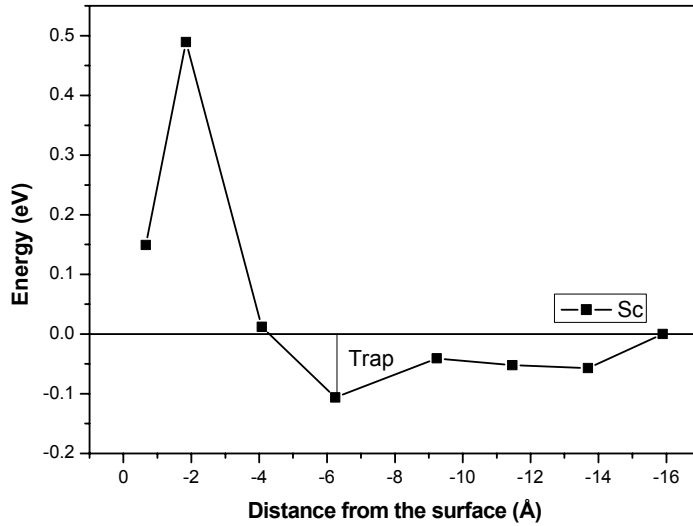


Figure 3.26: Segregation energy plotted against defect depth.

c) Y^{3+} doping

As the size of the dopant cation increases, it tends to remain at the surface where there is more space. Y^{3+} segregates to the surface, as the ionic radius of this cation is bigger than Fe^{3+} , which is shown by the negative segregation energy. From the energy profile, the dopants will segregate to the surface, but an energy barrier of 1 eV is observed in the depth profile (**Figure 3.27**).

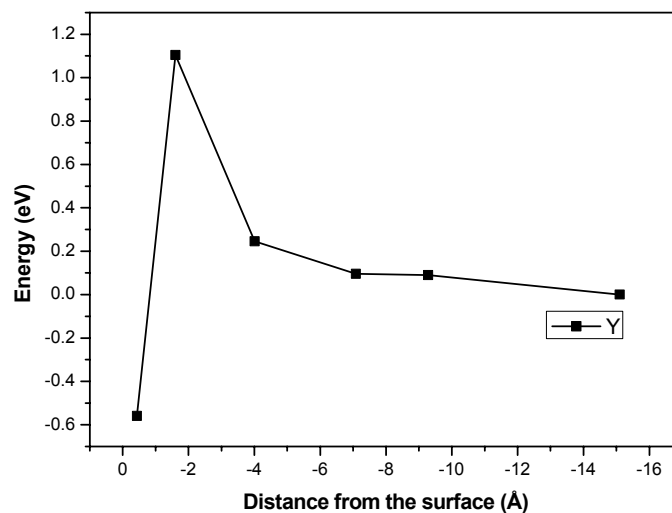


Figure 3.27: Calculated segregation energies of Y^{3+} doping plotted as a function of defect depth.

Al^{3+} , Sc^{3+} and Y^{3+} thus segregate to the surface although there is an energy barrier (subsurface) to cation movement. Al^{3+} has the lowest solution energy and is most likely to dissolve in the surface, which might be controlling the particle size in the reaction. Practically, the large energy barriers for Y^{3+} segregation may lead to the formation of a separate Y_2O_3 layer.

3. La^{3+} doping

La^{3+} is the largest cation considered in this study and has the largest, negative segregation energy (**Figure 3.28**), which agrees with reports⁴² that these dopants will not stay in solution but will form a second phase. Zhang *et al*⁵² proposed an agglomeration in La-Fe solutions which increases the surface area which can be explained by the segregation of La to hematite surfaces, where it is likely to form La_2O_3 .

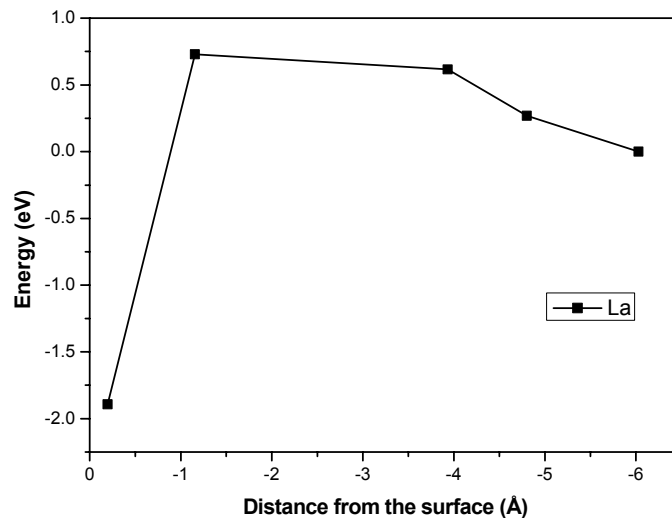


Figure 3.28: Segregation energy of La^{3+} as a function of defect depth.

Comparison of Solution Energies: Bulk and Surfaces

As discussed earlier in section 3.3.1, the dopants Cr^{3+} , Mn^{3+} , Ti^{3+} and V^{3+} (**Figure 3.20**) can form stable solutions in bulk hematite whereas the solution energy diagram in **Figure 3.29** shows the segregation of Al^{3+} to the surface, while Y^{3+} and La^{3+} form separate phases of their corresponding oxides.

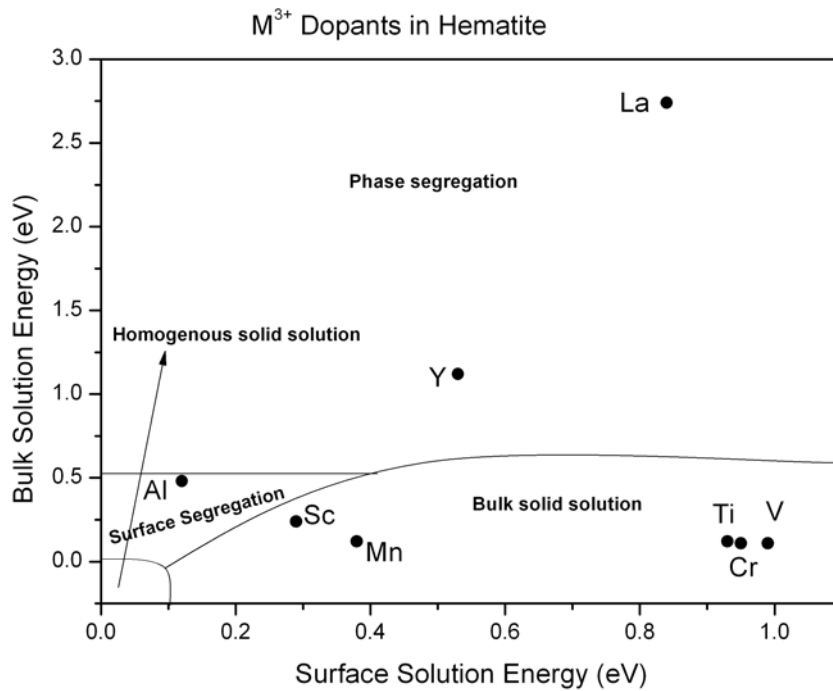


Figure 3.29: The solubility curve displaying the presence of dopants on the surface and bulk.

3.3.3 The Effect of Cr^{3+} and dissociated water on the Surface Morphology of Hematite

To find out the impact of defects on the hematite crystals, the equilibrium crystal morphologies are calculated from the surface energies (**Figure 3.30**). Using the INSIGHT II program, the crystal morphologies are built from the calculated surface energies (**Table 3.3**).

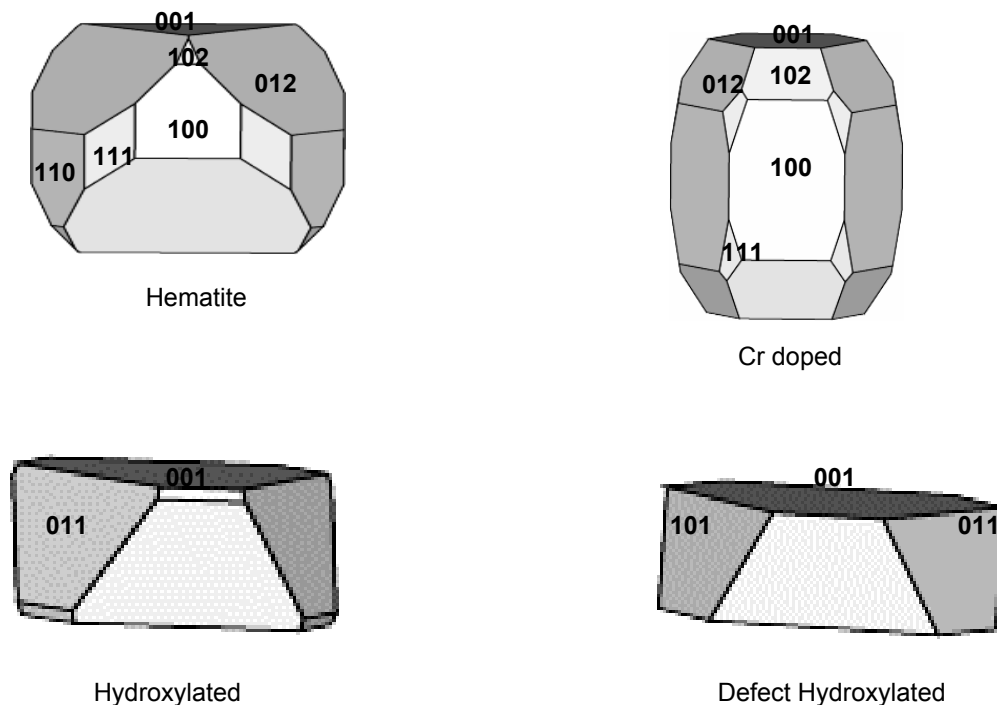


Figure 3.30: The crystal morphologies of different surfaces in hematite.

The most stable faces of hematite are found to be $(012 = 01\bar{1}2)$, $(001 = 0001)$, $(100 = 10\bar{1}0)$, $(110 = 11\bar{2}0)$, $(111 = 11\bar{2}1)$ and $(102 = 10\bar{1}2)$. However, when doped with chromium, the relative surface energies of the (0001) and $(10\bar{1}0)$ faces decrease (as can be seen from **Figure 3.30** and the $(01\bar{1}2)$, $(11\bar{2}1)$ faces increase and the $(11\bar{2}0)$ face becomes less stable. In an aqueous environment, the (0001) and

(01 $\bar{1}1$) are the stable faces while for Cr doped hydroxylated hematite, the stable faces are the (0001), (01 $\bar{1}1$) and (10 $\bar{1}1$).

3.4. Conclusions

In this chapter, the characteristics of the bulk and different surface planes of hematite have been investigated. From the surface calculations, it can be observed that the (01 $\bar{1}2$) oxygen-terminated surface is the most stable face and the (0001) oxygen-terminated surface becomes more stable in an aqueous environment. The surface studies showed that the addition of impurities to the surface, affects their stability but it does not change the morphology to a great extent. The location and impact of Cr³⁺ in the bulk and different low-index dry and hydrated surfaces of hematite has been investigated. There is no driving force for segregation of Cr³⁺ to any of these surfaces. The defect morphology suggests that the presence of Cr³⁺ stabilises the (0001), (10 $\bar{1}1$) and (10 $\bar{1}0$) surface planes. The effect of water on the surface has been investigated which increases the stability of the surfaces.

The substitution of an isovalent cation (Al³⁺, Mn³⁺, Ti³⁺, V³⁺, Sc³⁺, Y³⁺ and La³⁺) at an iron site has been modeled and the energetics of the reaction, such as segregation energy and solution energy are calculated. The solution energies from both the calculations (Mott-Littleton and Supercell) are similar for all these isovalent ions. For the bulk calculations with Al³⁺, Cr³⁺, Mn³⁺ and Ti³⁺, the doped structure is more stable than pure hematite, where Al³⁺ doping is energetically favourable compared to the other dopants considered. V³⁺ as a dopant, shows a small positive defect energy as it has a very similar ionic radii as Fe³⁺, although the doped system is not favoured. For Sc³⁺, Y³⁺ and La³⁺, the defect energy is calculated as a positive value, which suggests that the doped structures are not energetically favoured. The relative size of the impurity has an effect on the solution energy and the segregation energy. The ions with similar radii as Fe³⁺ such as Cr³⁺, Mn³⁺, V³⁺ and Ti³⁺ possess similar solution energies and they form solid solutions in the bulk of hematite, whereas Al³⁺

is soluble in the surface. The bigger ions, Y^{3+} and La^{3+} would be expected to form separate oxide layers.

From the segregation energy calculations, Mn^{3+} follows a similar depth profile as Cr^{3+} . Al^{3+} and Ti^{3+} follow similar ordering properties, which are in good agreement with the experimental results⁵³. The bigger ions such as La^{3+} and Y^{3+} segregate to the surface, whilst the ions with similar radii as Fe^{3+} prefer to stay in the bulk. The relative size of the impurity ion will affect the segregation. The larger the defect the higher the tendency to migrate to the surface as the segregation is driven by release of strain obtained by incorporating large ions at the surface rather than in the bulk. Sc^{3+} and Al^{3+} exhibit a subsurface segregation, which is an important phenomenon from a catalytic point of view.

Finally by comparing all these energies, Al^{3+} , Mn^{3+} and Ti^{3+} could be suitable alternatives for Cr^{3+} . However, Ti^{3+} is not considered due to its anticipated electron transfer with Fe^{3+} and a tendency to remain in the Ti^{4+} oxidation state. As Al^{3+} is harmless and the behaviour of Mn^{3+} is similar to Cr^{3+} , these two dopants have been chosen for further study.

In the next chapter, mixed solid solutions are investigated. The structural behaviour, stability and properties of $(Fe_{1-x}Cr_x)_2O_3$ solutions are considered and compared with the properties of $(Fe_{1-x}Al_x)_2O_3$ solid solutions.

3.5. References

- 1 J. COX, *The Journal of Physics and Chemistry of solids* 1962, **24**, 405.
- 2 G. A. Waychunas, *Reviews in Mineralogy and Geochemistry*, 1991, **25**, 509.
- 3 G.V. Lewis and C. R. A. Catlow, *Journal of Physics, C; Solid state Physics*, 1985, **18**, 1149-1161.
- 4 S. C. Parker, *Physics and Chemistry of Minerals*, 2004, **31**, 507-517.
- 5 G W Watson, E Toby Kelsey, Nora H de Leeuw, Duncan J Harris and S. C. Parker, *Journal of the Chemical Society, Faraday Transactions*, 1996, **92**, 433-438.
- 6 J.D.Gale, *Journal of the Chemical Society, Faraday Transactions*, 1997, **101**, 1248.
- 7 D. R. Lide, *CRC Handbook of Chemistry and Physics*, CRC Press, 1999.
- 8 N. Apostolescu, B. Geiger, K. Hizbullah, M. T. Jan, S. Kureti, D. Reichert, F. Schott and W. Weisweiler, *Applied Catalysis B: Environmental*, 2006, **62**, 104-114.
- 9 E. K. Lee, K.-D. Jung, O.-S. Joo and Y.-G. Shul, *Applied Catalysis A: General*, 2005, **284**, 1-4.
- 10 A. Kuch, *Corrosion Science*, 1988, **28**, 221-231.
- 11 K. Shi, L.-M. Peng, Q. Chen, R. Wang and W. Zhou, *Microporous and Mesoporous Materials*, 2005, **83**, 219-224.
- 12 P. Liu, T. Kendelewicz, J. Gordon E. Brown, E. J. Nelson and S. A. Chambers, *Surface Science*, 1998, **417**, 53.
- 13 E. A. Jarvis and A. M. Chaka, *Surface Science*, 2007, **601**, 1909-1914.
- 14 W. Bergermayer, H. Schweiger and E. Wimmer, *Physical Review B*, 2004, **69**, 195409.
- 15 X. G. Wang, W. Weiss, S. K. Shaikhutdinov, M. Ritter, M. Petersen, F. Wagner, R. Schlögl and M. Scheffler, *Physical Review Letters*, 1998, **81**, 1038.
- 16 A. Rohrbach, J. Hafner and G. Kresse, *Physical Review B*, 2004, **70**, 125426.
- 17 S. A. Chambers and S. I. Yi, *Surface Science*, 1999, **439**, L785-L791.

- 18 S. Thevuthasan, Y. J. Kim, S. I. Yi, S. A. Chambers, J. Morais, R. Denecke, C. S. Fadley, P. Liu, T. Kendelewicz and G. E. Brown, *Surface Science*, 1999, **425**, 276-286.
- 19 K. Y. J. Thevuthasan S, Yi.S.I, Chambers S. A, Morais J Denecke R, Fadley C.S., Liu P, Kendelewicz T and Brown, Jr, G.E., *surface Science*, 1999, **425**, 276-286.
- 20 S. H. Bergermayer.W, Wimmer.E, *Physical Review B*, 2004, **69**, 195409.
- 21 H. J. Rohrbach.A, Kresse.G., *Physical Review B*, 2004, **70**, 125426.
- 22 C. Lemire, S. Bertarione, A. Zecchina, D. Scarano, A. Chaka, S. Shaikhutdinov and H. J. Freund, *Physical Review Letters*, 2005, **94**, 166101.
- 23 Karl M. Kadish, Kevin M. Smith and R. Guilard, *The porphyrin handbook* 1999.
- 24 P. S. C. Oliver P M, Mackrodt W C, *Materials Science and Engineering*, 1993, **1**, 755-760.
- 25 M. A. Henderson, S. A. Joyce and J. R. Rustad, *Surface Science*, 1998, **417**, 66-81.
- 26 J.Wang and J.R.Rustad, *Geochimica et Cosmochimica Acta*, 2006, **70**, 5285.
- 27 C. S. Lo, K. S. Tanwar, A. M. Chaka and T. P. Trainor, *Physical Review B* 2007, **75**, 075425/075421-075425/075415
- 28 J. R. Rustad, B. P. Hay and J.W.Halley, *Journal of Chemical Physics*, 1995, **102**, 427.
- 29 J. R. Rustad, A. R. Felmy and B. P. Hay, *Geochimica et Cosmochimica Acta*, 1996, **60**, 1553-1562.
- 30 T. P. Trainor, A. C. Chaka, P. J. Eng, M. Newville, J. Catalano, G. A. Waychunas and G. E. B. Jr., *Surface Science*, 2004, **573**, 204.
- 31 S.A.Chambers and S. I. Yi, *Surface Science*, 1999, **439**, L785-L791.
- 32 C. M. Eggleston, A. G. Stack, K. M. Rosso, S. R. Higgins, A. W. Bice, S. W. Boese, R. D. Pribyl and J. J. Nichols, *Geochim. Cosmochim. Acta*, 2003, **64**, 1221-1228.
- 33 E. Wasserman, J. R. Rustad, A. R. Felmy, B. P. Hay and J. W. Halley, *Surface Science*, 1997, **385**, 217.

-
- 34 S. Kerisit, D. J. Cooke, D. Spagnoli and S. C. Parker, *Journal of Materials Chemistry*, 2005, 1454.
- 35 S. Kerisit and K. M. Rosso, *Geochimica et Cosmochimica Acta*, 2006, **70**, 1888-1903.
- 36 S. Kerisit and K. M. Rosso, *The journal of Chemical Physics*, 2007, **127**, 124706/124701 124706/124710
- 37 K. S. Tanwar, C. S. Lo, P. J. Eng, J. G. Catalano, D. A. Walko, G. E. B. Jr., G. A. Waychunas, A. M. Chaka and T. P. Trainor, *Surface Science*, 2007, **601**, 460.
- 38 K. S. Tanwar, S. C. Petitto, S. K. Ghose, P. J. Eng and T. P. Trainor, *Geochimica et Cosmochimica Acta*, 2008, **72**, 3311-3325.
- 39 C. R. A. Catlow, *Computer Modelling in Inorganic Crystallography*, Academic press Limited, 1997.
- 40 R. D. Shannon, *Acta Crystallographica*, 1976, **A32**, 751-767.
- 41 R.A.Jackson, M.E.G.Valerio and J. F. d. Lima, *Journal of Physics Condensed Matter*, 2001, **13**, 2147.
- 42 K. J. W. Atkinson, R. W. Grimes, Mark R. Levy, Zoe L. Coull and T. English, *Journal of the European Ceramic Society*, 2003, **23**, 3059–3070.
- 43 N. R. Battaile C C, Srolovitz D J, *Journal of American Ceramic Society*, 1995, **78**, 3915.
- 44 D.Wolf and S.Yip, *Materials, interfaces- atomic level structure and properties*.
- 45 C. R. Stanek, M. R. Bradford and R. W. Grimes, *Journal of Physics Condensed Matter*, 2004, **16**, S2699-S2714.
- 46 C. R. Stanek, R. W. Grimes, M. J. D. Rushton, K. J. McClellan and R. D. Rawlings, *Philosophical Magazine Letters*, 2005, **85**, 445-453.
- 47 D. McLean, *Grain Boundaries in Metals*, Clarendon Press, Oxford, 1957.
- 48 J. B. Goodenough, *Physical Review* 1960, **117**, 1442.
- 49 B. Burton, *Physics and Chemistry of Minerals*, 1984, **11**, 132-139.
- 50 N. E. Brown and A. Navrotsky, *American Mineralogist*, 1994, **79**, 485-496.
- 51 Araujo.G.C and Rangel.M.C, *Catalysis Today*, 2000, **62**, 201-207.

- 52 Q. Zhang and F. Saito, *Journal of Materials Science*, 2001, **36**, 2287-2290.
- 53 Majzlan.J, Navrotsky.A and Evans.B.J, *Physics and Chemistry of Minerals*, 2002, **29**, 515-526.

Chapter4

The properties of the mixed solid solutions, $\text{Fe}_2\text{O}_3\text{-Cr}_2\text{O}_3$ and $\text{Fe}_2\text{O}_3\text{-Al}_2\text{O}_3$.

4.1 Introduction

In this chapter, the thermodynamic stability of Fe-Cr and Fe-Al mixed oxide solid solutions have been considered as a function of temperature and composition. The degree of cation disorder and the effective cell parameters of the mixed oxide as functions of temperature and composition, along with the effect of magnetic interactions and lattice vibrations on the stability of these solid solutions are investigated.

Mixed oxides of Fe-Cr and Fe-Al have attracted interest mainly due to their application in the field of catalysis¹⁻⁶, and extensive research has focused on Fe-Al and Fe-Cr solid solutions. The range of techniques employed in these studies include X-ray⁷⁻¹⁴ and neutron diffraction,^{14, 15} Mossbauer^{8, 10-12, 14} and infrared/Raman^{13, 16, 17} spectroscopies and molecular modelling techniques¹⁸. Hematite (Fe₂O₃), eskolaite (Cr₂O₃) and corundum (Al₂O₃) have the same crystalline structure, which is expected to favour the formation of solid solutions. The formation of solid solution has been reported to depend on the preparation temperature and other synthesis conditions^{10, 11, 14}. We find that Fe₂O₃ and Cr₂O₃ can form a continuous solid solution in the entire concentration range, which is attributed to the similarity of the ionic radii of the cations (Fe³⁺ 0.67 Å; Cr³⁺ 0.64 Å). However, some authors have reported that temperatures as high as 800 K are necessary to stabilise the Fe₂O₃ – Cr₂O₃ solid solution, although the preparation temperature can be reduced to ~623 K by mechanical pre-treatment.¹² For Fe₂O₃ – Al₂O₃ solutions, there is a reduced solubility with a wide miscibility gap, which is in agreement with previous studies^{19, 20}. It has been reported that below 1300K, the mixing of Al-Fe-O systems is very slow²¹. Unfortunately, the high specific surface areas that are desirable for catalytic applications cannot be obtained at high temperatures, and therefore the potential of the stability of these solution systems at lower temperatures is of great practical interest.¹²

In this chapter, atomistic simulation techniques based on classical interatomic potentials are used in combination with statistical mechanics and the addition of a model magnetic interaction Hamiltonian (Chapter 2:Section 2.3.2, 2.3.3, and 2.3.4) to investigate the Fe-Cr-O and Al-Fe-O solid solutions.

4.2 Fe₂O₃-Cr₂O₃ Solutions

In this study, the substitution of Fe³⁺ by Cr³⁺ in a 1x1x1 unit cell and 2x2x1 supercell are considered. Each unit cell contains 12 cation sites, and a 2x2x1 supercell thus contains 48 cation sites. The total and reduced numbers of configurations for each cell as a function of Cr concentration are shown in **Table 4. 1**. In the hematite unit cell, all inequivalent substitutional configurations were calculated over the full range of Cr concentrations (Fe_{12-n}Cr_nO₁₈; $n=0,1, 2, \dots, 12$). For the 2x2x1 supercell only Cr concentrations between 0 and 8.33 mol% (Fe_{48-n}Cr_nO₇₂; $n=0, 1, 2, 3, \text{ and } 4$) were investigated, because for higher doping concentrations the number of configurations involved becomes too large to be computationally feasible. In any case, typical Cr doping of iron oxides in HT-WGS catalysts is only ~8.5 mol% (8wt%).²² The results for the larger supercell can also be used to corroborate those obtained for the smaller cell, and to discuss the presence of any size effects in the simulations.

N_{Cr} / N_{sites}	x	N	M
0/12	0.000	1	1
1/12	0.083	12	1
2/12	0.167	66	9
3/12	0.250	220	19
4/12	0.333	495	50
5/12	0.417	792	66
6/12	0.500	924	90
7/12	0.583	792	66
8/12	0.667	495	50
9/12	0.750	220	19
10/12	0.833	66	9
11/12	0.917	12	1
12/12	1.000	1	1
1/48	0.021	48	1
2/48	0.042	1128	19
3/48	0.062	17296	135
4/48	0.083	194580	1466

Table 4. 1: Total number (N) of configurations with N_{Cr} substitutions in the hematite unit cell with 12 cation sites and in the $2 \times 2 \times 1$ supercell with 48 cation sites, and the number M of inequivalent configurations in each case.

The energies of all inequivalent configurations of Fe³⁺ and Cr³⁺ cations for all compositions of the unit cell were obtained. The energies showed that, as a rule, the lowest-energy configurations of cations are those where the substituted Cr atoms are clustered, forming regions of pure chromium oxide. For example, the lowest energy configuration for the 50% - 50% composition (FeCrO₃) is shown in **Figure 4.1**.

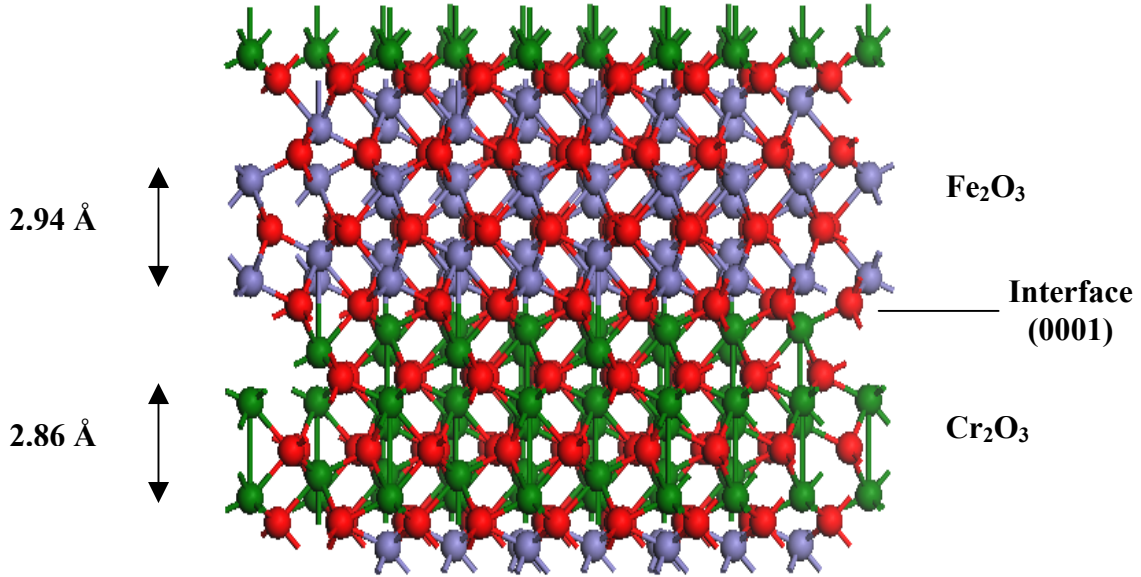


Figure 4.1: The most stable configuration calculated for the composition FeCrO₃ in a single unit cell, showing complete segregation of Fe and Cr cations within the cell. Cations are represented by blue (Fe³⁺) and green (Cr³⁺), O²⁻ anions are shown by red spheres.

In this case, half of the cell is occupied by chromium cations and the other half by iron cations, in a completely segregated distribution. The segregation of the two materials in layers parallel to the (0001) plane occurs, which allows us to calculate the (0001) interface energy between Fe₂O₃ and Cr₂O₃, as:

$$\gamma = \frac{1}{A} (E[\text{FeCrO}_3] - E[\text{Fe}_2\text{O}_3] - E[\text{Cr}_2\text{O}_3]), \quad (4.1)$$

where $E[\text{FeCrO}_3]$ is the lattice energy of the mixed system including the interface, $E[\text{Fe}_2\text{O}_3]$ and $E[\text{Cr}_2\text{O}_3]$ are the lattice energies of an equal number of pure iron and chromium oxide bulk units respectively, and A is the area of the interface. The interfacial energy is then calculated to be $\gamma = 1.49 \text{ Jm}^{-2}$, a reasonably low value which shows that the formation of such an interface is not energetically prohibitive. For comparison, the calculated surface energies of the free Fe₂O₃ and Cr₂O₃ (0001) surfaces are $\gamma = 2.41 \text{ Jm}^{-2}$ and $\gamma = 3.20 \text{ Jm}^{-2}$,

respectively, indicating that the $\text{Fe}_2\text{O}_3/\text{Cr}_2\text{O}_3$ interface in the [001] direction is thermodynamically more stable than the isolated (0001) surfaces for both materials. The geometries at both sides of the $\text{Fe}_2\text{O}_3/\text{Cr}_2\text{O}_3$ interface are very similar, except for a small difference in the interlayer distances perpendicular to the interface, which are smaller for the Cr_2O_3 phase than for the Fe_2O_3 phase, as shown in **Figure 4.1**.

A simple inspection of the $\text{Fe}_2\text{O}_3\text{-Cr}_2\text{O}_3$ system showed that the energies of all the different configurations are very similar (**Figure 4.2**). For example, there are 90 different configurations were generated when six dopants were substituted in the $1 \times 1 \times 1$ unit cell. **Figure 4.2** shows that the difference in energies of these configurations are negligible. Therefore, a great degree of disorder would be expected in the solid solution. The fact that configurations with Cr clustering have lower energies should not be interpreted as a particular trend of cation ordering in the system, but it is an indication of a (weak) tendency to phase separation as explained earlier.

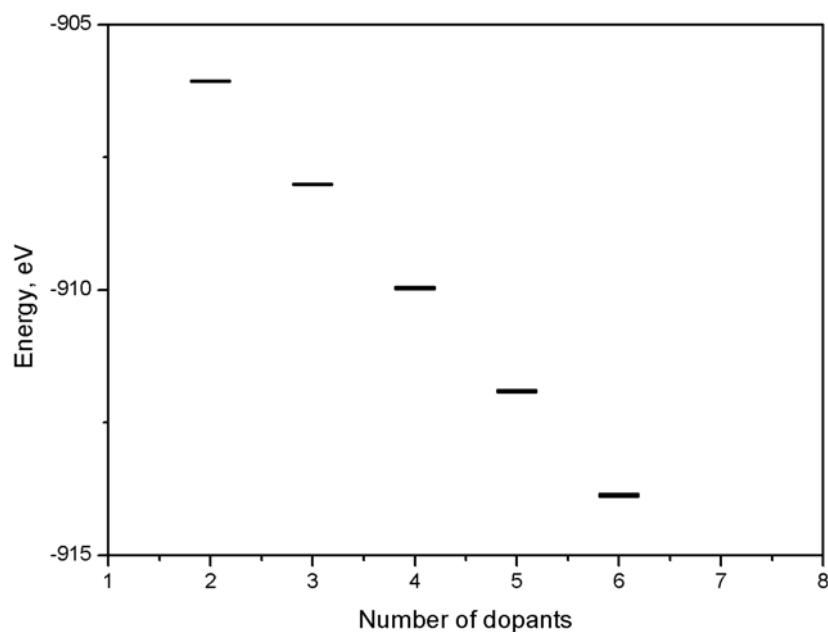


Figure 4.2 : The energies of different configurations of the same composition are plotted as a function of number of dopants.

To compare the stability of the solution with that of the separated components, the (zero-pressure) enthalpies and free energies of mixing as a function of composition have been computed for a number of temperatures,

as:

$$\Delta H_{\text{mix}} = E[(\text{Fe}_{1-x}\text{Cr}_x)_2\text{O}_3] - (1-x)E[\text{Fe}_2\text{O}_3] - xE[\text{Cr}_2\text{O}_3] \quad (4.2)$$

and

$$\Delta G_{\text{mix}} = G[(\text{Fe}_{1-x}\text{Cr}_x)_2\text{O}_3] - (1-x)G[\text{Fe}_2\text{O}_3] - xG[\text{Cr}_2\text{O}_3] \quad (4.3)$$

respectively, where $E[(\text{Fe}_{1-x}\text{Cr}_x)_2\text{O}_3]$ is the average energy calculated while $G[(\text{Fe}_{1-x}\text{Cr}_x)_2\text{O}_3]$ is the configurational free energy of the solid solution, calculated from the energies or vibrational free energies of all different cation arrangements.

The results as a function of temperature are shown in **Figure 4.3 (a)**. The enthalpy of mixing of the solid solution is small, but positive, and therefore the mixing is an energetically unfavourable process. However, the thermodynamic stability of the solution is given by the free energy of mixing, which in this calculation is negative at all temperatures of interest, indicating the formation of stable solid solutions. The results are practically the same regardless of whether we include or exclude vibrational effects. The vibrational correction to the free energy of mixing is always less than 10 meV per unit cell, even at 600 K. On the basis of this result, in the calculations with larger cells, the vibrational contributions are ignored. This is significant from a technical point of view, not only because each free energy minimisation is more expensive than a simple lattice energy minimisation, but also the inclusion of vibrational contributions requires a separate set of energy minimisations at each temperature. The same set of configuration energies without including the vibrational effects can now be used for the statistics at any temperature.

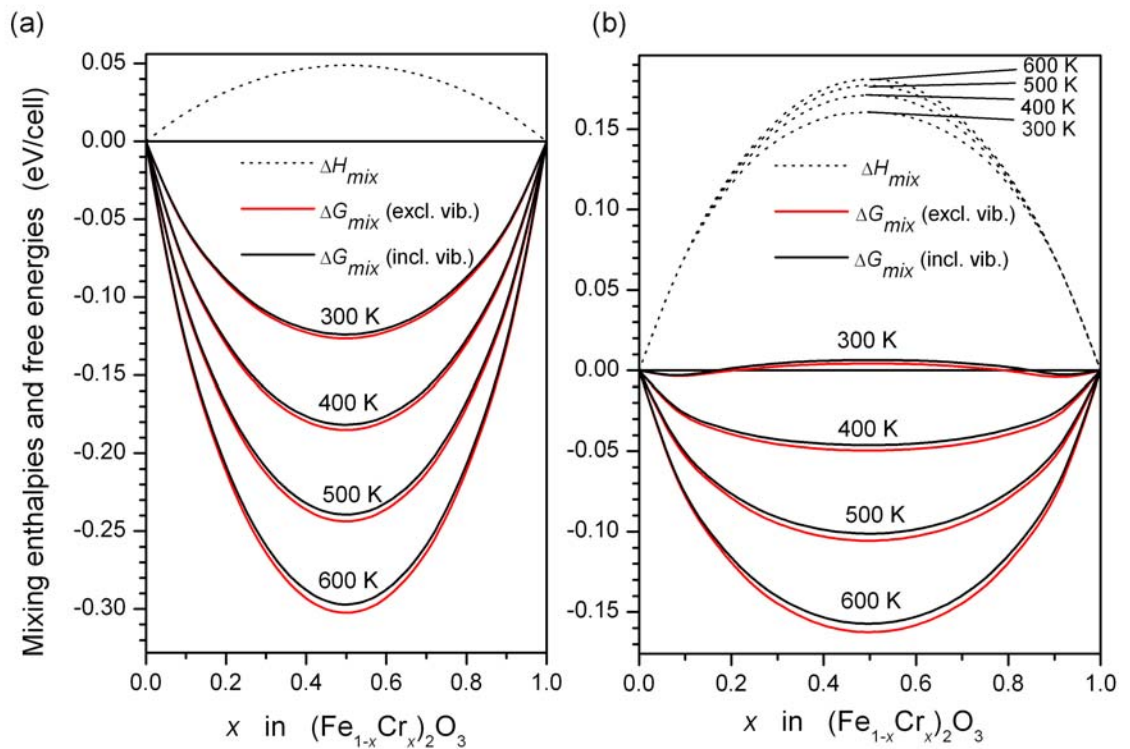


Figure 4.3: Free energy of mixing and enthalpy of mixing of the system as a function of composition, as calculated for a single unit cell. a) without magnetic contributions b) including magnetic effects. (The red line represents the calculations without the vibrational contributions, which are found to be very similar to those including vibrational contributions. The dotted line represents the enthalpy of mixing of the solution.)

The results presented above seem to contradict experimental information¹², which shown that $\text{Fe}_2\text{O}_3 - \text{Cr}_2\text{O}_3$ solid solutions are stabilised throughout the whole range of compositions, only if the mixture is heated to temperatures a few hundred degrees above room temperature. However, as pointed out by critics^{14, 23}, the reason for the instability of the solutions might not be thermodynamic in nature, but instead associated with the synthesis conditions. Still, these initial calculations may be underestimating the enthalpies of mixing of the system, and

therefore the critical temperature above which the complete solution series can form. This could be due to the presence of relatively strong magnetic interactions in the material that so far have not been included so far in this study.

4.2.1 Magnetic Effects

Both Fe_2O_3 and Cr_2O_3 are antiferromagnetic solids, although with different magnetic arrangements. The difference in the superexchange coupling strengths between Fe – Fe and Cr – Cr pairs (the Néel temperature is 955 K in hematite, but only 300 K in eskolaite), suggests that magnetic interactions might play a significant role in the thermodynamics of mixing. It seems that these interactions could increase the enthalpies of mixing in the solution, by reinforcing the stability of Fe – Fe pairs of neighbours, where the magnetic stabilisation energy is most important.

A simple way to estimate the effect of magnetic interactions is to include a magnetic contribution, (**section 2.3.4**) in the energy calculation for each configuration. As the Fe – Fe magnetic interactions are much stronger than the Cr – Cr interactions (at the temperatures of interest here, above room temperature and up to 900 K, pure Fe_2O_3 is antiferromagnetic while pure Cr_2O_3 is already paramagnetic), only the Fe – Fe interactions are included in this model by assuming that these interactions have the same strength as in pure hematite. Furthermore, the iron spins have the same orientation as they have in the pure oxide. Despite these approximations, we should be able to obtain reasonable estimates of the magnetic contribution to the energy of each configuration. Two different coupling constants were included, one for the neighbouring Fe^{3+} pairs with Fe – O – Fe angle of $\sim 132^\circ$ and one for pairs with an angle of $\sim 118^\circ$. As pointed out by Cox *et al.*¹⁵, the antiferromagnetic ordering of hematite can be derived by the consideration of these two interactions. The values of the corresponding J constants (-23.2 K and -29.7 K, respectively) were taken from the experimental determination by Samuelsen and Shirane²⁴.

As expected, the inclusion of the magnetic contribution increases the enthalpy of mixing of the solid solution with respect to the non-magnetic model, **Figure 4.3 (b)**. Perhaps less expected is the fact that the estimated magnetic contribution to the enthalpy of mixing is more significant than the original contribution from the interatomic potentials. Therefore, magnetic interactions may play a crucial role in the thermodynamics of mixing of these solid solutions, especially at low temperatures. The enthalpies of mixing now become large enough to yield positive values of the mixing free energies for intermediate compositions at room temperature. In **Figure 4.3 (b)**, the line corresponding to 300 K has two minima, one at Fe-rich compositions and one at Cr-rich compositions, indicating the two phases into which any intermediate composition would separate, if kinetically allowed. This thermodynamic miscibility gap disappears at slightly higher temperatures.

4.2.2 Configurational Entropy

In **Figure 4.4**, the variation of the configurational entropy of the solid solution with temperature (solid lines) is plotted. At each value of x , the dotted line represents the maximum entropy that can be obtained for this cell size at that Cr concentration, as given by

$$S_{\max} = k_B \ln N = k_B \ln \frac{(N_{\text{sites}})!}{(xN_{\text{sites}})!(N_{\text{sites}} - xN_{\text{sites}})!} \quad (4.4)$$

where x is the concentration of Cr, k_B is the Boltzmann constant and N is the total number of sites.. The values of $N(x)$ are those listed in **Table 4. 1**.

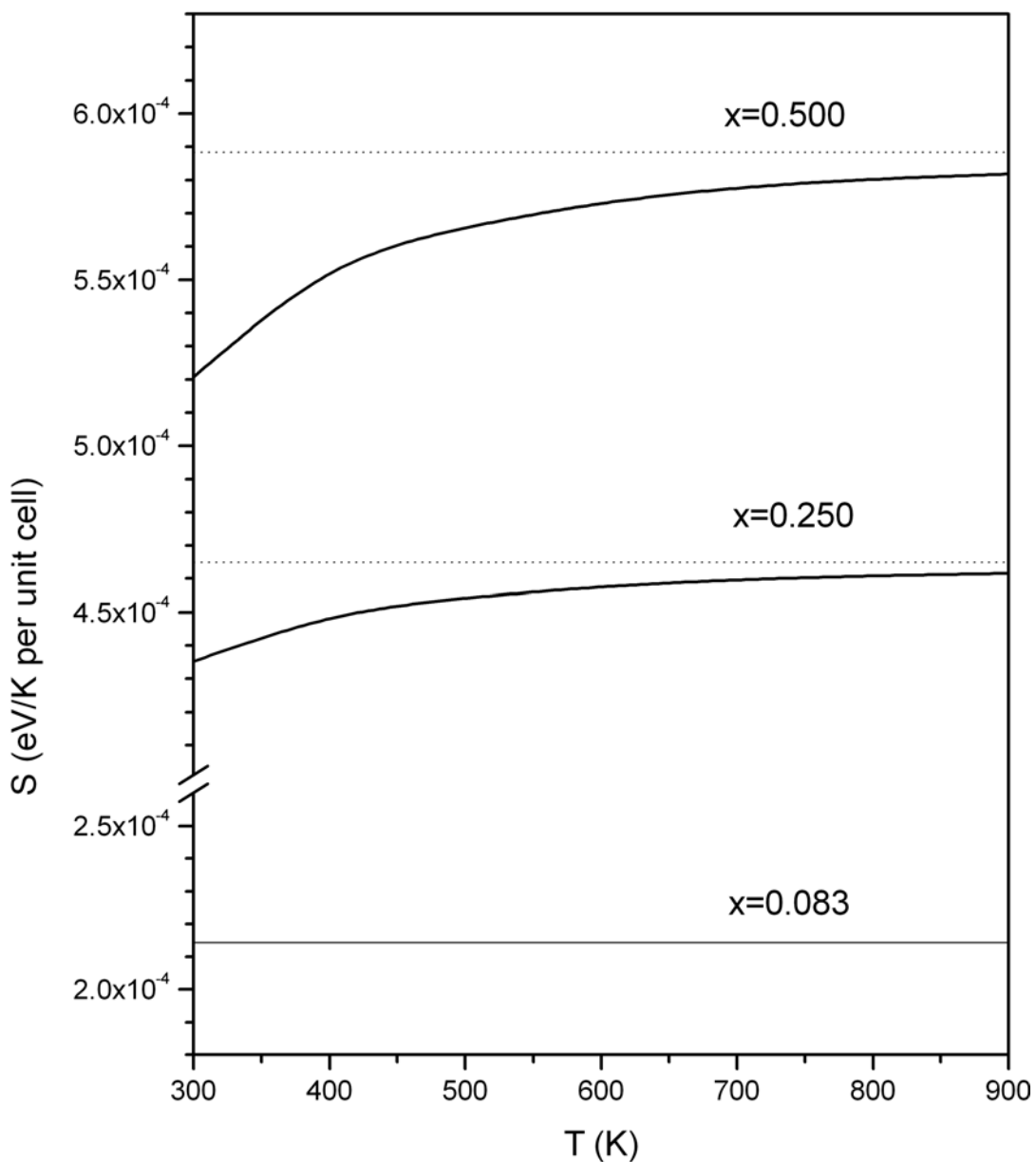


Figure 4.4: Variation with temperature of the configurational entropy calculated in the hexagonal unit cell. Dotted lines represent the maximum entropies obtainable at each composition in this cell.

Since the case $x=0.083$ corresponds to the cell with one substitution at any of the 12 equivalent cation sites of the cell, all the configurations have the same energy and the entropy has its maximum possible value for the cell. At other concentrations, where several different distributions of the cations are possible, the entropy deviates from the maximum value, especially at lower temperatures, but not by a great amount. For example, when $x=0.25$ ($x=0.5$), the configurational entropy reaches 96% (94%) of its maximum value at 400 K, and 98% at 600 K. This means that the solid solution is almost ideally disordered at all temperatures of interest, in agreement with experimental observations, where neutron diffraction studies of this system have not found any evidence of ordered superstructures in samples synthesized at 923 K.¹⁴

However, conclusions from different authors about the mixed Fe-Cr oxide properties are sometimes contradictory. Busca *et al.*¹⁷ have considered that a band in the Raman spectra of the 50%-50% solid solution that was absent in the end members, indicates an ilmenite-type ordering of the cations, but the corresponding superstructural reflections have not been found in the X-ray diffraction patterns. The cation ordering hypothesis has been rejected by Grygar *et al.*¹⁴ on the basis of careful neutron diffraction studies of a structure with $x=0.5$, in which no superstructural peaks could be found, despite the high sensitivity of neutron diffraction to the hypothetical superstructures.

The calculated degree of disorder, as given by the entropy, depends on the size of the cell. In the above-described calculations, a relatively small cell with only 12 cation sites is employed to check the variation of the calculated thermodynamic properties with cell size. To this end, a cell doubled in both the a and b directions (the c/a ratio in the unit cell is 2.6 – 2.7), with 48 cation sites was also considered. In this supercell, the composition $x=0.083$ corresponds to 4 Cr substitutions, and therefore several configurations were calculated (the number of inequivalent configurations is $M=1466$). The structures of these configurations were optimised to obtain their equilibrium energies, including the magnetic term discussed earlier in **section 4.2.1**, but neglecting vibrational effects, which, as we

have seen, do not contribute significantly to the thermodynamics of mixing. The resulting enthalpy of mixing in the supercell was 58 meV (average per unit cell), i.e. only 5% less than the value calculated for the small cell (61 meV).

However, cell size effects can be more important in the calculation of configurational entropies rather than mixing enthalpies. At $x=0.083$, for example, the calculated entropy shows no significant deviation from the maximum entropy obtainable in the $(2 \times 2 \times 1)$ supercell (2.62×10^{-4} eV/K per unit cell) at any temperature above 300 K, although this value represents a 22% increase with respect to the value calculated for the same x in the small cell (2.14×10^{-4} eV/K per unit cell). It seems that, at these small concentrations and temperatures above 300 K, no significant departure can be expected from the maximum disorder obtainable at each supercell size. It is therefore justified to extrapolate the entropy to its infinite cell value using the full-disorder limit given by

$$S_{\infty} = k_B N_{\text{sites}} (-x \ln x - (1-x) \ln(1-x)) \quad (4.5)$$

which yields 2.96×10^{-4} eV/K per unit cell for $x=0.083$. At higher Cr concentrations, there is some departure from the ideal disorder behaviour (as discussed above), however, such deviations are still relatively small. Higher concentrations are also less interesting from a catalytic point of view.

The mixing potentials are recalculated and corrected for size effects, by using the infinite size limit for the entropy, while keeping the enthalpy of mixing obtained in the $(2 \times 2 \times 1)$ supercell, which is done by extrapolating other x values using a quadratic function. The numerical simulations show that at room temperature (300 K), there is a thermodynamic miscibility gap between $x=0.17$ and $x=0.83$, which quickly reduces when the temperature increases, and disappears at ~ 360 K. A miscibility gap that closes at these low temperatures is unlikely to be observed experimentally as the slow ion diffusion prevents thermodynamic equilibrium. Therefore the results from this study support the conclusion that there are no miscibility gaps of thermodynamic origin in the Fe₂O₃-Cr₂O₃ system at the usual synthesis temperatures.

4.2.3 Vegards Law: Relation between the cell parameter and the composition of the defect

According to Vegards law²⁵, there is a linear relationship between the lattice cell parameter and concentration of the defect. The calculated a and c parameters for each composition are plotted in **Figure 4.5**, as functions of the Cr concentration. These values represent averages of the configurational space assuming full disorder. The use of any finite-temperature distribution of cations produces a negligible change in the average cell parameters, which seem to depend mainly on the composition and very little on the particular cation distribution within the cell. The thermal expansion at room temperature with respect to the 0 K structure has been considered in the calculation. The parameters used in the configurational averaging are those resulting from the minimisation of the free energy in the quasi-harmonic approximation. This vibrational effect is small and consists of a nearly isotropic volume expansion of 0.52% for pure Fe₂O₃ and 0.42% for pure Cr₂O₃, with a linear variation in between.

The cell parameters decrease with the Cr concentration as expected from the smaller ionic radius of Cr³⁺ compared to that of Fe³⁺, and in agreement with experimental results.^{7, 14} It is interesting to note that experimentally the decrease is not linear with respect to the Cr concentration, with a and c having small positive and negative curvatures, respectively, with respect to the concentration. This behaviour is not reproduced by our simulations, where we obtain a perfect linear correlation between each cell parameter and the Cr concentration, following Vegard's law.

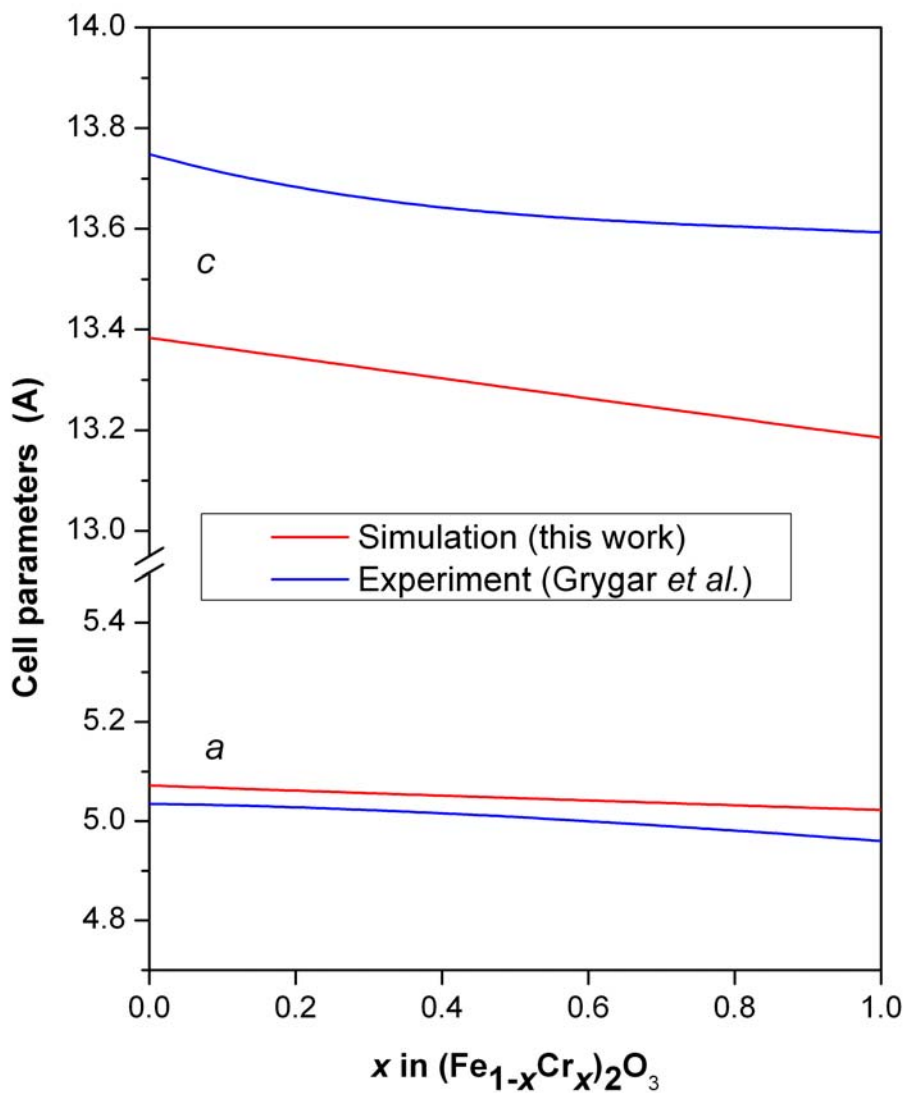


Figure 4.5: Variation of the cell parameters of the solid solution with Cr concentration, in comparison with experimental results (blue lines are cubic polynomial fits to experimental data, as given by Grygar *et al.*¹⁴). Calculated values represent configurational averages.

In principle, the experimental deviation from Vegard's law could be related to the presence of cation ordering, which has been suggested by Busca *et al.*¹⁷ based on an interpretation of the Raman spectrum of the solid solution. However, in the case of the Fe₂O₃ – Cr₂O₃ system, this explanation is unlikely, as no evidence of superstructure formation has been found in diffraction studies.¹⁴ Furthermore, because of the positive enthalpy of mixing of the system, the solid solution only forms at temperatures that are high enough for significant disorder to be present, allowing an entropic stabilisation of the solution. Therefore, the non-vegardian behaviour of this system is more likely to be due to the presence of magnetic or other specific cation – cation interactions, as previously suggested by Grygar *et al.*¹⁴ Although our calculations now include magnetic interactions via the introduction of exchange coupling constants, the present approach introduces corrections only to the energies and not to the local structures, for which geometry-dependant J values would be necessary. The only magnetic effects on the cell parameters that could be obtained from this model are those acting via a modification of the cation distribution. However, the cell parameters in these calculations are not sensitive to the substitutional configurations. Therefore, we suggest that the deviation from Vegard's law is a consequence of magneto-structural effects in the mixed oxide.

4.3 Comparison of Fe₂O₃ – Cr₂O₃ and Fe₂O₃-Al₂O₃

Solutions

In this section, another dopant system, Fe₂O₃ – Al₂O₃ is discussed and compared with the Fe₂O₃ – Cr₂O₃ solutions. As our previous studies²⁶ have revealed that the size of the unit cell has very little effect on these systems, in order to save computer effort, only the 1 x 1 x1 cell consisting of 12 cation sites is used. The energies of different configurations vary considerably, indicating that cation ordering can be expected in the mixed solution system.

4.3.1. Mixing Energies and Cation Ordering

The mixing enthalpies and free energies have been calculated (explained in **section 4.2**) for the Fe₂O₃-Al₂O₃ solutions with and without vibrational contributions. Bouree *et al*²⁷ reported on the basis of neutron diffraction studies that mixed Al oxides undergo a magnetic phase transition at 280 K, although there is no other experimental evidence to verify their findings. The results from the calculated Fe₂O₃ – Cr₂O₃ solutions showed that magnetic contributions play an important role in these systems, so the magnetic effects of the Fe-Fe pairs are again included in the calculations.

The mixing energies for different temperatures are shown in **Figure 4.6**. The effect of the vibrational contributions was small in the Fe₂O₃ – Cr₂O₃ solutions, but in the Fe₂O₃ – Al₂O₃ solid solutions the vibrational effects are not negligible, as can be seen in **Figure 4.6**. The mixing free energies confirm that there is a wide miscibility gap in the entire range of composition and thus no mixing is expected at lower temperatures. Even at high temperatures (*e.g.* 1200 K), the free energy of mixing is still positive, indicating that the separation of the system into two pure phases is thermodynamically preferred. Fe₂O₃ – Al₂O₃ solutions thus do not mix as easily as Fe₂O₃ – Cr₂O₃ solutions, which can be attributed to the difference in the ionic radii between Fe³⁺ (0.645 Å) and Al³⁺ (0.535 Å). This size difference is attributed to many characteristics of Fe-Al mixed solutions, for example the unit cell volume decrease exhibited in these solutions as the concentration of Al³⁺ increases and the surface area increase, which has an impact on the catalytic properties⁶. Due to the size difference of these ions, the particle size is shifted towards smaller equilibrium particles, thereby increasing the surface area of hematite, which is one of the criteria for a good catalyst.

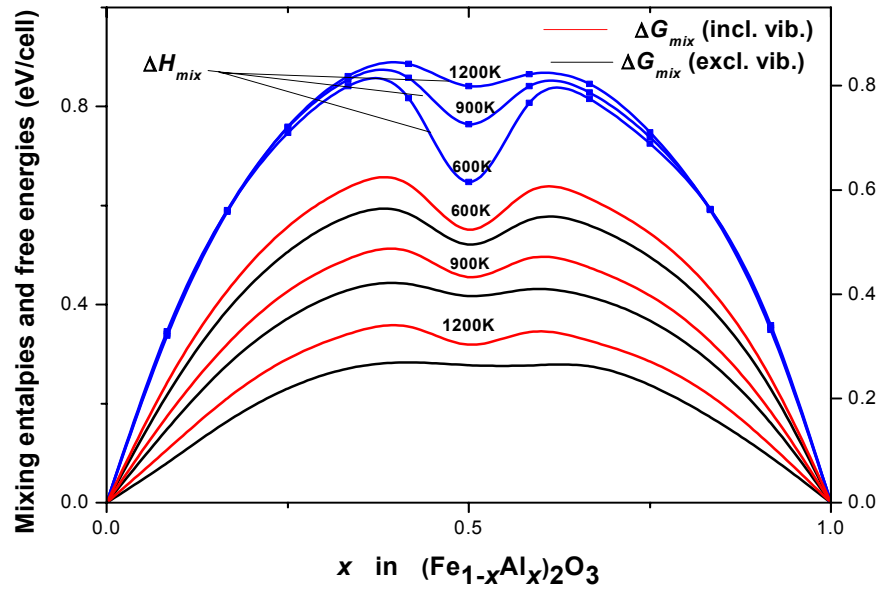


Figure 4.6: Free energy of mixing (red and black) and enthalpy of mixing (blue) of the system as a function of composition, as calculated for a single unit cell, red lines represent the inclusion of vibrational contributions. Magnetic effects are included in both cases.

The enthalpy of mixing of $\text{Fe}_2\text{O}_3 - \text{Al}_2\text{O}_3$ is also positive and remains so even at higher temperatures (**Figure 4.6**), which shows that the formation of a solution is strongly endothermic which agrees with the experimental results of Majzlan *et al*¹⁸. For the $\text{Fe}_2\text{O}_3 - \text{Cr}_2\text{O}_3$ system, at each concentration of the dopant x , the entropy quickly reaches its maximum value. The configurational entropy is close to its maximum value, (**Figure 4.4**) which is an indication of completely disordered site occupancy in the solid, illustrating that the $\text{Fe}_2\text{O}_3 - \text{Cr}_2\text{O}_3$ system behaves as an ideal solid solution even at relatively low temperatures of around 300 K. The absence of cation ordering in this system is further confirmed by experimental results.¹⁴ However, the contribution of the entropy term in the $\text{Fe}_2\text{O}_3 - \text{Al}_2\text{O}_3$ solutions is too small to stabilize the system even at high temperatures, although as the temperature decreases, a stable ordered phase with a 50:50 composition, begins to appear. The minimum at $x = 0.5$ in **Figure 4.6** is the result of preferential ordering at the 50:50 composition, suggesting that a meta-

stable ordered structure can be found at a concentration of $x = 0.5$. **Figure 4.7** shows the entropy at $x = 0.5$ is also lower than for the other compositions, which may result in a kind of separation or ordering of the system. The difference between the enthalpy of mixing and free energy of mixing dominates, suggesting only a small contribution of configurational entropy, which is not enough to stabilise the mixed solution system. Therefore, the $\text{Fe}_2\text{O}_3 - \text{Al}_2\text{O}_3$ solution is only metastable with respect to the pure phases and is expected to separate if exposed to temperatures high enough to allow cation redistribution. Due to the high thermal resistance of Al_2O_3 , the mixing of Fe-Al oxides occurs only at high temperatures²⁸. In **Figure 4.8** the variation of the configurational entropy of Fe-Al and Fe-Cr solid solutions with temperature and composition are plotted, which again suggest that the Al system is more ordered compared to the Cr doped system.

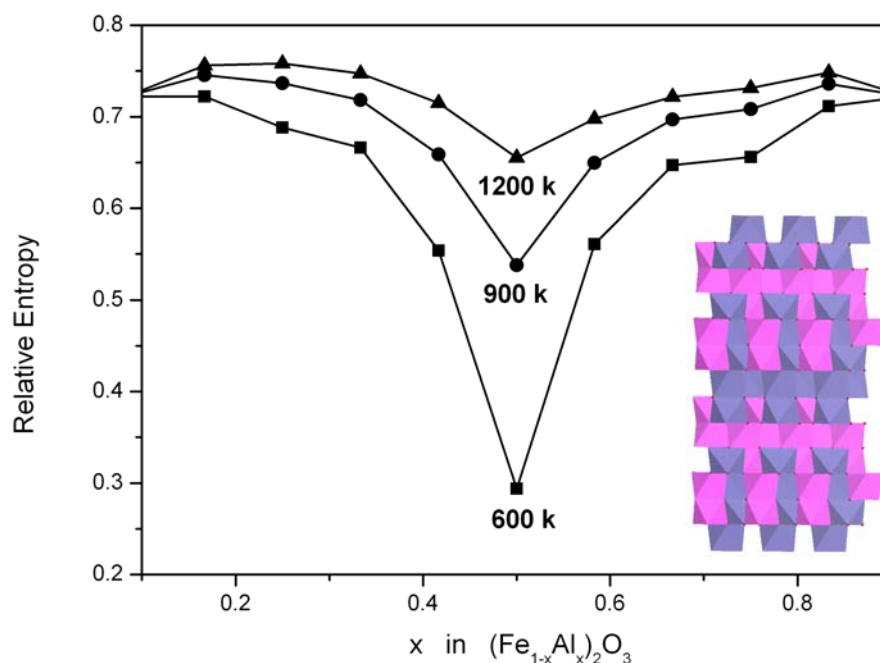


Figure 4.7: The relative entropy of the Fe-Al solution system at different temperatures plotted as a function of composition. Inset: The ordered lower energy structure of the 50:50% composition Fe-Al solution system. Blue represents Fe^{3+} , pink represents Al^{3+} and small red circles represent O^{2-} .

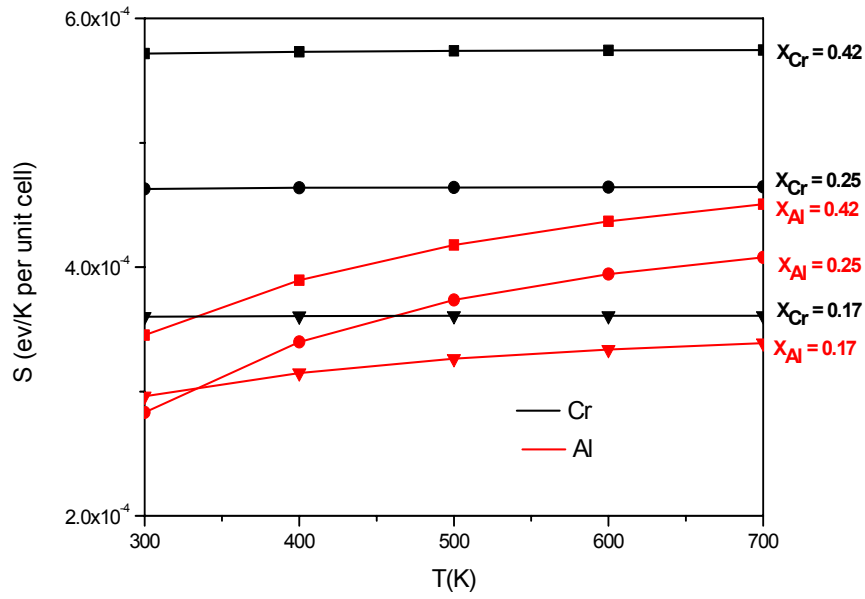


Figure 4.8: Comparison of the configurational entropy of Fe-Cr and Fe-Al solutions.

The magnetic contributions to these mixed solutions are investigated by including the magnetic interactions in the simulations,

$$E = E_{IP} - 2 \sum_{\{Fe, Fe_j\}_{NN}} J_{ij} S_i S_j \quad (4.6)$$

where the first term E_{IP} is the paramagnetic contribution from the simulations and the second term is the magnetic ordering contribution. The J values are taken from experiment²⁴.

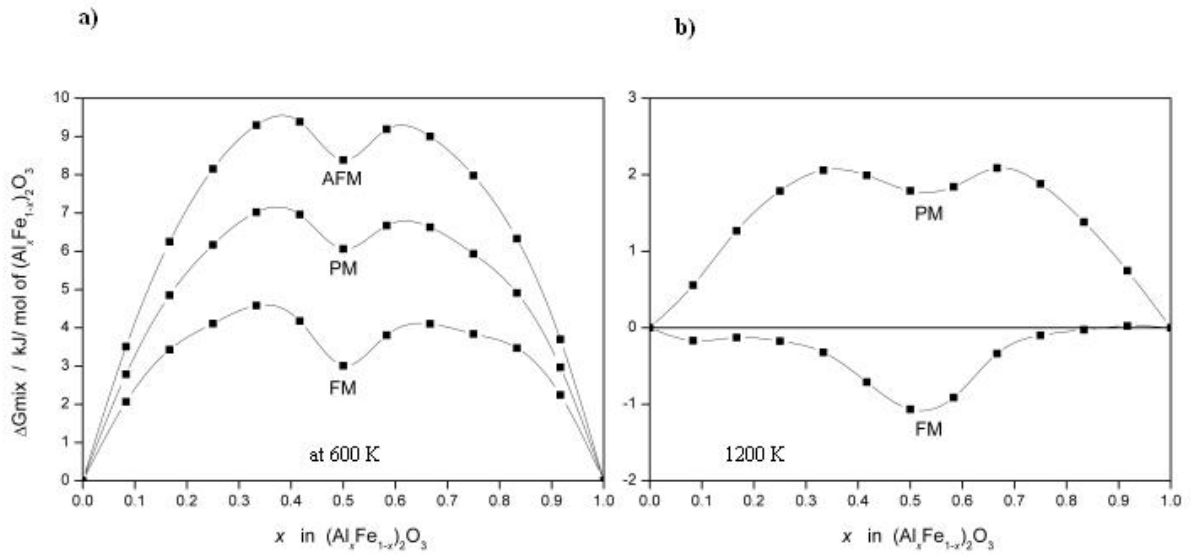


Figure 4. 9: The free energy of mixing between Fe_2O_3 and Al_2O_3 at 600K (a) and 1200K (b). (AFM refers to antiferromagnetic, PM term paramagnetic and FM ferromagnetic.)

In order to investigate the dependence of temperature in the magnetic ordering of Fe-Al mixed oxides, the free energy of mixing is calculated with the inclusion of magnetic ordering contributions (Eqn.4.6). This will provide information on the preparation of Fe-Al oxides at reduced temperature, or to increase the solubility of dopant Al in Fe_2O_3 solutions at low temperatures. **Figure 4. 9** displays the magnetic stabilization of Al in hematite at 600K and 1200K (the Neel temperature of hematite is 955K). (**Figure 4. 9 (a)**) indicates that similar to the Fe-Cr solutions, magnetic interactions in Fe-Al solutions are also important and the inclusion of magnetic terms will result in a drop in the free energy of mixing. Burton et al²⁹ used the cluster variation method to study the temperature dependence of the antiferromagnetic - paramagnetic transition of the mixing of $\text{Fe}_2\text{O}_3\text{-FeTiO}_3$ systems. When applying the magnetic interactions, the paramagnetic system appears to be ferromagnetic, i.e., magnetic ordering, which would enhance the mixing of oxides, which is in agreement with our results, however, these results are hypothetical as the magnetic structure of hematite is very complex; hence more research is needed in this area. In addition, only in the presence of a very strong magnetic field, the system will become ferromagnetic. Unfortunately this kind of strong magnetic field is not widely available.

To conclude this part, the Fe-Al-O solid solution is meta-stable with respect to the separated phases and the mixed solution will only exist at very high temperature. The calculated results verify the results reported by some authors^{18,21} that the solution is stable above 1600K. However, many authors^{6,30,31} have drawn contradictory conclusions regarding the segregational characteristics of the system, which retards the sintering process as suggested by Araujo⁶ and Topsøe³⁰. However, Oliveira *et al*³¹ argued that aluminium did not significantly affect crystallization, as it is expected to go into the lattice rather than remain as a separate phase. The system exhibits some kind of ordering, as shown by the results of the surface segregation of Al in hematite (**section 3.3.2**). The bond energy of Al-O (512.1 kJ/mol)³² is larger than that of Fe-O (390.4 kJ/mol), which could contribute to the crystallisation behaviour reported by Scherwtmann³³ and the segregation behaviour exhibited in the system. For both Fe₂O₃ – Cr₂O₃ and Fe₂O₃ – Al₂O₃ solutions, the magnetic contribution has a significant effect, indicating that the mixing of solid solutions may be easier with the application of a magnetic field.

4.3.2. Deviation from Vegards Law

A strain is induced in Fe₂O₃ – Al₂O₃ solutions when Al³⁺ replaces Fe³⁺. Majzlan *et al*¹⁸ argued that this strain causes a distortion of the hexagonal network of oxygen ions, while the metal ions remain in the same position. Zoppi *et al*³⁴ conducted a vibrational infrared study, which has verified that the introduction of Al³⁺ induces a strain in the lattice of hematite, thereby leading to a decrease in the lattice parameters. Many authors^{33,35} argued that the lattice parameters of Al-hematite show a deviation from the ideal behaviour, according to Vegards law²⁵. The calculated cell parameters show a decrease as the Al³⁺ concentration increases, which is expected from the smaller ionic radius of Al³⁺ compared to that of Fe³⁺ in good agreement with the experimental results suggested by Zoppi *et al*. However, experimentally the decrease is not linear, with both *a* and *c* parameters showing curvatures with respect to the concentration. At low temperature, there is a positive deviation and at high temperature there is a slight negative deviation as reported by Majzlan *et al*¹⁸ in their

calorimetry studies. The simulations from this work suggest that the deviation from ideal mixing is less at high temperatures, **Figure 4.10**, **Figure 4.11**.

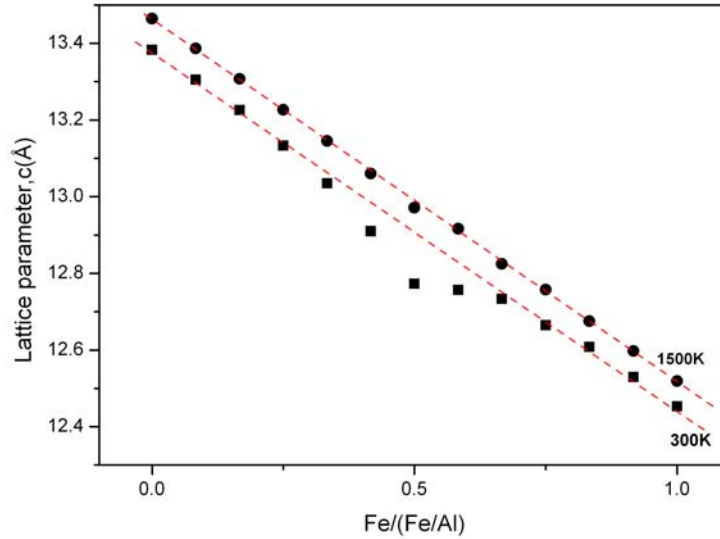


Figure 4.10: Variation of the cell parameter, c of the solid solution with Al concentration, at 300K and 1500K temperatures. The dashed lines represent ideal mixing (Vegard's law). As the temperature increases, the deviation from an ideal solution is small.

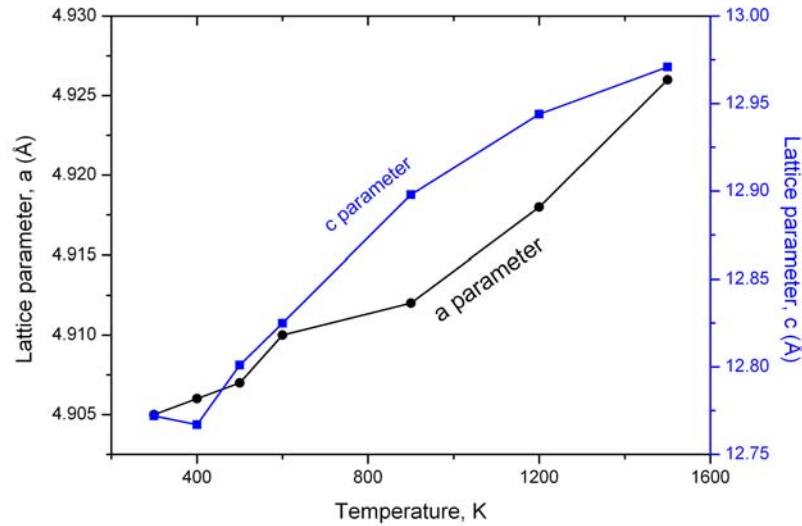


Figure 4.11: Variation of the lattice parameters, a and c of Fe-Al mixed solution at 50% composition as a function of temperature.

The deviation can be explained with the help of Vegards law, and is related to the presence of cation ordering. There is evidence of superstructure formation in these solutions, reported from diffraction studies²². This cation ordering also explains the wide miscibility gap evident in these solutions as discussed earlier. Our studies verified that the strain experienced in these solutions decreases with temperature and is assumed to disappear at very high temperatures.

4.4 Summary

A theoretical investigation into the stability and structural behaviour of $(\text{Fe}_{1-x}\text{Cr}_x)_2\text{O}_3$ and $(\text{Fe}_{1-x}\text{Al}_x)_2\text{O}_3$ mixed oxides has showed that these two solutions exhibit entirely different characteristics. $(\text{Fe}_{1-x}\text{Cr}_x)_2\text{O}_3$ solutions have small but positive enthalpies and free energies of mixing, a significant part of which seem to be due to contributions of magnetic origin. Furthermore, they are thermodynamically stable in the whole range of compositions at all temperatures above ~ 400 K. Only very small deviations from fully disordered distributions of cations should be expected, in agreement with the most recent experimental evidence. There are no thermodynamic limitations for Cr doping in Fe_2O_3 , whereas the $(\text{Fe}_{1-x}\text{Al}_x)_2\text{O}_3$ solution is metastable and is expected to form separate phases even at very high temperatures, exhibiting a wide miscibility gap.

The calculations also show a decrease in the cell parameters of the solid solution as the Cr or Al content increases, as obtained experimentally. It is suggested that the small deviation from linearity of this dependence is due to magnetic interactions of the cations in Cr solutions, whilst in the case of Al solutions, it could be due to cation ordering.

In the preparation of active WGS catalysts, the precursor material, hematite is reduced to magnetite. In the next chapter, we have modelled maghemite, which is an intermediate in the reduction process and also represents an interesting starting point for calculations of the highly complex magnetite structure.

4.5 References

1. M. V. Twigg, *Catalyst Handbook*. 2 ed.; Wolfe Publishing: London 1989; 268-288.
2. C. Rhodes; G. J. Hutchings; A. M. Ward, *Catalysis Today* **1995**, 23, (1), 43-58.
3. R. J. Willey; H. Lai; J. B. Peri, *Journal of Catalysis* **1991**, 130, (2), 319-331.
4. J. S. Walker; G. I. Straguzzi; W. H. Manogue; G. C. A. Schuit, *Journal of Catalysis* **1988**, 110, (2), 298-309.
5. S. Natesakhawat; X. Wang; L. Zhang; U. S. Ozkan, *Journal of Molecular Catalysis A: Chemical* **2006**, 260, (1-2), 82-94.
6. G. C. Araujo; M.C.Rangel, *Catalysis Today* **2000**, 62, 201.
7. H. E. V. Steinwehr, *Z. Kristallographica* **1967**, 125, 377.
8. A. K. Bhattacharya; A. Hartridge; K. K. Mallick; C. K. Majumdar; D. Das; S. N. Chintalapudi, *Journal of Materials Science* **1997**, 32, (3), 557-560.
9. J. Manjanna; G. Venkateswaran, *Industrial & Engineering Chemistry Research* **2002**, 41, (13), 3053-3063.
10. S. Music; M. Lenglet; S. Popovic; B. Hannover; I. CzakoNagy; M. Ristic; D. Balzar; F. Gashi, *Journal of Materials Science* **1996**, 31, (15), 4067-4076.
11. S. Music; S. Popovic; M. Ristic, *Journal of Materials Science* **1993**, 28, (3), 632-638.
12. P. Tsokov; V. Blascov; D. Klissurski; I. Tslovski, *Journal of Materials Science* **1993**, 28, 184-188.
13. M. I. Baraton; G. Busca; M. C. Prieto; G. Ricchiardi; V. S. Escribano, *Journal of Solid State Chemistry* **1994**, 112, (1), 9-14.
14. T. Grygar; P. Bezdicka; J. Dedecek; E. Petrovsky; O. Schneeweiss, *Ceramics-Silikaty* **2003**, 47, (1), 32-39.
15. D. E. Cox; G. Shirane; W. J. Takei, *Journal of Physics and Chemistry of Solids* **1963**, 24, (3), 405-&.
16. K. F. McCarty; D. R. Boehme, *Journal of Solid State Chemistry* **1989**, 79, (1), 19-27.

17. G. Busca; G. Ramis; M. D. Prieto; V. S. Escribano, *Journal of Materials Chemistry* **1993**, 3, (6), 665-673.
18. J.Majzlan; A. Navrotsky; B.J.Evans, *Physics and Chemistry of Minerals* **2002**, 29, 515.
19. A.Muan; C.L.Gee, *Journal of American Ceramic Society* **1956**, 39, 209.
20. L. M. Atlas; W. K. Sumida, *Journal of American Ceramic Society* **1958**, 41, 150.
21. A. Feenstra; S. Samann; B. Wunder, *Journal of Petrology* **2005**, 46, (9), 1881-1892.
22. F. Domka; A. Basinska; R. Fiedorow, *Surface Technology* **1983**, 18, (3), 275-282.
23. Y. Murakami; A. Sawata; Y. Tsuru; K. Akiyama, *Journal of Materials Science* **2003**, 38, (12), 2723-2725.
24. E. J. Samuelsen; G. Shirane, *Physica Status Solidi* **1970**, 42, 241-256.
25. L. Vegard, *Zeitschrift für Physik A Hadrons and Nuclei* **1921**, 5, (1), 17-26.
26. S. Benny; R. Grau-Crespo; N. H. de. Leeuw, *Physical Chemistry Chemical Physics*, **2008**, 11, 808.
27. F. Bouree; J. L. Baudour; E. Elbadraoui; J. Musso; C. Laurent; A. Rousset, *Acta Crystallographica Section B* **1996**, B 52, 217-222.
28. A. Ladavos; T. Bakas, *Reaction Kinetics and Catalysis Letters* **2001**, 73, (2), 223-228.
29. B. Burton; R. Kikuchi, *Physics and Chemistry of Minerals* **1984**, 11, (3), 125-131.
30. H. Topsøe; M. Boudart, *Journal of Catalysis* **1973**, 31, (3), 346-359.
31. A. C. Oliveira; J. L. G. Fierro; A. Valentini; P. S. S. Nobre; M. do Carmo Rangel, *Catalysis Today* **2003**, 85, (1), 49-57.
32. M. A. Wells; R. J. Gilkes; R.R.Anand, *Clay Minerals* **1989**, 24, 513.
33. U.Schwertmann; R.W.Fitzpatrick; R.M.Taylor; D.G.Lewis, *Clays and Clay Minerals* **1979**, 27, 105-112.
34. A. Zoppi; C.Lofrumento; E. M. Castellucci; Ph.Sciau, *Journal of Raman Spectroscopy* **2008**, 39, 40-46.
35. V. Barron; J.L.Rendon; J.Torrent; C.J.Serna, *Clays and Clay Minerals* **1984**, 32, 475-479.

Chapter 5

More Complex Iron Oxides: Maghemite and Isovalent Impurities

5.1 General

Maghemite, $\gamma\text{-Fe}_2\text{O}_3$ is one of the technologically important iron oxides, mainly used in storage media in magnetic recording applications¹. Due to its magneto-optical properties the material can be used as a sensor for the Earth's magnetic field². Apart from its magnetic properties, maghemite also has applications in the field of catalysis^{3, 4} and in a variety of bioseparations⁵. The presence of cation vacancy sites adds complexity to the maghemite structure, and whereas many publications have reported on aspects of maghemite's applications, none have offered a detailed study of the cation site occupancies or defect properties. In certain reactions, such as aldol condensation of acetone, it is essential to maintain the γ - phase, which is more catalytically active than the α - phase (hematite). From a catalytical point of view, it is therefore important to understand the effects of impurities on the phase transition from the γ - to the α - phase.

This chapter presents a comprehensive study of the incorporation of isovalent impurities in maghemite and their preferential site occupancies, any ordering and a speculation on the effect of dopants on the γ - to α - phase transition temperatures.

5.2 Maghemite Model and Bond Distribution

The structure of maghemite is similar to that of the cubic inverse spinel magnetite and the molecular formula can be written as, $[Fe^{3+}]_A \left[Fe_{\frac{2}{3}}^{3+} \Delta_{\frac{1}{3}} \right]_B O_3$ where Δ represents a cation vacancy⁶. The structure is described in detail in Chapter 1. The structure used in this study is optimized with the space group P4₁2₁2(92), which is an ordered structure with vacancies distributed in the octahedral sites (**Table 5.1**). The occurrence of vacancies in the octahedral sites are verified by a number of experimental results, for example, X-ray powder diffraction,^{6, 7} neutron diffraction⁸, Mossbauer spectroscopy and magnetization studies.^{9, 10} A 1x1x3 supercell was created with 64 Fe³⁺ ions, 96 anions and 8 cation vacancies. The energy minimizations were carried out by using constant pressure calculations. The computationally derived lattice parameters are a = b = 8.359 Å, and c = 24.854 Å giving c/a 2.973, i.e. with a slight distortion in the basic cubic lattice, as suggested by Somogyvari *et al*¹¹.

Lattice Energies (eV)		
Octahedral vacancies	Tetrahedral vacancies	Random distribution
-4801.45	-4773.96	-4785.91

Table 5.1: Lattice energies with vacancies on the octahedral, tetrahedral and random distribution.

5.2.1 Bonding in Maghemite

The calculated bond distribution in maghemite is displayed in **Table 5.2**, where the oxygen atom is fully coordinated to four metal cations, three in octahedral and one in tetrahedral coordination. There are three different types of tetrahedral and six different types of octahedral coordinations observed here. The calculations also show that it is easier to create a vacancy in the octahedral site rather than the tetrahedral site, **Table 5.1**, as octahedral sites are geometrically bigger and Fe-O bonding is weaker than in the tetrahedral sites. The cation vacancy distribution in the octahedral sites agrees with earlier report⁸. There is a strong correlation between the vacancy site and volume of the unit cell. The octahedral vacancies yield smaller unit cell volumes than

the tetrahedral vacancies, which is in agreement with Shmakov *et al*⁸, although some authors have reported that the vacancies could be found in both tetrahedral and octahedral sites.^{7, 12, 13} Amstrong *et al*¹² argued that there is a more co-valency observed in the tetrahedral sites, in agreement with our results which show a decrease in the cation-oxygen distance for the tetrahedral sites with respect to the octahedral sites.

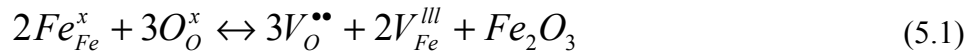
Sites	Bond distribution	Mean bond distance Å		
		This work	Experimental ⁸	Experimental ¹⁴
Tetrahedral (3 types of bond distribution)	1.84, 1.86, 1.94, 1.95	1.85 1.93	1.87	1.84
	1.84, 1.85, 1.91, 1.91			
	1.84, 1.85, 1.92, 1.97			
Octahedral (6 types of octahedral bond distribution)	1.94 (2), 2.004(2), 2.01 (2)	2.06 1.94	2.03, 2.20, 2.01	2.09
	1.898, 1.95, 1.998, 2.00, 2.07, 2.1			
	1.91,1.94, 1.95, 1.97, 2.06, 2.21			
	1.93,1.94, 1.94, 1.99, 2.01, 2.18			
	1.896,1.92, 1.97, 2.002, 2.04,2.14			
	1.898,1.95, 1.998, 2.00, 2.07, 2.16			

Table 5.2: Bond distribution of maghemite in different sites. The mean inter-atomic distance is compared with two experimental results.

5.2.2 Defect formation energies

Iron oxide materials are used as oxidation- reduction catalysts¹⁵. Previously Catlow and co-workers¹⁶ have suggested the most energetically favourable process for oxidation and reduction reactions for hematite by using computational methods. The authors have noted that usually, the reduction process occurs with the formation of electrons, charge compensated by either oxygen vacancies or cation interstitials while the oxidation reaction involves with the formation of electron holes with vacancy compensation or by creating oxygen interstitials¹⁶. Here the same procedure is applied to predict the preferential mechanism for the oxidation and reduction processes in the spinel iron oxide, maghemite.

To understand the defect mechanism in maghemite the defect formation energies are calculated, which are discussed in detail in Chapter 2. Schottky defects are created in a perfect crystal by transferring atoms from bulk lattice sites to the surface site in stoichiometric proportions and is represented by the equation,



When an ion is transferred from a lattice site to an interstitial site, a Frenkel defect is created and is represented by,

Anion Frenkel:



Cation Frenkel:



where O_O^x and Fe_{Fe}^x are neutral anion and cation sites, V_{Fe}^{III} , $V_O^{\bullet\bullet}$ are the metal and oxygen vacancies, $O_i^{\prime\prime}$ and $Fe_i^{\bullet\bullet\bullet}$ are oxygen and iron interstitials respectively. The

values are displayed in **Table 5.3** were calculated at infinite dilution using the Mott-Littleton method as implemented in the GULP package.

Defect	Defect Energy (eV)
V_{Fe}^{III}	55.42
$V_O^{\bullet\bullet}$	23.34
O_i^{II}	-12.84
$Fe_i^{\bullet\bullet\bullet}$	-30.09
Anion Frenkel	5.25
Cation Frenkel	12.67
Schottky	6.17

Table 5.3: The defect formation energy of maghemite.

The preferable mechanism of oxidation and reduction reactions are calculated by methods previously discussed by Catlow et al¹⁶ for hematite, for the oxidation reaction, charge compensation is either by oxygen interstitials or metal vacancies.

Formation of oxygen interstitials can be expressed as



where O_i^{II} and \dot{h} represent oxygen interstitial and electron hole respectively.

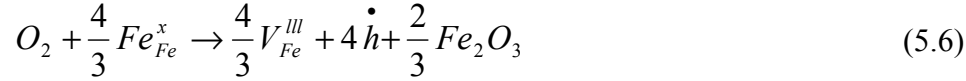
The oxidation energy can be calculated as follows:

$$E_{Ox}^{\ddot{O}_i} = E_D + 2E_{12} + 2E_{\ddot{O}_i} + 4E\dot{h} \quad (5.5)$$

where E_D is the dissociation energy of oxygen (7.1 eV) calculated from simulations, described in Chapter 3. E_{12} is the first and second electron affinity of oxygen (8.2 eV), $E_{\ddot{O}_i}$ and $E\dot{h}$ are the formation energies of oxygen interstitials and holes.

If the oxidation proceeds via creating metal vacancies, the oxidation energy of the vacancy compensation is calculated as follows:

For vacancy compensation,



where Fe_{Fe}^x is Fe in the lattice site.

$$E_{Ox}^{V_{Fe}^{III}} = E_D + 2E_{12} + \frac{4}{3} E_{V_{Fe}^{III}} + 4E_h + \frac{2}{3} E_L \quad (5.7)$$

where $E_{V_{Fe}^{III}}$ is the formation energy of metal vacancy and E_L is the lattice energy of maghemite (150.05 eV).

In order to find out which mechanism is favoured, simplifying by subtracting equation (5.5) – (5.7) and becomes,

$$\begin{aligned} E_{Ox}^{O_i} - E_{Ox}^{V_{Fe}^{III}} &= 2E_{O_i} - \frac{4}{3} E_{V_{Fe}^{III}} - \frac{3}{2} E_L \\ &= 2(-12.84) - \frac{4}{3}(55.42) - \frac{2}{3}(-150.05) \\ &= 0.46 \text{ eV.} \end{aligned} \quad (5.8)$$

The oxidation energy by oxygen interstitials needs 0.46 eV energy more than by vacancy compensation. The difference in energy implies that vacancy compensation is the favourable mechanism for the oxidation of maghemite, which is expected in view of the dominance of Schottky disorder.

For the reduction reaction the charge is compensated by either creating oxygen vacancies or cation interstitials.

For oxygen vacancies,



And the energy of reduction is given by,

$$E_{Red}^{V_O^{\bullet\bullet}} = 2E_{V_O^{\bullet\bullet}} + 4E_{e^-} - E_D - 2E_{12} \quad (5.10)$$

where $E_{V_O^{\bullet\bullet}}$ and E_{e^-} are the formation energies of oxygen vacancies and electrons respectively.

For cation interstitials,



And the reduction energy is given by,

$$E_{Red}^{Fe_i^{\bullet\bullet\bullet}} = \frac{4}{3}E_{Fe_i^{\bullet\bullet\bullet}} - E_D - 2E_{12} - \frac{2}{3}E_L + 4E_{e^-} \quad (5.12)$$

where $E_{Fe_i^{\bullet\bullet\bullet}}$ is the energy of formation of trivalent metal interstitials.

The above two equations (eqn (5.10) and eqn (5.12)) are simplified by subtracting,

$$E_{Red}^{V_O^{\bullet\bullet}} - E_{Red}^{Fe_i^{\bullet\bullet\bullet}} = 2E_{V_O^{\bullet\bullet}} - \frac{4}{3}E_{Fe_i^{\bullet\bullet\bullet}} + \frac{2}{3}E_L \quad (5.13)$$

$$\begin{aligned} &= 2(23.34) - \frac{4}{3}(-30.09) + \frac{2}{3}(-150.05) \\ &= -13.23 \text{ eV} \end{aligned}$$

The above results suggested that during the reduction process, oxygen vacancies are the dominant species by approximately 13eV than iron interstitials. Therefore, the reduction reaction is initiated by the creation of oxygen vacancies, which is the preferred mechanism for the reduction process in maghemite.

5.3 Incorporation of Isovalent Ions in Maghemite

The incorporation of impurities in the lattice of maghemite could influence the stability of the structure. In this study, the isovalent cations, Cr^{3+} , Al^{3+} and Mn^{3+} are considered as dopants. In order to find out the preferred sites, substitutions of Cr^{3+} , Al^{3+} and Mn^{3+} were made to replace both tetrahedral and octahedral Fe^{3+} sites. The solution energies of the different dopant oxides in the two cation sites are calculated using the two approaches, Mott-Littleton and Supercell calculations.

5.3.1 Solution Energy Calculations

The calculation of the structures and energies is carried out using the Mott-Littleton method (section 2.3.1). In this study, the radius of region 1 is taken as 12 Å, and thus the substitution energy of the isovalent impurity ion at the Fe^{3+} site at infinite dilution is calculated.

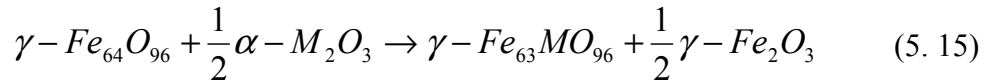
The solution energy E_s is :

$$E_s = [(E_{\gamma\text{-Fe}_2\text{O}_3} + E_{M^{3+}}) - \frac{1}{2} E_{M_2\text{O}_3}] \quad (5.14)$$

where $E_{M_2\text{O}_3}$ is the lattice energy of the dopant oxide, $E_{\gamma\text{-Fe}_2\text{O}_3}$ is the lattice energy of pure maghemite and $E_{M^{3+}}$ is the defect substitution energy, the energy required to move one Fe^{3+} from its lattice position to infinity and one impurity ion (M^{3+}) from infinity to the vacant cation site.

Supercell calculations are usually employed to simulate higher concentrations of defects. The interaction between dopant ions in neighboring cells is expected to be

small due to the size of the cell. The calculations use the γ -Fe₆₄O₉₆ 1x1x3 supercell with ordered vacancies where a single cation substitution is made first before the lattice energy minimization. By replacing a single Fe³⁺ in the supercell, 64 possible γ -MFe₆₃O₉₆ variants are created (20 with M in tetrahedral positions and 44 with M in octahedral positions). From the total lattice energy generated, the defect energy can be calculated by comparing the defect lattice with the perfect lattice, and the solution energy for the reaction,



The solution energy, E_s can be calculated using the relation,

$$E_s = (E_{\gamma\text{-MFe}_{63}\text{O}_{96}} - E_{\gamma\text{-Fe}_{64}\text{O}_{96}}) + \frac{1}{2}(E_{\gamma\text{-Fe}_2\text{O}_3} - E_{\text{M}_2\text{O}_3}) \quad (5.16)$$

For substitution in the tetrahedral sites, a correction factor is added to the calculated solution energy. This correction term arose due to the d-shell degeneracy and was calculated from the difference in the crystal field stabilization energies (CFSE) of the octahedral and tetrahedral sites. The octahedral site preferential energy (OSPE) for Cr³⁺ and Mn³⁺ are -1.63 eV and -0.99 eV respectively^{17, 18}, while Fe³⁺ and Al³⁺ have no stabilization energies.

Dopants	Radius (Å) (Fe ³⁺ : 0.645)	Solution Energy (eV)			
		Mott - Littleton		Supercell Method	
		Octa	Tetra	Octa	Tetra
Al ³⁺	0.535	0.17	0.62	0.19	0.57
Cr ³⁺	0.615	0.18	2.22	0.11	2.22
Mn ³⁺	0.645	0.17	1.27	0.15	1.27

Table 5.4: The solution energies are calculated using two different methods.

The results obtained using the two methods are consistent (**Table 5.4**) and suggest that substitution at the octahedral sites is energetically more favourable than the tetrahedral sites. For Cr³⁺ and Mn³⁺, substitution at the octahedral sites is energetically less unfavourable than in the tetrahedral sites because of the much lower solution energy for that site. The octahedral sites corresponds to the type of geometry required for these dopant's radii (**Table 5.4**), whereas substitution of Mn³⁺ or Cr³⁺ in a tetrahedral iron site requires respectively 1 eV and 2eV more energy than replacing a Fe³⁺ octahedral site. However, for Al³⁺ the energy difference is only 0.4 eV, suggesting that Al³⁺ could occur in both tetrahedral and octahedral sites. The concentration used here is very low (1.6%). Gillot *et al*¹⁹ from infrared investigations, reported that in highly substituted Cr-maghemites, some of the cation vacancies are considered to enter the tetrahedral sites as well as octahedral sites. On the other hand Al induced vacancies were reported to occur in the octahedral cation sites indicating that Al has entered tetrahedral sites. In this study, which considers the dilute case, only one out of 64 Fe³⁺ is replaced by a dopant (Al³⁺, Cr³⁺ or Mn³⁺), which prefers to occupy the octahedral site, and the vacancies are kept in the same sites. However, Wolska *et al*^{20,21} investigated the effects of Al³⁺ ions and revealed that the presence of Al³⁺ terminates the cation vacancy ordering in the octahedral sites by creating a partial occupancy of tetrahedral positions in the spinel lattice. The authors reported

that there is a possibility of these cations entering into both sites at higher concentration, which can be explained by the small difference in solution energies between the octahedral and tetrahedral sites of the Al doped system (see **Table 5.4**).

There is another possibility for the doping reaction where the end product would be hematite instead of maghemite, based on the fact that the formation of the α -phase is thermodynamically more favourable than the γ - phase. The solution energies for the reaction (Eqn 5.2, where the end product is hematite instead of maghemite) are calculated, considering the dopants are in the octahedral positions, which are very low (Al^{3+} : 0.03 eV, Cr^{3+} : -0.05 eV and Mn^{3+} : -0.01 eV). The energy difference between the two scenarios is 0.16 eV (1.6% dopant concentration), indicating that if hematite is the end product, then the solubility of the mixed material is high.

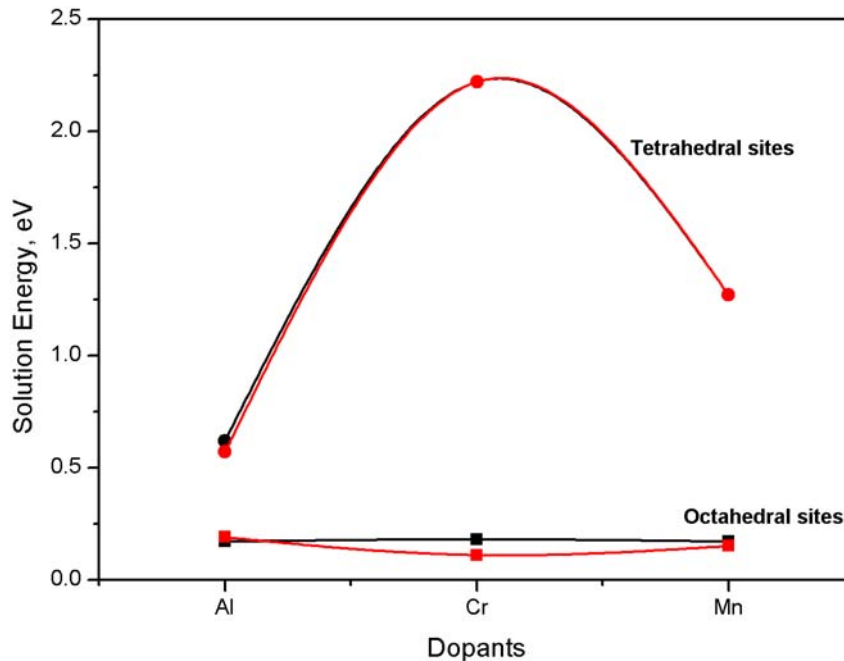


Figure 5.1: Graphical representation of solution energies calculated using two different methods, Mott-Littleton (black coloured) and supercell calculations (red coloured).

5.3.2 Bond distribution of the dopants in Maghemite

In the lowest energy structures, Cr^{3+} and Mn^{3+} are bonded to six fully coordinated oxygen ions while Al^{3+} is bonded with four fully coordinated O anions and two partially coordinated O anions. Al^{3+} replaces the Fe^{3+} , with the smallest inter-atomic Fe-O distance, while Cr^{3+} and Mn^{3+} replace the Fe^{3+} with the same co-ordination as in the pure structure. The difference in bond lengths before and after doping is summarized in **Table 5.5**. Al-O distances are smaller than the other cation–anion distances, and the volume decrease in Al-doped systems can be explained by these shorter Al-O bond lengths compared to the Fe-O distances.

Properties	Maghemite (1x1x3) (γ -Fe ₆₄ O ₉₆)		Cr doping		Mn doping		Al doping			
			Octa	Tetra	Octa	Tetra	Octa		Tetra	
Lattice Energy (eV)	-4801.45		-4803.46	-4802.98	-4801.92	-4801.79	-4806.73		-4806.35	
Lattice Parameter (Å)										
a	8.36		8.36	8.36	8.36	8.36	8.35		8.36	
b	8.36		8.36	8.36	8.36	8.36	8.34		8.34	
c	24.89		24.89	24.88	24.89	24.89	24.89		24.86	
α	90		90	90	90	90	90		90	
β	90		90	90	90	90	90		90	
γ	90		90	90	90	90	90		90	
Cell Volume (Å ³)	1739.68		1738.69	1739.01	1739.58	1739.67	1734.55		1733.86	
Static Dielectric constant	7.82		7.8	7.85	7.8	7.83	7.81		7.8	
Bond-lengths M-O	Octa	Tetra					Al-O	Fe-O	Al-O	Fe-O
	1.94	1.84					1.81	1.89	1.74	1.84
	(2)	1.85					1.83	1.92	1.74	1.85
	2.00	1.92					1.88	1.97	1.79	1.91
	(2)	1.97					1.90	2.00	1.80	1.91
2.01		1.94	2.04							
(2)		2.07	2.17							

Table 5.5: Comparison of doping with transition metal dopants Cr³⁺, Mn³⁺ and Al³⁺. Cr³⁺ and Mn³⁺ replace the Fe³⁺ with the same bond-distribution (green coloured) and Al³⁺ replaces the Fe³⁺ with the smallest bond length distribution (red coloured).

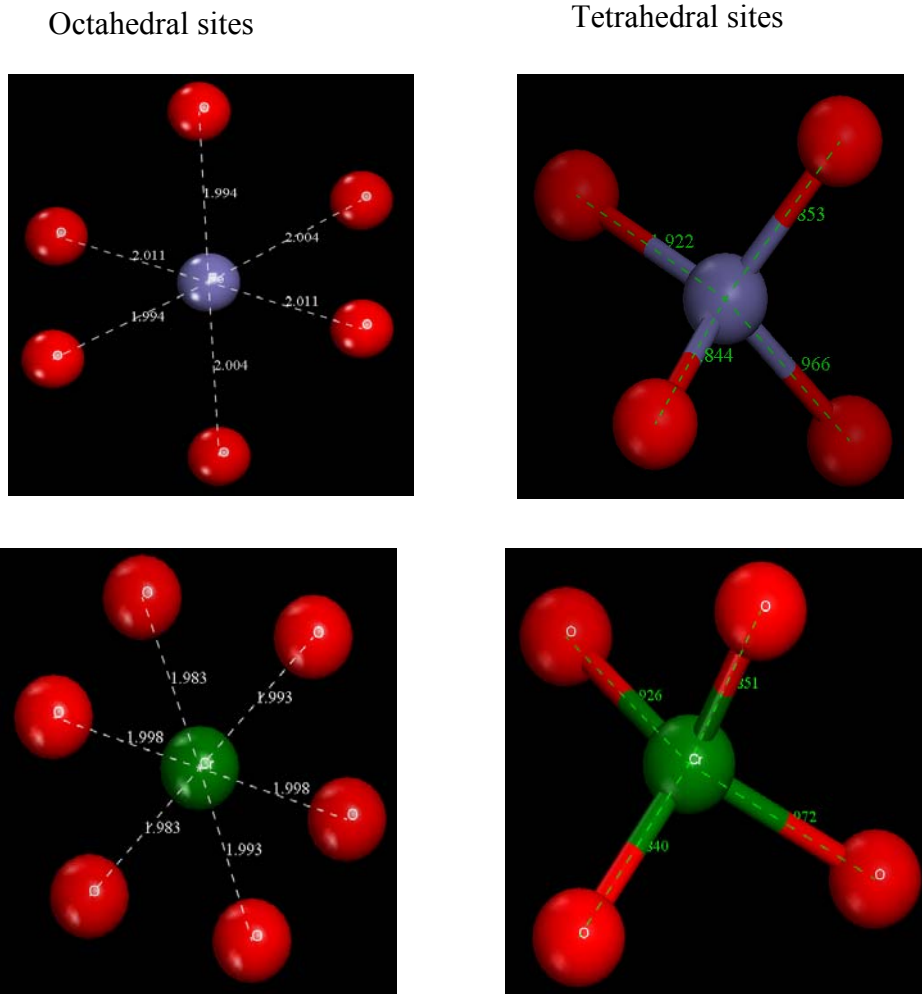


Figure 5.2: The Fe-O and Cr-O bond distances in the octahedral and tetrahedral sites of Maghemite. The blue spheres represent Fe ions, green spheres Cr ions and red spheres oxygen ions.

5.4 Cation Ordering and Stability of the Dopant Systems

5.4.1 Configurational Effects

The energies and equilibrium geometries of all possible configurations of the mixed solution systems at low concentration were calculated as explained in the Methodology chapter. The cation ordering disappears when a dopant is introduced into the pure maghemite system. The number of different configurations generated is displayed in **Table 5.6**.

$N_{\text{dopant}} / N_{\text{sites}}$	x	Total number of configurations, N	Inequivalent configurations, M	Total number of configurations, $N_{\text{Octa sites}}$	Inequivalent configurations, M_{Octa}
0	0.000	1	1	1	1
1/64	0.016	64	9	40	5
2/64	0.031	2016	273	780	110
3/64	0.047	41664	5239	9880	1235
4/64	0.063	635376	79766	91390	11545

Table 5.6: Total number (N) of configurations with N_{dopant} substitutions in the maghemite $1 \times 1 \times 3$ supercell with a total of 64 cation sites, in which 40 cations are in the octahedral sites ($N_{\text{Octa sites}}$). M is the number of inequivalent configurations in each case.

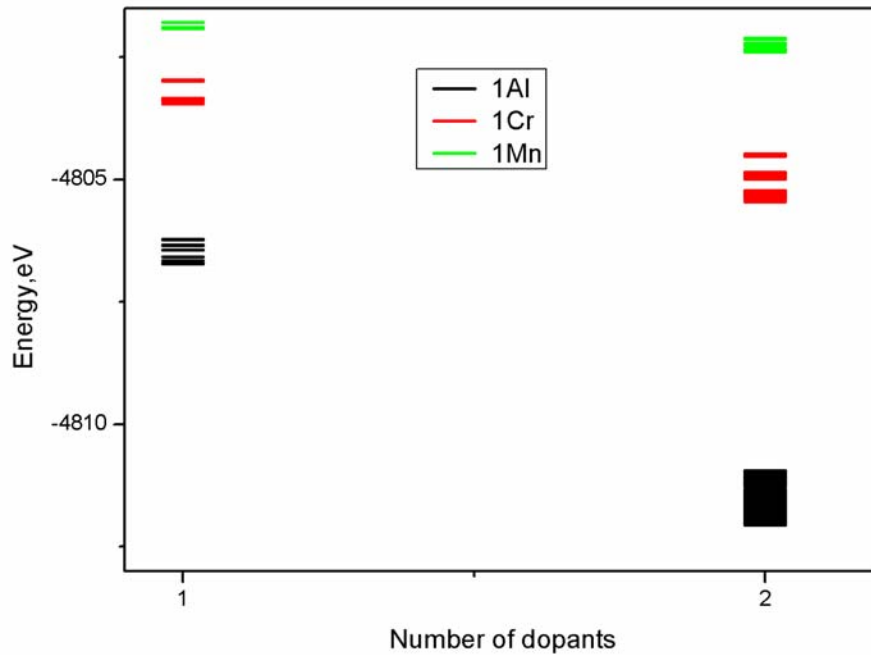


Figure 5.3: Correlation between the energy and number of dopants in the cell. The energies of different configurations are very similar.

Of all the different configurations, for example a total number of 40 configurations generated by the substitution of one dopant in the octahedral sites, **Table 5.6**. The energies of the different configurations of dopant systems are close (0.1 eV for Cr^{3+} , 0.03 eV for Mn^{3+}) and consequently disorder can be expected in the solution (**Figure 5.3**).

Comparison of the configurational entropies (**Figure 5.4**) show that of the three dopants, the $\gamma\text{-FeAlO}_3$ solution is less ordered than the other doped systems at 0 K. For Al^{3+} , the energy difference between the octahedral site and tetrahedral site is 0.39 eV. For the Cr^{3+} and Mn^{3+} substituted system, this small energy difference is attributed to the preferential occupation of these ions into the octahedral sites, which might result in a disorder by entering some of the vacancies to the tetrahedral sites as previously reported by Gillot *et al*¹⁹. With $\gamma\text{-FeMnO}_3$ and $\gamma\text{-FeCrO}_3$ doped systems showing a greater extent of disordering at high temperatures. (**Figure 5.4**). On the other hand in the $\gamma\text{-FeAlO}_3$ system, the disordering can be attributed to the much smaller size of Al^{3+} compared to other dopant ions. Previous studies²² demonstrated

that vibrational effects have little impact on these types of systems, with magnetic interactions playing a more important role. Generally the presence of a non-magnetic ion will weaken the overall magnetic exchange interactions. As the temperature and concentration increases, the degree of disordering in mixed Al solutions increases less than the other dopant systems. The lowering of the order-disorder temperature for Al^{3+} compared to the other dopants can be explained by the weak magnetic nature of aluminium.

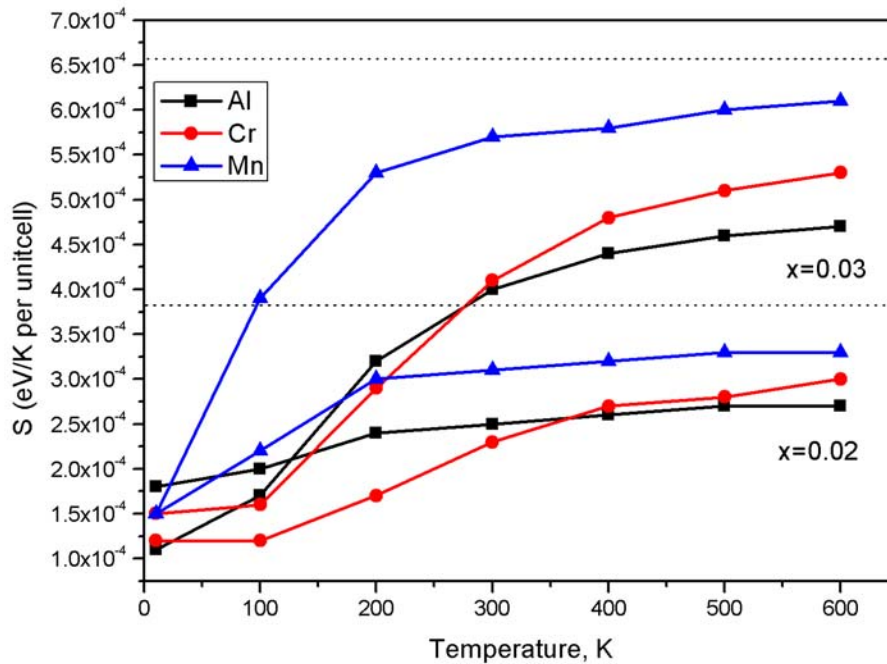


Figure 5.4: Configurational entropy as a function of temperature. Dotted lines represent the maximum entropies obtainable at each composition.

From our previous work²³ it is expected that the inclusion of magnetic contributions will increase the enthalpy of mixing of the solid solution with respect to the non-magnetic system. However, in this study magnetic contributions are not taken into account, as the magnetic nature of maghemite is complex and it is not straight forward to include these effects in our simple model.

In order to compare the stability of a solid solution system with that of the separated components, the enthalpies and free energies of mixing for a number of temperatures are computed. The thermodynamic stability of the solution is given by the free energy of mixing (see **Figure 5.5**), which indicates that the solution is stable above 340 K in the Cr-maghemite system, whereas for Al^{3+} and Mn^{3+} solutions, the solid solution exists above 200K.

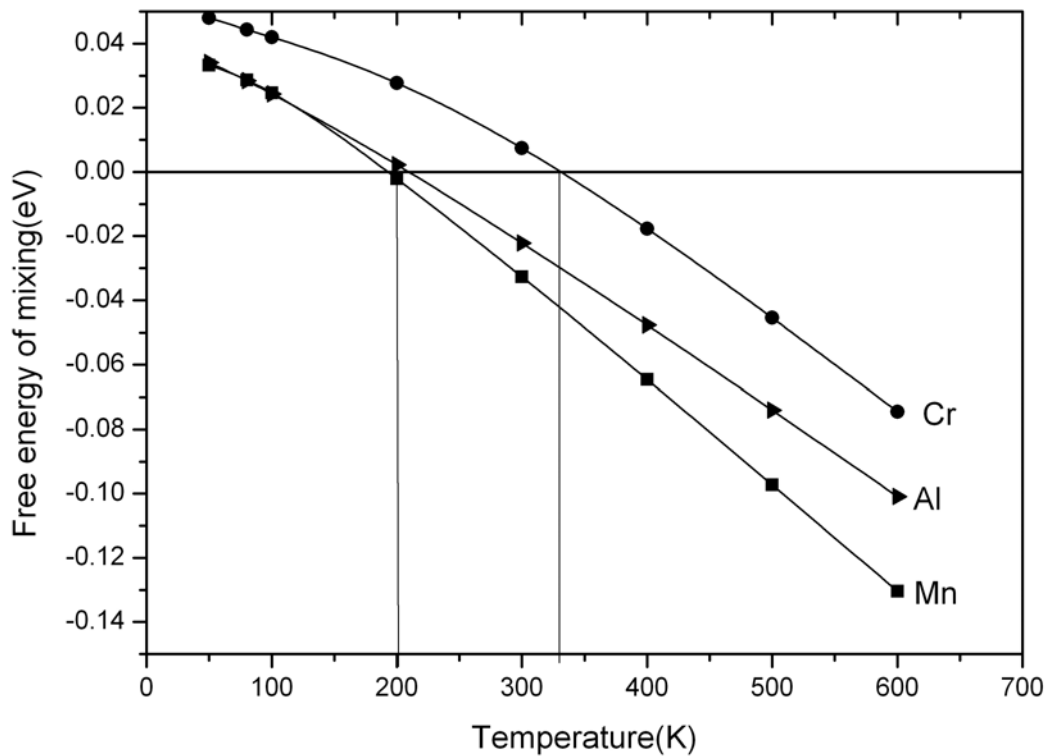


Figure 5.5: The free energy of mixing of the system as a function of temperature.

5.4.2 Effect of Dopants on the γ - to α - Phase Transition

The phase transition from α to γ is very unlikely as the α -phase has a higher thermal stability than the γ -phase. The conversion of the γ - to the α - phase is reported to occur between 625-675 K^{20, 24-27}. Impurities retard the formation of the α -phase, stabilizing the defect spinel phase at higher temperatures, which is very important in certain catalytical applications, for example, for the WGS reaction³, or aldol condensation

reaction. We have therefore investigated the effect of dopants on the thermal stability of $\gamma\text{-Fe}_2\text{O}_3$.

It has been proposed that the change in the phase transition temperature upon doping is directly proportional to the difference in solution enthalpies of the two phases and inversely proportional to the difference in the internal enthalpy of the pure phases²⁸. Due to the equivalent co-ordination of ions in the pure and doped system, the entropy change at the transition point is considered to be small. The change in the transition temperature upon doping can be calculated as,

$$\delta T_c = T_c^0 \frac{\Delta(\delta H)}{\Delta H^0} \quad (5.17)$$

where δH is the difference in the enthalpies of the doped and pure systems, ΔH^0 is the enthalpy change for the pure phases, i.e, hematite and maghemite and T_c^0 is the critical transition temperature, 675K (400°C)^{20, 24-27}.

The formation of the α - phase from the γ - phase requires the conversion of all tetrahedral Fe sites to octahedral coordination. This process has some activation energy and at 675K, the system attains sufficient energy to overcome this activation energy. Using the above relationship (Eqn.5.17), it is possible to calculate the transition temperature of the doped system (at low concentration of dopants (1.6%)) and thus assess the effect of dopants on the thermal stability of $\gamma\text{-Fe}_2\text{O}_3$. The data in **Table 5.7** show that introducing dopants stabilizes the α - lattice, probably by increasing the activation energy. However, the computational method only allows the calculation of the thermodynamic effect, while any kinetic effects are unknown.

Dopants	Change in transition temperature (calculated) K	Transition temperature, K (Critical transition temperature is 675K)	Solution range, K
Al	300	975	200-975
Cr	282	957	340-957
Mn	275	950	200-950

Table 5.7: The transition temperature of each dopant and the range of temperatures at which the mixed solution system can exist are tabulated.

The current studies reflect the thermodynamic effect of dopants on the γ -to α - phase transition, which show that the presence of these dopants should increase the γ - to α - phase transition temperature. For the mixed solutions, Al^{3+} in particular helps to maintain the maghemite phase to a higher temperature than the other dopants. The critical transition temperature increases from 675K by 300K to 975K, which is in agreement with findings by De-Boer and Dekkers²⁹. For Cr^{3+} and Mn^{3+} , the increase in transition temperature is 282 K and 275 K respectively, see **Table 5.7**. Furthermore, from the solution free energies we can therefore conclude that the Al^{3+} -doped solution system can exist between 200 -975 K, while for the Mn^{3+} doped system, the range is 200 - 950 K and for Cr^{3+} , the mixed solution exists between 340 - 957 K (**Figure 5.5, Table 5.7**). Sidhu *et al*³⁰ described the effect of Cr^{3+} , Mn^{3+} and Al^{3+} on the transformation of maghemite to hematite. The authors argued that an additional activation energy is needed to redistribute these elements in hematite, which decreases the transformation rate. Oliveira *et al*³¹ using thermal analysis studies, showed that the presence of Mn in the maghemite structure delays the transition to hematite, preventing the regeneration of the α -phase, which is a crucial step in certain catalytical reactions, such as aldol and retro-aldol condensation of acetone³². The active site in this reaction is the surface hydroxyl groups and the

authors found that the catalytic activity of maghemite is higher than that of hematite due to the greater acidic nature of the surface hydroxyl groups.

5.5 Conclusions

In this study, atomistic simulation techniques have been used to elucidate the effect of isovalent dopants in maghemite. Despite the wide application of maghemite, questions remain on the energetics and influence of foreign ions on the γ - to α - phase transition and the thermal stability of the doped systems. In maghemite, the cation vacancies are located exclusively on the octahedral sites. Introducing a dopant into the system stabilizes the maghemite structure with respect to hematite, where the dopants (Al^{3+} , Mn^{3+} and Cr^{3+}) show similar solution energies and prefer to occupy the octahedral sites. However, the small energy difference between the tetrahedral and octahedral sites in Al^{3+} indicates the tendency of these ions to occupy both sites. The Al^{3+} -doped system has the most disorder at low temperature, while the Mn^{3+} -doped system shows the most extensive disorder at high temperatures. The size difference between Fe^{3+} and Al^{3+} is assumed to play a part in decreasing the disorder at higher temperatures. The addition of dopants improves the thermal stability of maghemite and increases the γ - to α - transition temperature. Al^{3+} stabilizes the γ - phase most compared to the other dopants, forming stable mixed solutions in the range of 200-975 K.

Considering this study on maghemite as a stepping-stone to the complex spinel material magnetite, in the next chapter the results of defect calculations on both the bulk and the (110) surface of magnetite are presented.

5.6 References

1. A. H. Morrish; K. Haneda, *Journal of Magnetism and Magnetic materials*, **1980**, 15-18, 1089.
2. E. Matijević; M. Borkovec, *Surface and Colloid Science*, New York, **2004**.
3. A. Basinska; L. Kepinski; F. Domka, *Applied Catalysis A: General* **1999**, 183, (1), 143-153.
4. D. E. Miser; E.-J. Shin; M. R. Hajaligol; F. Rasouli, *Applied Catalysis A: General* **2004**, 258, (1), 7-16.
5. D. Li; W. Y. Teoh; S. Cordelia; W. Robert; A. Rose; R. Bettina, *Chemistry of Materials* **2006**, 18, 6403-6413.
6. G.W. Van Oosterhout; C. J. M. Rooijans, *Nature* **181** **1958**, 44.
7. K. Haneda; A. H. Morrish, *Solid State Communications*, **1977**, 22, 779.
8. N. Shmakov; G.N. Kryukova; S.V. Tsibula; A.I. Chuvilin; L. P. Solovyeva, *J. Applied Crystallography*, **1995**, 141, (28).
9. E. Schmidbauer; R. Keller, *Journal of Magnetism and Magnetic materials*, **1996**, 152, 99.
10. G. M. da Costa; E. De Grave; R. E. Vandenberghe; P. M. A. De Bakker, *Clays and Clay Minerals* **1994**, 42, (5), 628.
11. Z. Somogyváari; E. Sváb; G. Mészáros; K. Krezhov; I. Nedkov; I. Sajó; F. Bourée, *Applied Physics A: Materials Science & Processing* **2002**, 74, (0), s1077-s1079.
12. J.R. Armstrong; A. H. Morrish; G. A. Sawatzky, *Physics Letters*, **1966**, 23, 414.
13. H. Annersten; S. S. Hafner, *Zeitschrift. fur Kristallographie*, **1973**, 137, 321.
14. J.-E. Jørgensen; L. Mosegaard; L. E. Thomsen; T. R. Jensen; J. C. Hanson, *Journal of Solid State Chemistry*, **2007**, 180, (1), 180-185.
15. R. M. Cornell; U.Schwertmann, *The Iron Oxides Structure, Properties, Reactions, Occurrence and Uses*. 1996.
16. C. R. A. Catlow; J. Corish; J. Hennessy; W. C. Mackrodt, *Journal of the American Ceramic Society*, **1988**, 71, 42-49.
17. J. D. Dunitz; L. E. Orgel, *Journal of Physics and Chemistry of Solids* **1957**, 3, (3-4), 318-323.

18. D. S. McClure, *Journal of Physics and Chemistry of Solids* **1957**, 3, (3-4), 311-317.
19. F. B. B.Gillot, J.F. Ferriot, F.Chassagneux and A Rousset, *Journal of Solid State Chemistry*, **1977**, 21, 375.
20. E.Wolska; W.szajd; P.Piszora, *Soild State ionics* **1994**, 70/71, 537-541.
21. E. Wolska; U. Schwertmann, *Solid State Ionics* 32-33, (Part 1), 214-218.
22. G. M. da Costa; E. De Grave; R. E. Vandenberghe, *Hyperfine Interactions* **1998**, 117, 207.
23. S. Benny; R. Grau-Crespo; N. H. de. Leeuw, *Physical Chemistry Chemical Physics*, **2008**, 11, 808.
24. M.R.Anantharaman; K.Seshan; S.N.Shringi; H.V.Keer, *Bulletin of Material Science*, **1984**, 6, (1), 59.
25. Xisheng Ye; Dongsheng Liny; Z. Jiaoz; L. Zhangx, *Journal of Physics. D: Applied Physics*, **1998**, 31.
26. D. E. Miser; E.-J. Shin; M. R. Hajaligol; F. Rasouli, *Applied Catalysis A: General* **2004**, 258, 7.
27. D.L.A. de Faria; S.V.Silva; M. T. de Oliveira, *Journal of Raman Spectroscopy* **1997**, 28, 873-878.
28. M. Netsianda; P. E. Ngoepe; C. R. A. Catlow; S. M. Woodley, *Chemistry of Materials*, **2008**, 20, 1764.
29. C. B. de Boer; M. J. Dekkers, *Geophysical Research Letters* **1996**, 23, (20), 2815.
30. P.S.Sidhu, *Clays and Clay Minerals* **1988**, 36, (1), 31.
31. L. C. A. Oliveira; J. D. Fabris; R. R. V. A. Rios; W. N. Mussel; R. M. Lago, *Applied Catalysis A: General* **2004**, 259, (2), 253-259.
32. H. Watanabe; J. Seto, *Bulletin of Chemical Society of Japan*, **1991**, 64, 2411-2415.

Chapter 6

Magnetite: Defect Calculations in the Bulk and at the Surface

6.1 Introduction

Magnetite (Fe_3O_4) is considered to be the active phase in the WGS reaction.² This chapter presents detailed information on the bulk and surface structure of magnetite above 120K. The influence of defects such as Al^{3+} , Cr^{3+} , Mn^{3+} and Mn^{2+} is investigated.

6.2 Cation Charge Distribution

Magnetite (Fe_3O_4) has an inverse spinel structure, AB_2O_4 as discussed in Chapter 1. The starting point of this work is the structure reported by Wright *et al*³. The distribution of cations in terms of oxidation state and oxygen coordination depends on many factors such as crystal field stabilization energy, pressure, temperature and preparation method⁵. An electron hopping mechanism has been suggested above 120 K, the Verwey temperature. This study is only concerned with the high temperature phase - electron hopping occurs between the Fe^{2+} and Fe^{3+} ions in the octahedral B sites, resulting in an average charge of $\text{Fe}^{2.5+}$, whereas in the tetrahedral B sites, all ions remain in the 3+ oxidation state⁶.

The mean field approach⁷ is employed to model this complex system (see Chapter 2). For the pure system, the charge and the potentials are distributed equally over the octahedral sites in order to maintain the average charge of 2.5. The potentials of the ions are scaled according to their site occupancies. The Fe^{3+} and Fe^{2+} ions are each given half occupancies in the octahedral sites before optimization of the whole structure, where the average charge of each ion in the octahedral site must remain +2.5. Additionally, when a defect is introduced into the structure, to maintain the overall average charge, the defect is given its full charge (eg. +3 or +2) and the remaining partial charge is distributed equally over all other Fe cations in the octahedral sites. For example in a $\text{Fe}_{24}\text{O}_{32}$ cell, when a trivalent dopant is introduced into the octahedral site, the dopant charge remains +3 and the other charges in the octahedral sites are averaged to +2.4667. The potentials are scaled to compensate for the charges of the ions.

6.3 Calculations of Pure Magnetite

6.3.1 Bulk Calculations

The structure and properties of magnetite are explained in detail in Chapter 1. The unit cell of magnetite contains 32 oxygen anion sites and 24 cation sites. At room temperature, ie, above the Verwey temperature, the octahedral sites are occupied by 16 $\text{Fe}^{2.5+}$ ions, whereas the tetrahedral sites are occupied by 8 Fe^{3+} ions³. The bond distances of $\text{Fe}_{\text{tetra}}\text{-O}$ is 1.889 Å and $\text{Fe}_{\text{octa}}\text{-O}$ is 2.058Å³, which is in good agreement with our calculations. The model discussed in section 6.2 is verified here by comparing the calculated lattice properties using the GULP simulation code with the experimental values. The results in **Table 6.1** show that the model employing only a potential derived for octahedral Fe ions defines the system more accurately in terms of lattice parameter and bond distances than a model using different potentials for the octahedral and tetrahedral cations, although the differences are not large.

Properties	Model using octahedral Fe^{3+} Potentials	Experiment (Wright <i>et al</i> ³ , 2002)	Model including tetrahedral Fe^{3+} Potentials ¹
Static Dielectric constant	8.2	10 (Schelegel <i>et al</i> ⁴)	8.3
Lattice parameter, Å	8.377	8.394	8.284
Bond distance, Å	1.898 2.047	1.889 2.058	1.847 2.041

Table 6.1: Comparison of the magnetite models used in this study with experimental results.

6.3.2 (110) Surface of Magnetite

To study the surface properties of magnetite, the low index non-dipolar (110) surface has been created using the simulation code METADISE. The (110) surface is one of the predominant growth planes and it is the most stable low index surface in magnetite.^{8,9} The surface model is created by employing the two-region strategy, (discussed in detail in Chapter 2) where region 1 has a thickness of 12 Å and region 2 extends down to a total of approximately 100 Å. Two possible terminations have been found for the (110) surface of magnetite; one surface is terminated with one tetrahedral Fe³⁺ ion on the surface and the other has two octahedral Fe^{2.5+} ions on the surface. The surface with the tetrahedral Fe termination ($\gamma = 2.1 \text{ J/m}^2$) has been shown to be energetically more stable than that with two octahedral Fe^{2.5+} ions ($\gamma = 4.1 \text{ J/m}^2$).

The calculated surface structure of the stable surface (lowest energy structure) is shown in **Figure 6.1**. A noticeable change at the surface occurs on relaxation (**Figure 6.1a**). Before relaxation, the top ferric (3+) ion and oxygen ions are in two-fold coordination while the Fe^{2.5+} ions are five-fold coordinated. During the energy minimization, the surface tetrahedral Fe³⁺ ion moves slightly downwards and becomes 3 coordinated (**Figure 6.1c**). The distance between the Fe and a surface O before minimisation is 3.49 Å (**Figure 6.1 b**), which shortens to 1.87 Å after relaxation. The octahedral Fe^{2.5+} ion near the surface moves slightly upwards (**Figure 6.1c**) by disconnecting from an oxygen ion and becoming four-coordinated. The loss of bonding in the surface compared to the bulk, and the electrostatic forces acting in the surface cause the rearrangement of the surface. The ferric ions are attracted towards the surface oxygen ions, resulting in the bond formation between the tetrahedral Fe³⁺ and O²⁻ ion. Due to this accumulation of positive charge near the surface, repulsive electrostatic forces act on the neighbouring Fe^{2.5+} pushing it away from the Fe³⁺. The distance between the neighbouring cations increases from 2.76 Å to 3.63 Å after relaxation. Therefore the stable surface is terminated with both tetrahedrally and octahedrally coordinated Fe ions, which is in agreement with experimental results¹⁰.

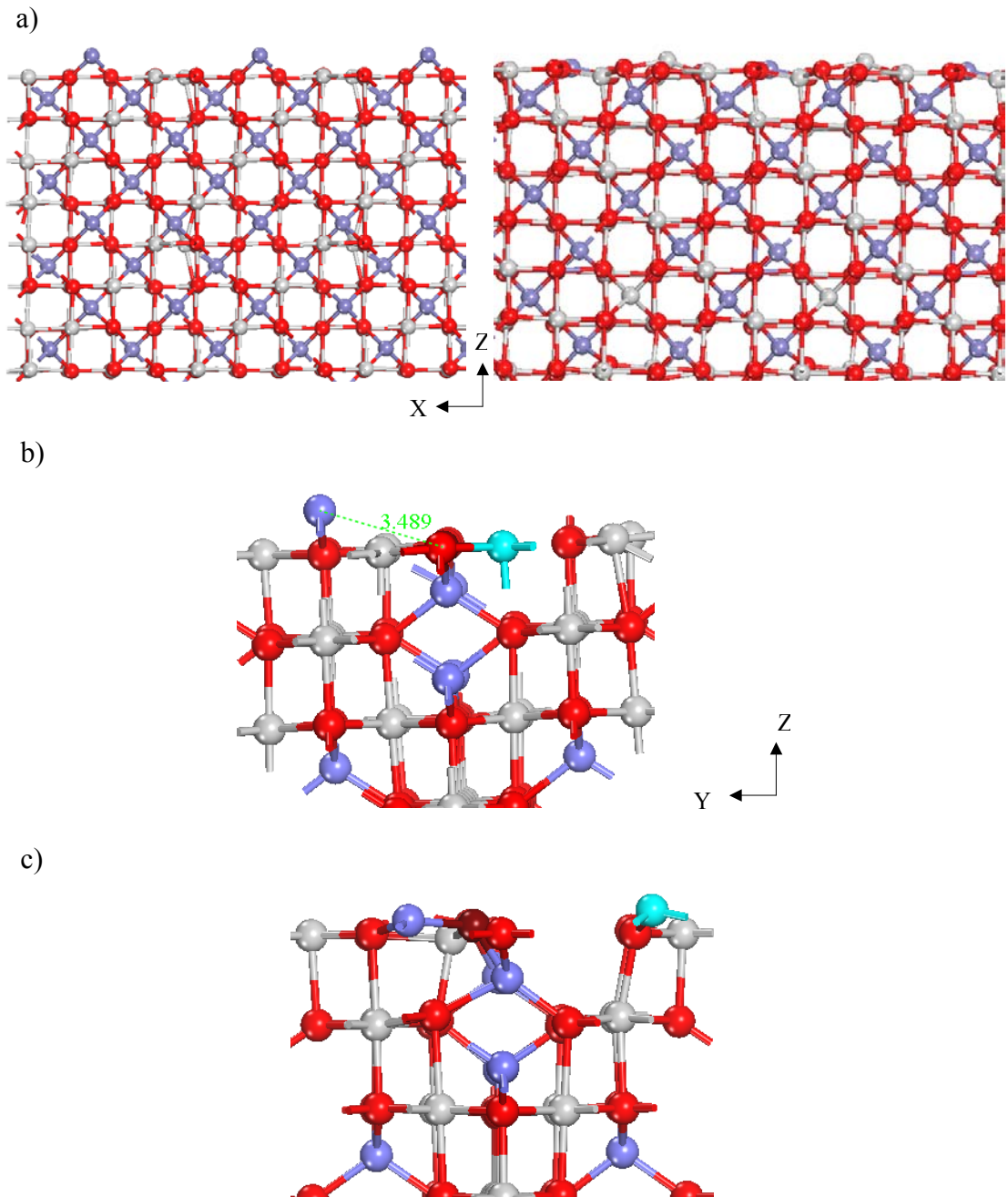


Figure 6.1: The (110) surface structure of magnetite (lower energy), a) left: before optimization and right: after optimization. b) Structural detail before relaxation and c) the re-arranged surface after relaxation. (Blue spheres represent Fe^{3+} ions, white spheres $\text{Fe}^{2.5+}$, red spheres O^{2-} ions, cyan sphere is the shifted $\text{Fe}^{2.5+}$ ion and the dark red sphere the shifted O^{2-} ion.)

6.4 Doped Magnetite : Bulk Calculations

6.4.1 Lattice Energy Calculations

Doping the spinel lattice with metal ions, for example aluminium, chromium or manganese, could strongly modify the redox properties of magnetite and thereby affect the catalytic properties. Additionally, these ions can influence the stability of the material as we have seen in Chapter 5 for maghemite. The Cr^{3+} , Al^{3+} and Mn ions (divalent and trivalent) are considered as dopants, based on the results obtained from our previous calculations on hematite and maghemite. Cr^{2+} has not been considered since it is more difficult to reduce Cr^{3+} than Fe^{3+} , unlike Mn^{3+} , which is easier. The substitutions have been made at both octahedral and tetrahedral sites using the supercell approach and the calculated lattice properties of the system doped with one impurity ion per unit cell are tabulated in **Table 6.2**. In all cases, the results show an energetic preference for octahedral substitution for the trivalent ions considered here.

Trivalent Metal Oxides	Lattice Energy (eV)	Lattice Parameter (Å)	Volume (Å ³)	Bond-distance (Å)
Magnetite	-1499.64	8.377	587.83	1.898 [Fe _t -O] 2.047 [Fe _o -O]
Al – Magnetite Octa	-1506.09	8.350	582.39	1.894 [Al-O] 2.028-2.069 [Fe _o -O] 2.067 [Fe _t -O]
Tetra	-1504.32	8.350	582.76	1.79 [Al-O] 2.045 [Fe _o -O] 1.903 [Fe _t -O]
Cr – Magnetite Octa	-1502.84	8.374	587.27	1.982 [Cr-O] 2.036 - 2.075 [Fe _o -O] 1.891 , 1.916 [Fe _t -O]
Tetra	-1501.12	8.375	587.38	1.895 [Cr-O] 2.047 [Fe _o -O] 1.897 [Fe _t -O]
Mn – Magnetite Octa	-1501.32	8.374	587.27	1.992 [Mn-O] 2.049 [Fe _o -O] 1.892 [Fe _t -O]
Tetra	-1499.96	8.377	587.84	1.9 [Mn-O] 2.047 [Fe _o -O] 1.898 [Fe _t -O]

Table 6.2: The substitution of dopants into the lattice of magnetite. Only one substitution is made (4%).

6.4.2 Effect of Dopants on Bulk Structures

Cr doping

Due to the presence of different lattice sites, the defect can have different positions. The calculations are restricted by the generation of large numbers of inequivalent configurations, listed in **Table 6.3** and energy minimizations are carried out using up to 4 dopants per simulation cell (12%).

No. of dopants	No. of different configurations (octahedral sites only)
1	16
2	120
3	560
4	1820

Table 6.3: Number of configurations generated with the increase in number of dopants

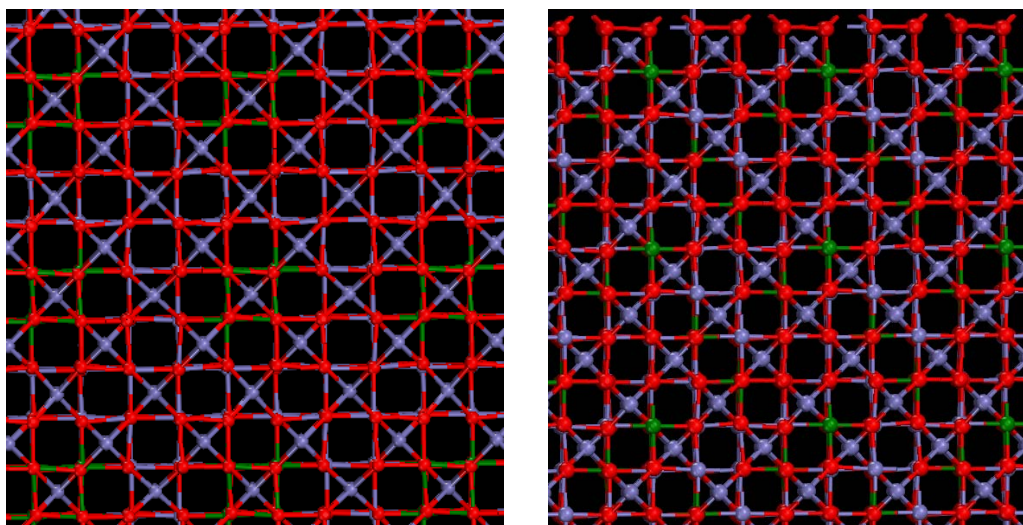


Figure 6.2: Distribution of Cr^{3+} in the high (left) and low (right) energy structures. (Blue spheres represent Fe ions, green spheres represent Cr ions and red spheres represent O ions.)

Cr^{3+} occupies octahedral sites, as is expected from the much lower energy for the octahedral site in **Table 6.2**. However, some authors¹¹ have reported that at high Cr contents, Cr can replace Fe in the tetrahedral sites in the crystalline structure. In the lower energy structures Cr^{3+} ions are scattered throughout the lattice whereas they cluster in the high-energy structures, **Figure 6.2** however, the difference in energy between solution and segregation energy is only 0.02 eV/dopant for 4% of impurities. As the concentration increases, the energy difference between the dispersed or clustered configurations increases gradually. For example, when the concentration increases to 8% (2 Cr/cell), the energy difference is 0.12 eV/cell, i.e. 0.06 eV/dopant and when the concentration is 12% (3 Cr/cell), the energy difference is 0.24eV/cell, i.e. 0.08eV/dopant, indicating that these ions prefer to go into a dispersed solution rather than a segregated configuration.

Al doping

To validate the structure, and the charge protocol and meanfield method used for this study, the elastic constants of a mixed system are calculated and compared with experimental and other theoretical results (tabulated in **Table 6.4**). According to the crystal field theory, the octahedral site preference energy of Al^{3+} is zero, as explained in Chapter 5; consequently aluminium could enter both octahedral and tetrahedral sites. However, the energy calculations indicate that at low concentration aluminium replaces the octahedral Fe^{3+} ions, which is in agreement with experimental results¹². Antonov *et al*¹³ studied the electronic structure of Al-substituted magnetite using magneto-optical spectroscopy and reported that at high concentration Al can substitute Fe^{3+} ions in both octahedral and tetrahedral sites.

<i>Elastic Constant</i>	<i>Experiment</i>	<i>Calculated</i>	<i>This work</i>
C11	26.6	35.1	32.9
C12	18.2	17.9	17.9
C44	18.2	16.5	15.3

Table 6.4: Experimental and calculated¹ elastic constants (10^{11} dyne cm^{-2}) for FeAl_2O_4

The experimental behaviour of aluminium as a dopant is entirely different from that of chromium. Fe-Al solutions exhibit a weak exsolution as they form as a cluster or a segregated phase¹⁴. It is reported that the exsolution of aluminium takes place between 600-700°C for a spinel containing 10-20 % of FeAl_2O_4 ¹⁵.

When aluminium is introduced into the system, the unit cell volume decreases considerably with increase in Al concentration, (**Figure 6.3**) which is consistent with Vegard's law¹⁶. The various Fe-O bond distances of Fe and O (**Table 6.2**) indicate significant local rearrangement probably due to strain introduced in the magnetite lattice when the markedly smaller Al^{3+} is incorporated. Such a strain

could result in the formation of smaller particles and consequent increase in surface area, which is one of the criteria to improve catalytic activity.

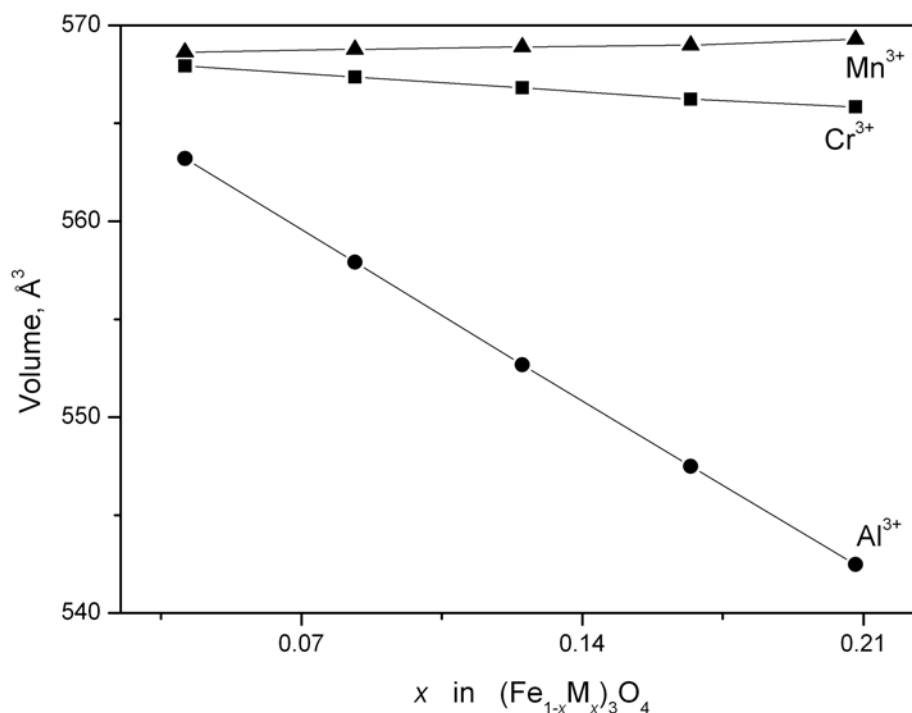


Figure 6.3: Volume versus concentration curve of different dopant systems

Mn doping

Manganese can exist in different oxidation states, and therefore both divalent and trivalent Mn ions are considered in this study. Manganese forms different types of spinel solutions with ferrites, for example, MnFe_2O_4 and FeMn_2O_4 . MnFe_2O_4 (Jacobsite) is a spinel material, where Fe is present as Fe^{3+} in the octahedral B sites with Mn^{2+} occupying tetrahedral A sites.¹⁷ In FeMn_2O_4 , Fe is present as Fe^{2+} in tetrahedral A sites and Mn^{3+} occupies the octahedral B site. In our calculations, upon incorporation of manganese into magnetite system, the unit cell volume ie, lattice parameter is almost the same when manganese is replacing Fe in the spinel system as Mn^{2+} or Mn^{3+} due to their similar ionic radii. (**Table 6.2, Figure 6.3**) In

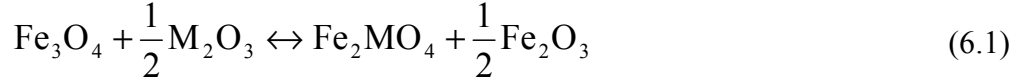
addition there is no Crystal Field Stabilization Energy for these ions, so manganese should be able to exist in either A or B sites.

Several researchers¹⁸⁻²⁰ have suggested that Mn^{3+} occupies octahedral sites at low concentrations but tetrahedral sites at high concentration. Costa *et al*²¹ reported that addition of manganese will decrease the Fe^{2+} content which implies that manganese replaces Fe^{2+} . Mossbauer studies revealed that manganese has no effect on the tetrahedral sites, ie, it replaces Fe^{2+} in the octahedral sites in magnetite. Also the authors found no phase separation in manganese ferrites, which agrees with our results that the incorporation of manganese into the lattice will form spinel solutions with magnetite.

When a tetrahedral Fe^{3+} is substituted by Mn^{2+} , the charge is balanced by converting two $2.5+$ ions in the octahedral site to $3+$. The presence of more Fe^{3+} ions in the lattice may be responsible for the decreased activity of the mixed spinel system. XRD studies revealed that the presence of manganese in the magnetite structure significantly decreases the temperature of hematite formation¹⁸, indicating that the presence of manganese may facilitate the oxidation of Fe^{2+} to Fe^{3+} and inhibit the reduction of Fe^{3+} to Fe^{2+} , which is catalytically not effective. For example, in the WGS reaction, it is important to retain the magnetite phase, where Fe^{2+} is assumed to be the active species for this reaction.

6.4.3 Solution Energies of the Mixed Spinel Oxides

The solution energies, E_s for the trivalent dopants are calculated by considering the reaction,



$$E_s = (E_{\text{Fe}_2\text{MO}_4} - E_{\text{Fe}_3\text{O}_4}) + \left(\frac{1}{2}E_{\text{Fe}_2\text{O}_3} - \frac{1}{2}E_{\text{M}_2\text{O}_3} \right) \quad (6.2)$$

where $E_{\text{Fe}_3\text{O}_4}$ and $E_{\text{Fe}_2\text{MO}_4}$ are the energies of pure and doped magnetite calculated from supercell calculations and $E_{\text{Fe}_2\text{O}_3}$ and $E_{\text{M}_2\text{O}_3}$ are the lattice energies for hematite and the dopant oxide.

For the divalent Mn^{2+} ion, the reaction becomes,



and the solution energy is given by:

$$E_s = (E_{\text{Fe}_2\text{MnO}_4} - E_{\text{Fe}_3\text{O}_4}) + (E_{\text{FeO}} - E_{\text{MnO}}) \quad (6.4)$$

where E_{FeO} and E_{MnO} are the lattice energies of the pure oxides, calculated at -39.5 eV and -38.4 eV respectively.

The solution energies for 4% doping in both octahedral and tetrahedral sites have been calculated and the results are tabulated in **Table 6. 5**. All dopant species except Mn^{2+} prefer to enter the octahedral site. The extra energy term, Octahedral Site Preferential Energy when added to the solution energy shows the preferential substitution of the octahedral sites by Cr^{3+} and Mn^{3+} even more clearly. By using Mössbauer spectroscopy, XRD and magnetisation experiments, Robbins *et al*²² proposed that Cr^{3+} ions displaced equal amounts of Fe^{2+} and Fe^{3+} from the octahedral sites in the oxygen sublattice and the displaced Fe^{2+} ions transfer to the tetrahedral sites to maintain charge balance. Here in this study, the charge balance is modelled as suggested by Robbins *et al*²². When a $\text{Fe}^{2.5+}$ ion is substituted by the trivalent ion, the charge is balanced by transferring equal amount of $\text{Fe}^{2.5+}$ to the tetrahedral site and the modelling results are consistent with the experimental data.

Dopants	Solution Energy (eV)	
	Octahedral	Tetrahedral
Cr^{3+}	-1.2	0.47 (2.1)
Al^{3+}	-1.1	0.63
Mn^{3+}	-1.02	0.33 (1.3)
Mn^{2+}	-1.06	-2.6

Table 6. 5: Solution energies for dopants (4%) in the octahedral site and the tetrahedral sites of magnetite. The figures in parentheses represent the resultant value by adding the OSPE.

The solution energy results also suggest that Al can form a solid solution. In hematite, Al is not highly soluble in the bulk material and consequently in the reduced form i.e., magnetite, low solubility or segregation of Al might be expected as well. Experimentally the solution formation is only possible at high temperature, above 900°C ¹⁵, and it has also been reported¹⁴ that at high concentration Al can enter into the tetrahedral site, which agrees with the calculated small, positive solution energy for this site (**Table 6.5**). Exsolution or formation of separate phases occurs only at high concentration and it could be suggested that the exsolution takes place when Al enters into the tetrahedral sites, where its solubility is less, resulting in the formation of different Fe-rich and Al-rich phases. The behaviour of aluminium in magnetite is discussed further below in relation to surface calculation.

For Mn^{2+} there is no octahedral stabilization energy and in principle it could enter either site. The solution energy calculations predict that divalent Mn is soluble in both sites, but preferably on the tetrahedral sites. Spinel ferrites such as FeCr_2O_3 , FeAl_2O_3 and FeMn_2O_4 are normal spinels, where the octahedral sites are occupied by the trivalent ions. However, MnFe_2O_4 is reported as both normal²³ or inverse, or random spinel²¹. Szotek *et al*²⁴ conducted a study on the electronic structure of the transition metal oxide, MnFe_2O_4 in both normal and inverse spinel structures using density functional theory. The authors reported that these systems appear to exist as a mixture of both normal and inverse spinels, which again suggest the occupation of these dopant ions in either site.

6.5 Dopants at the Surface

Surface calculations have been performed by replacing one Fe^{3+} ion in the (110) surface of magnetite with a dopant. The dopant is systematically moved from the surface towards the bulk of the material to investigate the segregational behaviour, followed by energy minimization calculations, and the total lattice energy, solution energies and segregation energy were calculated for each layer and compared. From the bulk results, preferred site occupancy for the trivalent ions has been considered as octahedral substitution and for the divalent ion, it would be tetrahedral substitution.

6.5.1 Cr^{3+}

In the fully relaxed surface structure, the outermost surface octahedral Fe^{3+} is replaced by the dopant Cr^{3+} ion. Subsequent substitution as a function of depth only involves octahedral Fe^{3+} sites. The energy profile (**Figure 6.4**) shows that Cr^{3+} prefers to stay in the bulk rather than at the surface, a similar result to that obtained in hematite. Experimental results corroborate this result as no separate phase is found in Cr-doped magnetite solutions²⁵, which might be expected if chromium segregates to the surface.

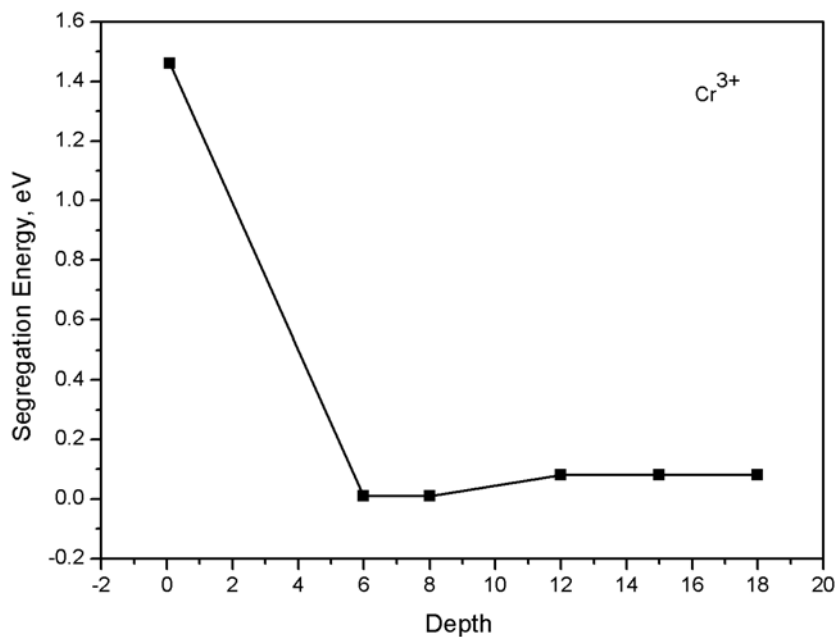


Figure 6.4: Segregation energy of Cr³⁺ at the magnetite (110) surface plotted as a function of depth (Å).

<i>Doped Magnetite</i>	<i>Solution Energy (eV)</i>	<i>Surface Energy (J/m²)</i>
Pure	-	2.1
Al ³⁺	-2.1	1.9
Cr ³⁺	0.24	2.4
Mn ³⁺	0.26	2.4
Mn ²⁺	-3.1	1.95

Table 6.6: Surface solution energies (eV) and surface energies (J/m²) of doped magnetite.

6.5.2 Al³⁺

Despite the bulk solubility of Al shown in **Table 6. 5**, the even lower surface solution energy of Al implies the segregation of the dopant to the surface, which is verified by the energy profile displayed in **Figure 6.5**. The defect surface energy is less than the pure surface energy, which indicates that the presence of aluminium gives stability to the surface. The surface Al³⁺ is five-coordinated with bond distances 1.91 Å, 1.79 Å (2) and 1.75 Å (2). The surface segregation might be the reason for the phase separation observed by Harrison et al.²⁶ The authors reported that exsolution or phase separation into Fe-rich and Fe-poor phases occurs in binary spinel solutions of Fe₃O₄ and FeAl₂O₄. This finding is in line with Turnock *et al*¹⁵, who suggested that the solution system exhibits a miscibility gap at higher temperatures from about 700°C. Exsolution or formation of separate phases occurs only at high concentration, when the Al solubility will be less, and results in the formation of different Fe-rich and Al-rich phases. The ordering or the surface segregation leads to the separation of the solution into different phases at high temperatures, which will prevent the sintering process.

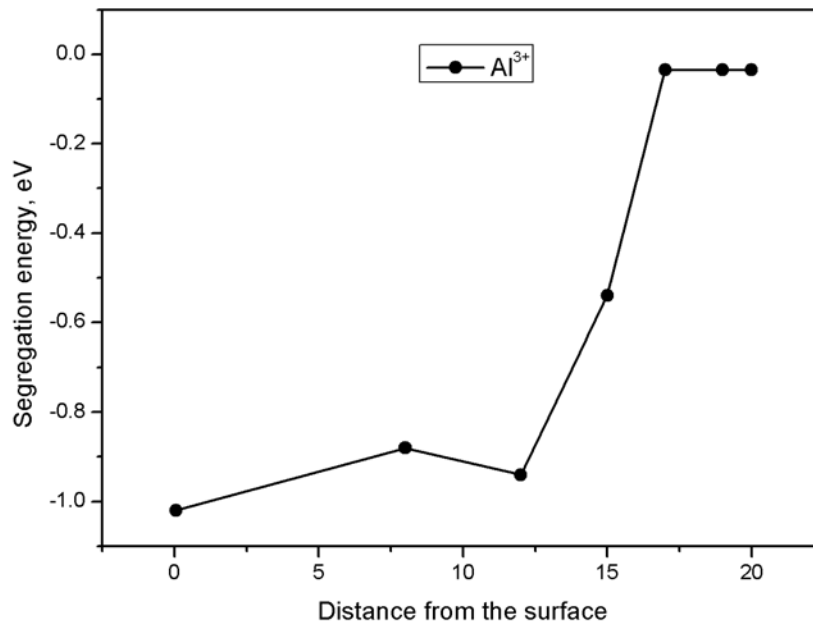


Figure 6.5: Segregation energy of the aluminium-doped magnetite (110) surface plotted as a function of dopant depth (Å).

6.5.3 Mn^{3+} and Mn^{2+}

Mn^{3+} and Cr^{3+} have similar segregation energy profiles (**Figure 6.4**, **Figure 6.7**), and Mn in its trivalent state prefers to stay in the bulk. The difference between the trivalent and divalent manganese ions is that Mn^{3+} replaces the octahedral Fe^{3+} ions while Mn^{2+} prefers to substitute tetrahedral Fe^{3+} ions, even though it can enter either site. At the surface, the tetrahedral Mn^{2+} is three-coordinated while Mn^{3+} at the surface is five-coordinated. The various Mn-O bond distances are displayed in **Figure 6.6**.

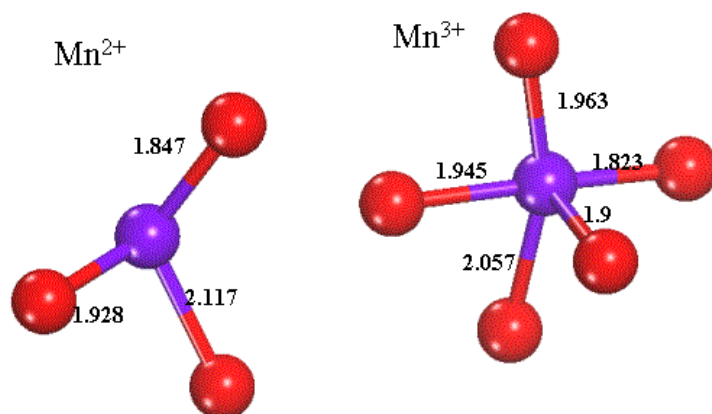


Figure 6.6: Relaxed structures of Mn^{2+} substituted at the tetrahedral sites and Mn^{3+} substituted at the octahedral sites at the surface.

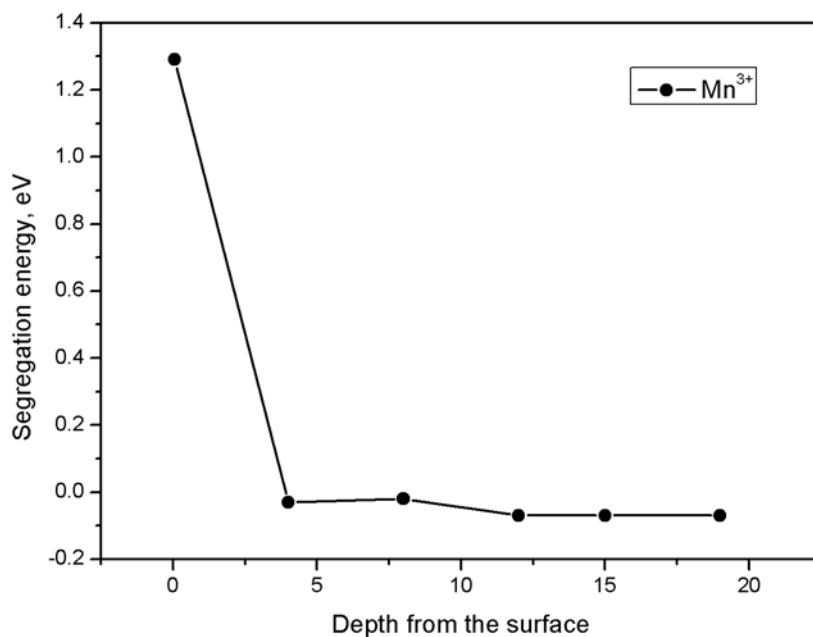


Figure 6.7: Segregation energy of Mn^{3+} is plotted against defect depth (Å).

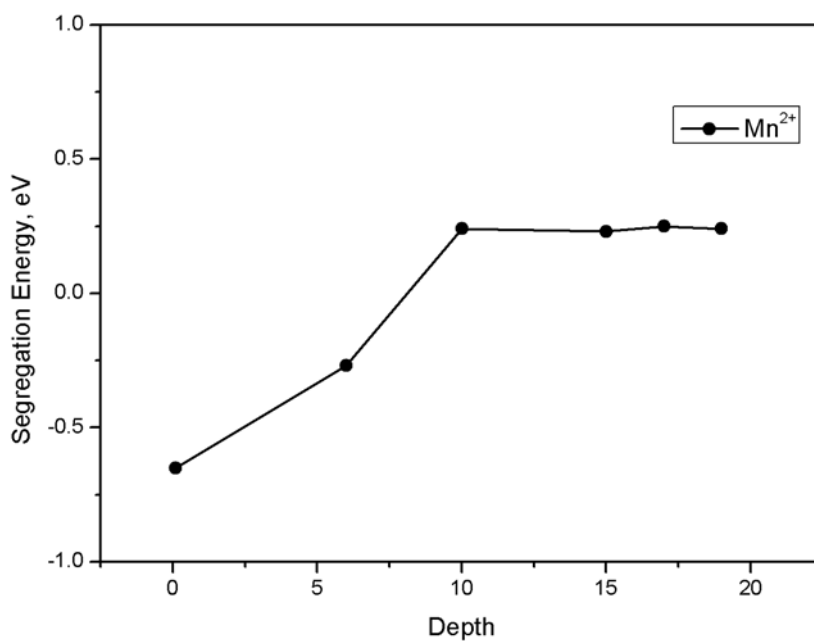


Figure 6. 8: Segregation energy of Mn^{2+} is plotted as a function of depth (Å).

The surface energies (**Table 6.6**) of the Mn^{2+} -doped surface predict that the surface is stabilized by the substitution of Mn^{2+} . This is reflected by the segregation energy profile of the dopant to the surface (**Figure 6. 8**), indicating that divalent manganese will stay in the surface layer thereby increasing the surface stability. The presence of Mn^{2+} on the surface will also result in the accumulation of Fe^{3+} ions (as a result of balancing the charge by converting two of the $\text{Fe}^{2.5+}$ ions to Fe^{3+} ions). However, thereby encouraging the formation of hematite, which will lead to a decrease in the activity of the system as, explained earlier. The segregational behaviour of Mn^{2+} is corroborated by the studies of magnetite-jacobsite (MnFe_2O_4) solutions conducted by Beard *et al*²⁷, where the authors predicted the presence of two phase regions below 600°C .

6.6 Oxygen Vacancy Formation in Magnetite

6.6.1 Oxygen Vacancies at the Bulk

Oxygen vacancies are known to play an important role in catalytic reactions. In order to study the properties of oxygen vacancies, one neutral oxygen atom from a supercell ($2 \times 2 \times 2$) of magnetite is removed before optimization of all the atom coordinates at constant pressure. The resulting energy can then be used to calculate the vacancy formation energy (*VFE*), defined as the energy required removing one single oxygen atom from the bulk material of magnetite as follows:

$$VFE = \frac{1}{2}E[\text{O}_2] + E[\text{Fe}_{3n}\text{O}_{4n-1}] - E[\text{Fe}_{3n}\text{O}_{4n}] \quad (6.5)$$

where the energies *E* are directly calculated using GULP and *n* is the number of formula units in the supercell.

Three different types of charge compensation have been considered here, representing the different oxidation states of Fe ions in the octahedral and tetrahedral sites: The oxygen vacancy is created and the charge is compensated by converting i) two tetrahedral Fe^{3+} ions to two Fe^{2+} ions, (Type 1) ii) four octahedral $\text{Fe}^{2.5+}$ ions to four Fe^{2+} ions (Type 2) and iii) converting two $\text{Fe}^{2.5+}$ to two Fe^{2+} ions and one Fe^{3+} to Fe^{2+} (Type 3). Our calculations (**Table 6.7**) showed that Type 2 is favoured over the other two schemes possibly due to the presence of more divalent cations in the lattice or the spreading of the compensating charges, which would enhance the reduction process.

Different schemes	Vacancy Formation Energy, eV	
	Bulk	Surface
Type 1	2.83	-0.1
Type 2	2.72	-0.13
Type 3	2.74	-0.03

Table 6.7: Vacancy formation energy in the bulk and at the surface.

Another possible scenario of vacancy formation, i.e. to create an oxygen vacancy as well as a divalent metal vacancy to compensate the charge, is also discussed here: i) Two octahedral $\text{Fe}^{2.5+}$ ions can be converted to one Fe^{2+} and Fe^{3+} , with the removal of the Fe^{2+} ion as well as the O^{2-} and ii) a metal vacancy is created by removing one tetrahedral Fe^{3+} and converting two $\text{Fe}^{2.5+}$ to Fe^{2+} . The latter type is energetically more favourable than the first, which again might be due to enrichment of Fe^{2+} in the lattice of the material. The supercell created is large enough (448 atoms) to exclude any effects of interaction between the vacancies.

As the concentration of oxygen vacancies increases, more divalent Fe ions will be created in the lattice with reduction continuing via the above equation.

These types of vacancy calculations could perhaps be better investigated using electronic structure calculations due to the redistribution of electronic charge. However, from the simulations obtained here, the divalent Fe species appear to play an important role in the reduction process.

We next investigated the effect of dopants on the formation of oxygen vacancies at the surface of magnetite.

6.6.2 Oxygen Vacancies on Magnetite Surface

Catalytic reactions normally take place on the surface. Studying the stability of oxygen vacancies at various distances from the surface will provide information on the presence of the oxygen vacancies at surfaces.

For these calculations, an oxygen vacancy is created on the (110) surface of magnetite and charge-compensated in the same schemes described above for the bulk material. Similar to the bulk material, the Type 2 mechanism is favoured, and the creation of one oxygen vacancy at the surface via Type 1 and Type 3 required 0.03 and 0.1 eV, respectively, more energy than Type 2 (**Table 6.7**) In order to study the distribution of the oxygen vacancies as a function of depth, the vacancy was moved from the surface to the bulk (**Figure 6. 9**) and the dependence of the oxygen vacancy formation energy on the depth from the surface of magnetite is illustrated in **Figure 6. 10**.

The energy profile shows that oxygen vacancies are more stable at the surface.

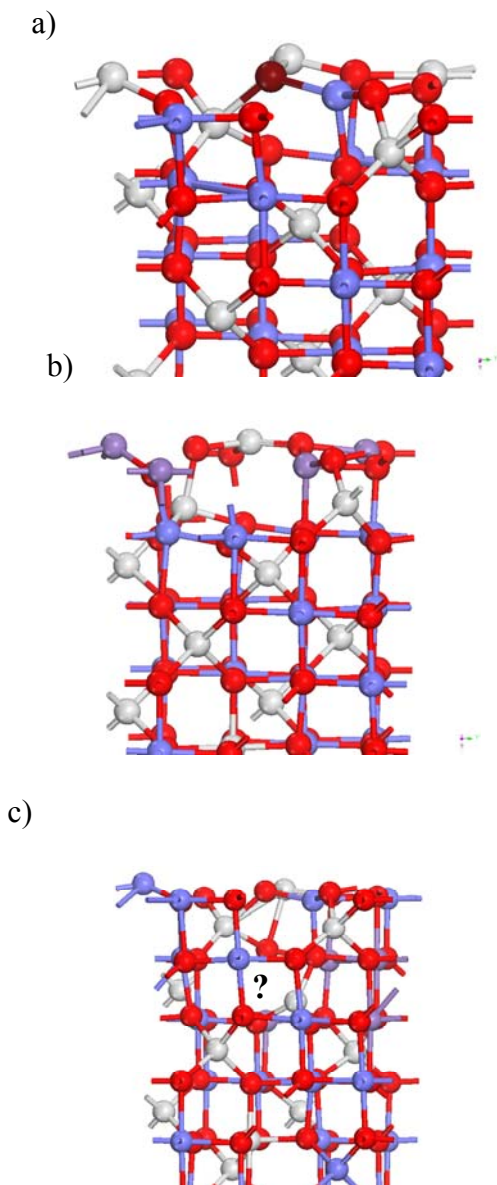


Figure 6. 9: An oxygen vacancy is created on the surface and moved gradually downwards towards the bulk. Dark red sphere represents oxygen to be removed to create a vacancy. Violet blue spheres near the oxygen vacancy represent Fe²⁺ ions, white spheres: octahedral Fe^{2.5+} ions, blue spheres: tetrahedral Fe³⁺, and red spheres represent oxygen ions. The '?' represents the oxygen vacancy moved downwards to the second layer.

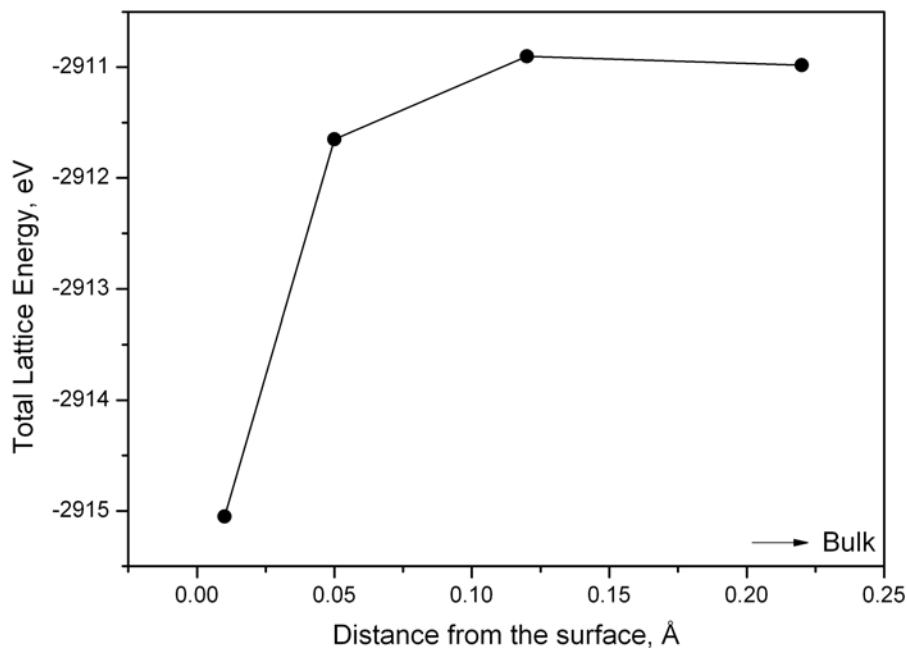


Figure 6. 10: The Total energy for oxygen vacancies as a function of depth from the surface.

6.6.3 Effect of Dopants in the Oxygen Vacancy Formation Energy

The effect of dopants on the formation of oxygen vacancies in magnetite are also considered. The dopants Cr^{3+} , Al^{3+} , Mn^{3+} and Mn^{2+} ions were substituted at the magnetite surface and the energy of formation of the oxygen vacancies were calculated as before. The data in **Table 6.8** show that for Cr^{3+} , Al^{3+} and Mn^{3+} , the oxygen vacancy formation energy is exothermic indicating the ease of creating oxygen vacancies in the presence of these dopants, when they are in the octahedral positions. If the dopants are substituted to the tetrahedral sites, the process becomes endothermic except for Al^{3+} , which still promotes oxygen vacancy formation. These results indicating that the presence of dopant promotes the formation of oxygen vacancies except manganese.

Dopants	Oxygen vacancy formation energy (eV) of the dopant at-	
	Octahedral sites	Tetrahedral sites
Cr ³⁺	-1.35	0.14
Al ³⁺	-4.91	-2.87
Mn ³⁺	-0.02	2.3
Mn ²⁺	0.52	0.54

Table 6.8: Oxygen vacancy formation energy (eV) of the doped surface of magnetite. The vacancy formation energies are calculated with dopants in octahedral and tetrahedral sites.

When chromium is substituted in the octahedral sites, which is the preferential site for Cr³⁺, the surface can sustain oxygen vacancies due to the exothermic nature of oxygen vacancy formation. However, as chromium segregates to the bulk, the surface chromium concentration will be very low.

Aluminium shows a particular tendency to promote oxygen vacancies even if they are in the tetrahedral sites, suggesting that the presence of aluminum will enhance the surface reactivity by producing oxygen vacancies more easily.

Data in **Table 6.8** indicate that oxygen vacancy formation with Mn³⁺ at the octahedral site is slightly exothermic. Vacancy formation can lead to reduction of the Mn³⁺ to Mn²⁺. The reduced Mn²⁺ can substitute both sites and in both cases the vacancy formation energy is the same and slightly endothermic, discouraging the formation of vacancies and thus the catalytic reactivity of the surface. In addition, if Mn³⁺ is reduced to Mn²⁺, the presence of Fe²⁺ at the surface is reduced.

6.7 Conclusions

The effect of dopants, Al^{3+} , Cr^{3+} , Mn^{3+} and Mn^{2+} in the cubic spinel magnetite has been investigated. The calculations reveal that Cr^{3+} and Mn^{3+} will form spinel solutions with magnetite with a preference for octahedral site occupancy, while aluminium prefers to be segregated to different phases at higher concentrations. Addition of impurities affects the stability of the surface; for example, the presence of aluminium and divalent manganese increases the surface stability, whereas, chromium, aluminium and manganese in their trivalent oxidation state should make the surface more active by promoting oxygen vacancy formation. Aluminium-doped magnetite leads to highly stable surface encouraging large surface area. The loss of catalytic activity in Mn doped magnetite can be explained on the basis of the accumulation of Mn^{2+} and Fe^{3+} at the surface.

The mean field approach has been used to obtain general trends, which will help to predict the mixing behaviour and surface structures of the system. However this method is not suitable to investigate electronic or magnetic effects in a spin model like magnetite. Electronic structure calculations would be needed to explore the reactivity or electron-dependent properties in detail.

In the next chapter, the theoretical results obtained from this study are interpreted in the context of experimental results.

6.8 References

- 1 G.V.Lewis and C. R. A. Catlow, *Journal of Physics C: Solid State Physics*, 1985, **18**, 1149-1161.
- 2 L. R. Lloyd, D. E.; Twigg, M. V. E., *Catalyst Handbook*, Wolfe Publications, London, 1989.
- 3 J. P. Wright, J. P. Attfield and P. G. Radaelli, *Physical Review B*, 2002, **66**, 214422.
- 4 A. Schlegel, S. F. Alvarado and P. Wachter, *Journal of Physics C: Solid State Physics*, 1979, **12**, 1157-1164.
- 5 Hiroshi Yasuoka, Akira Hirai, Teruya Shinjo, Masao Kiyama, Y. Bando and T. Takada, *Journal of the Physical Society of Japan*, 1967, **22**, 174-180.
- 6 P. Piekarczyk, K. Parlinski and A. M. Oles, *Physical Review B*, 2007, **76**, 165124.
- 7 J. D. Gale, *Journal of the Chemical Society-Faraday Transactions*, 1997, **93**, 629-637.
- 8 A. Szytu, Lstrok, A. Burewicz, Zcaron, Dimitrijevi, Cacute, S. Kra, Sacute, nicki, H. R, Zdot, J. Todorovi, A. Wanic and W. Wolski, *Physica Status Solidi (b)*, 1968, **26**, 429-434.
- 9 T. K. Kundu, K. H. Rao and S. C. Parker, *Journal of Colloid and Interface Science*, 2006, **295**, 364-373.
- 10 G. Maris, O. Shklyarevskii, L. Jdira, J. G. H. Hermsen and S. Speller, *Surface Science*, 2006, **600**, 5084-5091.
- 11 F. Magalhães, M. C. Pereira, S. E. C. Botrel, J. D. Fabris, W. A. Macedo, R. Mendonça, R. M. Lago and L. C. A. Oliveira, *Applied Catalysis A: General*, 2007, **332**, 115-123.
- 12 M.Rosenberg, P.Deppe, H.U.Janssen, V. A. M. Brabers, F.S.Li and S.Dey, *Journal of Applied Physics*, 1985, **57**, 3740.
- 13 V. N. Antonov, B. N. Harmon, V. P. Antropov, A. Y. Perlov and A. N. aresko, *Physical Review B*, 2001, **64**, 134410.
- 14 Ute Golla-Schindler, Hugh St.C. O'Neill and A. Putnis, *American mineralogist*, 2005, **90**, 1278-1283.
- 15 A. C. Turnock and H. P. Eugster, *Journal of Petrology*, 1962, **3**, 533-565.

- 16 W. F. J. Fontijn, P. J. van der Zaag, M. A. C. Devillers, V. A. M. Brabers and R. Metselaar, *Physical Review B*, 1997, **56**, 5432.
- 17 Gabriela Marinescu, Luminita Patron, Oana Carp, Lucian Diamandescu, Nicolae Stanica, Aurelia Meghea, Maria Brezeanu, J. C. Grenier and J. Etourneau, *Journal of Materials Chemistry*, 2002, **12**, 3458-3462.
- 18 L. C. A. Oliveira, J. D. Fabris, R. R. V. A. Rios, W. N. Mussel and R. M. Lago, *Applied Catalysis A: General*, 2004, **259**, 253-259.
- 19 G. Marinescu, L. Patron, O. Carp, L. Diamandescu, N. Stanica, A. Meghea, M. Brezeanu, J.C. Grenier and L. Etourneau, *Journal of Materials Chemistry*, 2002, **12**, 3458.
- 20 C. Wende, K. Olimov, H. Modrow, F. E. Wagner and H. Langbein, *Materials Research Bulletin*, 2006, **41**, 1530-1542.
- 21 R. C. C. Costa, M. F. F. Lelis, L. C. A. Oliveira, J. D. Fabris, J. D. Ardisson, R. R. V. A. Rios, C. N. Silva and R. M. Lago, *Journal of Hazardous Materials*, 2006, **129**, 171-178.
- 22 M. Robbins, G. K. Wertheim, R. C. Sherwood and D. N. E. Buchanan, *Journal of Physics and Chemistry of Solids*, 1971, **32**, 717-729.
- 23 R. J. Hill, J. R. Craig and G. V. Gibbs, *Physics and Chemistry of Minerals*, 1979, **4**, 317-339.
- 24 Z. Szotek, W. M. Temmerman, D. Ködderitzsch, A. Svane, L. Petit and H. Winter, *Physical Review B*, 2006, **74**, 174431.
- 25 M.C.Rangel, R.M.Sasaki and F.Galembeck, *Catalysis Letters*, 1995, **33**, 237-254.
- 26 R. J. Harrison and A. Putnis, *American Mineralogist*, 1996, **81**, 375-384.
- 27 J. S. Beard and R. J. Tracy, *American Mineralogist*, 2002, **87**, 690-698.
- 28 J. D. Dunitz and L. E. Orgel, *Journal of Physics and Chemistry of Solids*, 1957, **3**, 318-323.
- 29 D. S. McClure, *Journal of Physics and Chemistry of Solids*, 1957, **3**, 311-317.

Chapter 7

Implications for Catalysis and Conclusions

This section concludes and discusses the catalytic implications of the results obtained from the theoretical calculations presented within this thesis. The Fe-Cr mixed oxide system is currently the most effective industrial catalyst used for HT-WGS reaction. A comprehensive knowledge of the effect of defects on the behaviour and properties of the iron oxide materials is of critical importance in the design and development of improved catalyst materials. The investigation of the pure and defect properties for both bulk and surface of hematite provides information about promising dopants, which could be used to replace chromium. From the calculations, it is evident that aluminium and chromium have similar effects on the catalysts despite exhibiting different behavioural patterns. Preliminary calculations have speculated that manganese might be a good substitute for chromium, however further detailed studies revealed that manganese affects the catalyst in a different manner to chromium. Even though the reduction conditions favour the presence of manganese, other criteria, for example its activity, have to be analysed in order to propose it as a suitable alternative catalyst.

It is generally accepted that the role of chromium in the WGS reaction is to prevent sintering, increase the surface area of the catalyst and suppress the over-reduction of the active catalyst^{1, 2}. However to date there has been no detailed theoretical study on the structural and geometrical origins of this fact. To shed light onto this area, we investigated how chromium incorporates into the iron oxide (Fe_xO_y) lattice and discussed in detail in Chapters 3, 4 (hematite), 5 (maghemite) and 6 (magnetite). In Chapters 3 and 4, chromium and aluminium incorporation into hematite were studied. It was found that the prevention of sintering occurs due to a different mechanism between aluminium and chromium, which as its origins in the different structural properties. Cr^{3+} is found to be distributed randomly whereas Al^{3+} segregates to the surface. In Chapter 4 we also investigated the role of magnetism and the stability. This was achieved by including only the Fe-Fe interactions assuming that these interactions are stronger than Cr-Cr interactions at the temperatures of interest here. The general conclusions regarding segregation and stability of Fe-Al and Fe-Cr were unchanged for $T > 300\text{K}$, however, at $< 300\text{K}$, solution formation were no longer thermodynamically stable.

The effect of dopants on the thermal stability of different iron oxide phases, hematite and the meta-stable phase, maghemite were discussed in Chapter 5, where the addition of dopants, especially aluminium, was found to improve the thermal stability of maghemite and increases the γ - to α - transition temperature.

In Chapter 6, we discussed the activation of the catalyst by the reduction of hematite to magnetite. During the reduction process, some Fe^{3+} is reduced to Fe^{2+} , because reduction of Cr^{3+} to Cr^{2+} is quite unlikely due to the significant higher reduction enthalpy of Cr^{3+} . Therefore the end result will be unreduced Cr^{3+} occupying B sites, which will inhibit the crystal growth of the active catalyst, magnetite. Although, from the calculations presented here, there is an indication that some segregation occurs for reduced magnetite. Certain controversies still remain in the literature concerning the surface enrichment of chromium ions, which appears to be highly dependent on the method of preparation³. However, some researchers^{4, 5} have suggested that the

surface enrichment of chromium ions could be due to the hexavalent chromium,⁶ which prefers to segregate to the surface.

Fe-Al catalysts were modelled to allow comparison with the Fe-Cr system in Chapters 3, 4 and 6. The surface energy calculations presented in Chapter 3 and 6 show that the addition of aluminium produces smaller crystallites and hence larger surface areas, which is attributed to the segregational / phase separation nature of aluminium. The results also show that in contrast to chromium, which reduces the crystallite size via lattice dissolution, aluminium segregates to the surface, i.e. crystal growth is inhibited due to the blocking of surface cation sites. In hematite, Al^{3+} is less soluble than Cr^{3+} in the bulk primarily due to the difference in ionic size. The segregation of aluminium in hematite leads to a separation of Al-rich and Fe-rich phases rather than the formation of homogenous solutions. Similarly in magnetite, the negative segregation energy for aluminium indicates that a marked surface enrichment would be expected, and this surface enrichment has the potential to block the active surface sites, which could lead to decrease in catalytic activity.

The predicted solubility of Mn^{3+} in hematite is similar to Cr^{3+} (Chapter 3). From a catalytic perspective it is important to distinguish between the presence of Mn^{3+} and Mn^{2+} . However, this is difficult to achieve experimentally but possible to tackle theoretically. The reduction of Mn^{3+} to Mn^{2+} is easily accessible and it is found that when manganese is in its divalent form, it preferably occupies the tetrahedral sites, while Mn^{3+} occupies the octahedral sites. This structural difference indicates that different catalytic behaviour would be expected for Mn^{2+} compared to Cr^{3+} due to the influence of electronic structure upon geometrical properties. The calculations show that an increase in concentration of Mn^{2+} at the surface leads to the easy formation of hematite by decreasing the formation temperature, which results in a decrease in catalytic activity due to the formation of a hematite layer on the surface.

Overall this project has provided valuable information on the structural influences of the Fe_xO_y WGS catalyst particularly the relative stability of chromium, aluminium and manganese ions and their likely geometrical structure. The segregation properties and the preferential positioning of ions in the lattice can be used to understand the influence of dopants and sintering process. This work is currently undergoing experimental validation and directing the development of new chromium - free industrial catalysts.

For future work, a useful extension of the present investigation would be to apply electronic-structure modelling techniques, such as density functional theory (DFT), which can incorporate electronic and magnetic effects which is especially important for complex oxide systems like magnetite.

7.1 References

- 1 D. S. Newsome, *Catalysis Reviews : Science and Engineering*, 1980, **21**, 275.
- 2 M. V. Twigg, *Catalyst Handbook* Wolfe Publishing, London, 1989.
- 3 G. Doppler, A. X. Trautwein, H. M. Ziethen, E. Ambach, R. Lehnert, M. J. Sprague and U. Gonser, *Applied Catalysis*, 1988, **40**, 119-130.
- 4 M. A. Edwards, D. M. Whittle, C. Rhodes, A. M. Ward, D. Rohan, M. D. Shannon, G. J. Hutchings and C. J. Kiely, *Physical Chemistry Chemical Physics*, 2002, **4**, 3902-3908.
- 5 C. Rhodes and G. J. Hutchings, *Physical Chemistry Chemical Physics*, 2003, **5**, 2719-2723.
- 6 C. Martos, J. Dufour and A. Ruiz, *International Journal of Hydrogen Energy*, 2009, **34**, 4475-4481.

Appendix I

The lattice energies of pure oxides calculated from simulations.

Pure Oxides	Lattice Energy, eV / M ₂ O ₃
Fe ₂ O ₃	-150.37
Cr ₂ O ₃	-154.29
Al ₂ O ₃	-160.99
Mn ₂ O ₃	-151.28
Ti ₂ O ₃	-150.96
V ₂ O ₃	-150.27
Sc ₂ O ₃	-144.89
Y ₂ O ₃	135.04
La ₂ O ₃	-126.41